MMIC and RFIC Solutions for Modern Radio Astronomy

by

Alireza Seyfollahi

B.Sc., Isfahan University of Technology, 2015

M.Sc. University of Victoria, 2018

A Dissertation Submitted in Partial Fulfillment of the

Requirements for the Degree of

DOCTOR OF PHILOSOPHY

in the Department of Electrical and Computer Engineering

We acknowledge and respect the lək̓ʷəŋən peoples on whose traditional territory the university stands and the Songhees, Esquimalt and W̱SÁNEĆ peoples whose historical relationships with the land continue to this day.

MMIC and RFIC Solutions for Modern Radio Astronomy

by

Alireza Seyfollahi

B.Sc., Isfahan University of Technology, 2015

M.Sc. University of Victoria, 2018

Supervisory Committee

Dr. Jens Bornemann, Supervisor

(Department of Electrical and Computer Engineering)

Dr. Frank Jiang, Co-supervisor

(Department of Electrical and Computer Engineering and National Research Council, Herzberg Astronomy and Astrophysics Research Centre, Victoria)

Dr. Colin Bradley, Outside Member

(Department of Mechanical Engineering)

Abstract

This dissertation presents research on theory, design, EM modeling, fabrication, packaging and measurement of Monolithic Microwave Integrated Circuits (MMICs) and Radio Frequency Integrated Circuits (RFICs) for modern radio receivers. The purpose of the thesis is to demonstrate technology development for the future state of the art radio telescopes such as the Dish Verification Array (DVA-2), next generation Very Large Array (ngVLA) and Canadian Hydrogen Observatory and Radio-transient Detector (CHORD). The goal is to design integrated circuits that address the unique challenges of each radio telescope frontend in the microwave and millimeter wave regime ranging 1-120 GHz. Low noise figure, high gain and wide bandwidth cryogenic and room temperature Low Noise Amplifiers (LNA) and wideband high conversion gain mm-wave mixers are the critical components of a radio receiver. This work aims to research and develop integrated circuits based on four semiconductor technologies: GaAs pHEMT, GaAs mHEMT, InP HEMT and SiGe BiCMOS. Each technology has its unique advantages that make it the optimum choice for each specific block in the radio receiver chain. GaAs mHEMT and InP HEMT offer the ultimate low noise and high operational frequency that is suitable for cryogenic LNAs. GaAs pHEMT features low noise, excellent repeatability and medium power capacity that is advantageous in post amplifier (warm amplifier) and mixer design. SiGe BiCMOS with very high cut-off frequency HBTs and standard CMOS and multi-metal back end of line (BEOL) is the best option for millimeter-wave down-converter and post amplifier with high degree of integration. The fundamentals of each semiconductor technology are reviewed and the design methodology of four LNAs at, UHF (0.3-1.5 GHz), Ku (12-24 GHz), Ka (18-36 GHz) and Q (30-52 GHz) bands and three mm-wave mixers at Q (35-50 GHz and 33-55 GHz) and W (70-120 GHz) bands are presented with the focus on low noise, high gain, wide bandwidth and low input/output return loss. A co-design method is employed to account for packaging and wire bond effect.

The designed MMICs and RFICs are validated by measurements of several prototypes, and compared to similar published works and commercially available chips that demonstrates their capability required by the next generation of radio telescopes.

Table of Contents

List of Tables

List of Figures

List of Symbols

v	velocity
v_{eff}	effective channel velocity
τ_c	mean free time between collisions
Γ	reflection coefficient
dB	decibel
dBm	decibel milliwatt
$\vec{E}$	electric field
$\vec{F}$	force
f	frequency
f_T	cut-off frequency
G	gain
g_m	transconductance
I_{DSS}	drain current at gate-source voltage equal to zero
k	Stern stability factor
m^*	electron effective mass
NF	noise figure
P	power
Q	electron charge
T	temperature

Acronyms

2DEG	two-dimensional electron gas
AC	alternating current
ADC	analog to digital converter
ALMA	Atacama Large Millimeter Array
BEOL	back end of line
CAD	computer-aided design
CHIME	Canadian Hydrogen Intensity Mapping Experiment
CHORD	Canadian Hydrogen Observatory and Radio-transient Detector
CMBR	cosmic microwave background radiation
CMOS	complementary metal-oxide-semiconductor
DC	direct current
DRC	design rule check
EM	electromagnetic
FET	field effect transistor
HAA	Herzberg Astronomy and Astrophysics
HBT	heterojunction bipolar transistor
HEMT	high electron mobility transistor
IC	integrated circuit
IF	intermediate frequency
LNA	low noise amplifier
LO	local oscillator

MESFET	metal-semiconductor field effect transistor
MIM	metal-insulator-metal
MMIC	monolithic microwave integrated circuit
MOS	metal-oxide-semiconductor
MSG	maximum stable gain
ngVLA	next generation Very Large Array
NRAO	National Radio Astronomy Observatory
NRC	National Research Council (Canada)
OMT	orthomode transducer
PNA	power network analyzer
RF	radio frequency
RFIC	radio frequency integrated circuit
SEM	scanning electron microscope
SIS	superconductor-insulator-superconductor
TFR	thin film resistor
VLA	Very Large Array
VNA	vector network analyzer

Acknowledgment

I would like to express my sincere gratitude to my supervisors Dr. Jens Bornemann and Dr. Frank Jiang for their inspiration, patience, and continuing support.

I would like to devote this work to the love of my life, Avi, who accompanied me in the path that I traveled and to whom I owe my success. Also, to my parents, Sousan, Abdoreza, Faranak and Mohammadreaza, and my sister, Maryam, for all the support throughout the past years.

My greatest gratitude goes to Dr. Julia Penfield who has been a mentor in my professional carrier and a true friend in my personal life.

Last but not least, I would like to thank my colleagues, Dr. Lewis Knee, Mr. Dominic Garcia, Mr. Pat Niranjanan, Mr. Doug Henke and Mr. Adam Densmore in the Radio Instrumentation Team at the National Research Council Herzberg Astronomy and Astrophysics Research Centre.

Radio Astronomy embraces a wide range of topics from physical phenomena to receiver and antenna design, and radio telescopes bring together the state of the art in several areas of electrical and mechanical engineering.

Radio Astronomy, J. D. Kraus

Chapter 1

Introduction

1.1 A Brief History of Radio Astronomy

Radio astronomy is a relatively young branch of science that was born in 1932 when a discovery was made by Karl Jansky at Bell Telephone Laboratories. In the study of radio interference at a frequency of 20.5 MHz, Jansky recorded an unknown signal for several months from all directions [1]. When he published his results in "Proceedings of the IRE" [2], he called the received signal "electrical disturbances apparently of extra-terrestrial origin" [3] [4].

Jansky's discovery of extraterrestrial radio noise was totally unexpected to him and did not elicit much if any interest from the astronomers of the time. There was only optical astronomy back then and little understanding of much more than traditional optical solar, planetary, and stellar astronomy.

However, he also noticed a steady weaker background noise that seemed always to be present, and after studying it for some time realized that the strength of this background noise seemed to rise and fall daily, with the position in the sky of peak intensity tracking across the sky in a roughly 24-hour cycle. This was the first hint that the noise came from beyond the Earth. The Sun's motion around the Earth takes 24 hours, but the position of peak intensity was not in the direction of the Sun, so it could not be the Sun. Jansky eventually realized that the periodicity of the signal was not quite 24 hours – it was closer to 23 hours 56 minutes. This was the key, because 23 hours 56 minutes is the rotation period of the Earth relative to the stars (since the Earth orbits the Sun while rotates, the "solar day" of 24 hours is slightly longer than the "sidereal day"). This meant the noise was coming from outside the solar system!

What Jansky had discovered was the low-frequency emission of free electrons spiraling along field lines in the interstellar magnetic field of the Galaxy ("synchrotron emission"). This emission varied in intensity throughout the Galaxy, being stronger in the Galactic plane and towards the center of the Galaxy, and Jansky's telescope had just enough angular resolution to pick out one of the emission peaks and follow it across the sky. But astronomers did not know what it was, it did not correspond with anything they knew or cared about. So, it was not followed up until Reber.

In 1940, Grote Reber performed a survey of the sky at various frequencies between 160 MHz and 480 MHz using a parabolic reflector in his backyard that attracted the astronomers' attention to radio astronomy [4] [5].

Radio transmitter, receiver, and antenna technology grew enormously during the Second World War with the development of radar for military purposes. During the war, some engineers noted that sometimes radar antennas pointed near the Sun would pick up excess noise (Jansky's equipment could not pick up these solar radio emissions). By the time some of those engineers began to follow up on that after the war, Reber had already single-handedly established radio astronomy by following up on Jansky's discovery.

Reber's first attempts to detect Jansky's extraterrestrial radio noise were at frequencies much higher than Jansky's ~ 20 MHz. Reber tried 3300 MHz and 900 MHz but did not detect anything. Then he tried the lower frequency of 160 MHz and was successful in 1938.

He assumed that the noise was probably just the low-frequency tail of the aggregated black-body spectrum of stars in the Galaxy. The spectral index of hot objects like stars (thousands of degrees) is positive at radio frequencies, so the emission should be stronger at higher frequencies. But unexpectedly, he discovered the emission was weaker at higher frequencies.

Radio astronomy became an important part of astronomy with the technical improvements in microwave engineering in the 1950s when radio telescopes were built in several countries

The discovery of the 21 cm (1420 MHz) emission from Galactic neutral hydrogen atoms in 1951 was the first detection of spectral line radiation from the Galactic interstellar medium (ISM) and was important because the study of the Doppler shift of the line in various directions provided the first potential way to map the kinematics and structure of the ISM. It was also important as it suggested that perhaps molecules might exist in the ISM which could also be detected and studied at radio wavelengths. Radio observations in the 1960s and 1970s confirmed that there were a wide variety of molecules in the Galactic ISM, and thus began the discipline of astrochemistry and a major advance in the understanding of the theory of star formation (stars only form in regions of the ISM where densities are high enough that their composition is dominated by molecules – stars cannot form in atomic hydrogen regions).

Interestingly, the detection of the cosmic microwave background was, like Jansky's discovery, an accident while diligent radio astronomers were trying to understand the origin of a weak, constant, and uniform noise source in their antennas. Very careful work to characterize and account for all sources of noise in their system left this weird 3 K residual noise, which they soon realized might be the predicted remnant emission from the Big Bang.

By the 1970s many large radio telescopes were operating. To collect more signals and increase the resolution, telescopes grew larger in size up to 45 m by the end of the1980s. And radio astronomers were able to extend the frequency range into millimeter and sub-millimeter wavelengths [4].

Important astronomical discoveries were the direct result of advancement in radio telescopes such as:

- discovery of radiation from Galactic neutral atomic hydrogen in 1951
- identification of quasars in 1962
- radio observations of the OH lines in the interstellar medium in 1963
- discovery of the cosmic microwave background radiation (CMBR) in 1965
- discovery of pulsars in 1967
- the discovery of many other lines of interstellar molecules such as CO in 1970
- discovery of first binary pulsars in 1974
- imaging of 4769 Castali Asteroid by Arecibo in 1989

and recent discoveries of

- radio evidence for the existence of black holes, gravitational wave radiation,
- details of the birth of stars and other solar systems,
- discovery of the anisotropy of the CMBR, which directly measures the structure of the early Universe [3]

Studying the electromagnetic spectrum of the received signal from space in all directions shows two major peaks at millimeter and sub-millimeter ranges that contain the preponderance of the radiated electromagnetic energy in the Universe. The largest is the radiation of a 3-K blackbody, a result of the Big Bang that occurs at around 160 GHz (wavelength of about 2 mm). The other peak is located at 2 THz (wavelength of 150 μm) which is produced by stellar radiation absorbed and re-radiated by dust which is only detectable using space telescopes due the strong absorption by oxygen, water and other molecules in the Earth's atmosphere. However, the space telescopes are limited in sensitivity and angular resolution of the instrument that can be launched into space.

Radio telescopes are used to study the continuum and line emission of atomic and molecular clouds that form galaxies, stars and planets in the Universe. For instance, the majority of the non-CMBR sub-millimeter emission comes from the tremendous episodes of star formation in very distant galaxies at the earliest stage of the creation. These radiations are not visible in the optical spectrum as they have redshifted to sub-millimeter

wavelengths and are blocked by the atmosphere. Moreover, the optical light is absorbed by the great amount of dust in the galaxies and re-emitted at longer wavelengths. Therefore, identifying and studying these star-forming young galaxies requires instruments that provide high sensitivity, dynamic range and angular resolution comparable to or better than those available at other wavelengths; resolutions as high as 0.01" to 0.1".

The angular resolution, θ, of a telescope is given by wavelength, λ, divided by the aperture diameter D:

$$\theta = \frac{\lambda}{D} \tag{1.1}$$

For example, for a radio telescope receiving radio waves at 300 MHz, an aperture of 200 km is required to get one arcsec resolution while the same resolution can be achieved by a 10-cm aperture for a telescope in visible light. Therefore, to achieve the resolutions required for studying the star-forming galaxies, large telescopes are necessary.

Radio telescopes operate either as individual single-dish antennas or as interferometric arrays of multiple antennas. The sensitivity of a radio telescope or array is defined by the radiometer equation [6]:

$$\Delta T = T_{sys}\sqrt{\frac{1}{N f_{BW}\tau} + \left(\frac{\Delta G}{G}\right)^2} \tag{1.2}$$

where N is the number of receivers (for a single-dish system $N = 1$), f_{BW} is the observation bandwidth and τ is the integration time. G is the receiver gain, and ΔG is the gain stability. T_{sys} is the system noise temperature given as

$$T_{sys} = T_{ant} + T_{LNA} + \frac{T_{backend}}{G_{LNA}} \tag{1.3}$$

T_{ant} is the noise temperature of the antenna including the background noise temperature, ohmic losses and spillover; T_{LNA} and G_{LNA} are the noise temperature and gain of the LNA. $T_{backend}$ is the effective noise temperature of the rest of the electronic circuitry following the LNA. This shows the importance of having a very low noise, very high gain LNA. It directly affects the system noise temperature and the radio telescope's sensitivity.

Based on Equation (1.2), increasing the bandwidth of operation will reduce the observation time required for a given sensitivity. Increasing the effective collecting area of the dish will also increase sensitivity by allowing more power to be collected in a given integration time. Arrays also have other advantages, such as the ability to form independently operating sub-arrays and electronic beam-steering.

The cost of building a large paraboloid reflector with a surface accuracy sufficient for millimeter-wave operation (much smaller than a small fraction of a wavelength) increases roughly as the cube of the dish diameter due to the challenges in maintaining the precision while operating in the presence of wind, uneven solar heating, and shifting gravitational stresses. This makes the construction of very large single-dish telescopes impractical. Interferometric arrays consisting of large numbers of smaller antennas such as the Very Large Array (VLA), Figure 1.1, and the Atacama Large Millimeter Array (ALMA), Figure 1.2, offer high sensitivity and angular resolution at the expense of a more complex signal processing system and a requirement for a large number of receivers to be provided.

Figure 1.1. The Very Large Array in New Mexico, which operates mostly at cm-wave frequencies. The 28 antennas are of 25 meter diameters. Credit: NRAO.

For future arrays such as the Square Kilometer Array (SKA) and the next generation Very Large Array (ngVLA), providing a cost effective receiver with a desired sensitivity is an engineering challenge.

Figure 1.3 shows the sensitivity of the next generation of radio telescopes in comparison with the current state-of-the-art telescopes. Achieving higher sensitivity in a cost effective manner requires receivers with lower noise, wider bandwidth, lower power consumption, and simpler architecture. These define guidelines at component level development for receiver front ends such as the cryogenic low noise amplifier, warm low noise amplifier and mm-wave down-converters. The relatively high absorption region at above 50 GHz to about 70 GHz is not of great interest in radio astronomy due to the high attenuation peak of oxygen at 60 GHz.

1.2 Overview of a Radio Telescope Receiver

A radio telescope is in many ways similar to other microwave or millimeter-wave wireless communication receivers. A noisy electromagnetic signal is captured by a suitable antenna,

Figure 1.2. The Atacama Large Millimeter Array in northern Chile. In the center is one of the twelve 7-meter antennas and in the background a few of the 54 12-meter antennas. Credit: Joint ALMA Observatory.

amplified, down-converted, digitized, and processed in hardware and software to extract the desired information [7]. What makes an astronomical receiver unique are not the fundamental principles of its operation, but rather the unusual and often very extreme specifications that govern its design [3]. The most important factor in all radio telescopes is the noise temperature (noise figure) as discussed above in the radiometer equation.

Up until the previous generation of radio telescopes, the available technology allowed direct amplification for frequencies up to about 50 GHz where gallium arsenide (GaAs) and indium phosphide (InP) high electron mobility transistor (HEMT) microwave monolithic integrated circuit (MMIC) amplifiers were used before the frequency down-conversion stage.

MMIC LNAs showed the best performance in mid-range frequencies of 20 to 50 GHz. Below 20 GHz, hybrid LNAs had better performance by utilizing high Q passive discrete components. On the other hand, the performance of the MMIC LNAs would degrade at frequencies above 50 GHz due to low gain, high noise transistors, resistive loss and low Q

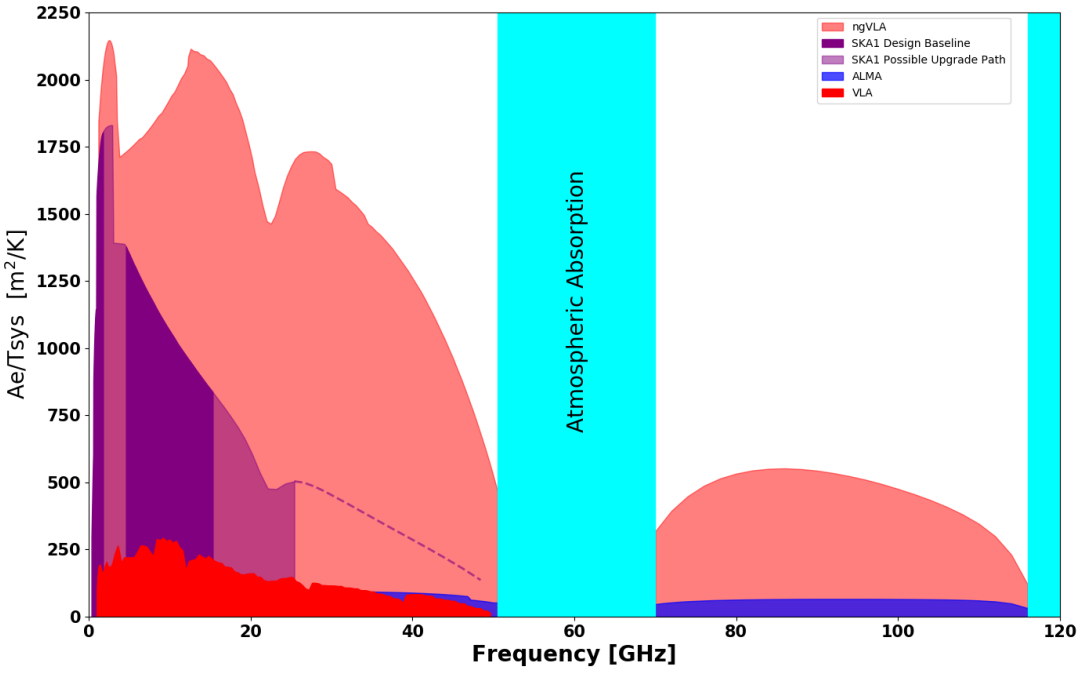

Figure 1.3. A comparison of sensitivity for a number of radio, mm, and sub-mm dish arrays expected to be operational in the 2030s. The y-axis shows the ratio of effective collecting area to system temperature, a figure of merit that accounts for the efficiency of the antennas as a function of frequency as well as the performance of the receivers and the atmospheric transparency. Credit: NRAO.

passives. However, with advances in semiconductor processing and photolithography methods in the past two decades, current MMICs utilize devices with smaller features (higher transconductance and lower noise), thicker metal layers and thinner substrates that allow frequencies of operation well above 100 GHz [8] [9] [10] [11] as well as MMIC LNAs with very good performance below 10 GHz [12] [13] [14] [15].

Deep in the sub-millimeter frequencies, low-noise superconductor-insulator-superconductor (SIS) tunnel junction mixers are used for the initial down-conversion. The price paid is that SIS mixers are expensive, costly to produce, and need to be cooled down to around liquid helium temperatures (4.2 K) to function (hence complex and expensive), whereas HEMT low noise amplifiers have acceptable performance at a much more easily achievable physical temperature of ~ 15 K. SIS mixers also need complicated quasi-optical or waveguide local oscillator (LO) distribution; and providing IF bandwidths greater than about a few GHz is difficult. Therefore, as long as the system requirements are met, LNAs hold an advantage over SISs due to simpler and less expensive receiver architecture.

Modern radio receivers necessitate the use of wider band definitions to minimize the number of receivers to cover the spectrum of interest as well as wider tuning range across the available atmospheric radio bands. The wider band definition requires low noise amplifiers that provide high gain and low noise over a wider frequency range. This is a challenge considering the trade-offs between noise, input matching and gain in LNA design methodology. Regardless of being a hybrid or a monolithic design, the LNA must be reproduced in high numbers with great reliability to build hundreds of identical receivers for a radio telescope array. Therefore, as long as a monolithic integrated LNA meets the design constrains, it has advantage over a hybrid solution since it can be reproduced in large volumes with great consistency.

Wider intermediate frequency (IF) bandwidths help to enhance the sensitivity in total power measurements and speed up wide-band spectral line surveys. Some of the newer telescope facilities on the horizon call for a continuous operational frequency spectrum of several decades, and instantaneous IF bandwidths of up to 8 GHz are already common [7]. The wider RF and IF bandwidths require a down-converter mixer above 10 GHz, where direct sampling is not possible, that has wideband performance. The commercially

available downconverters usually have narrow IF bandwidth, and those with wide RF and IF bands have high conversion loss, especially at mm-waves [16] [17] [18].

The mixer should be able to cover the entire RF band with acceptable input return loss, a consistent conversion gain and high isolation. The high conversion gain can relax the cryogenic LNA/warm RF amplifier gain requirement. Mixers presented in [19] [20] [21] [22] introduce conversion loss and poor input match at the RF port.

Figure 1.4 (a) shows a simplified block diagram of a conventional radio receiver chain. The first component is a high density polyethylene (HDPE) located in front of the cold cartridge. The 15 K cold cartridge includes the corrugated horn antenna, orthomode transducer (OMT) and RF LNAs. The OMT separates the two orthogonal linear polarizations. The OMT's broadband response is designed to suppress higher order modes to provide flat and smooth frequency responses in the co-polarization transmission [23]. Next is the cryogenic low noise amplifier (CLNA) – a multi stage amplifier that has a gain about 30 dB [24]. The outputs of the CLNAs are connected to the warm cartridge where warm LNAs amplify the signal before down conversion. The down converted signal is amplified again before sampling. However, more isolators and amplifiers may be used after the low noise amplifier to prevent LO signals from leaking back to the antenna and disturbing adjacent receivers as well as reducing the standing wave ratio between amplifier and mixer.

If the LNAs are low noise and have enough gain and are followed by a mixer that has high conversion gain, high LO-to-RF isolation and good input matching, then the isolator and extra buffer amplifiers can be removed to simplify the system architecture as shown in Figure 1.4 (b). It is important to note that unlike the LO and RF leakage to the IF path, the LO-to-RF leakage cannot be readily resolved by using a filter. The LO and RF frequencies are close and are only a few GHz apart in the mm-wave frequency band, and the LO frequency range overlaps the RF band. Thus, a fixed frequency filter is not practical for tunable LO operation. A common method employs subharmonic mixers [25] [26] where the RF and LO subharmonics are separated and the LO to RF leakage can be suppressed by using a simple filter. However, they require high LO power and are associated with conversion loss. Moreover, if the mixer provides adequate LO-to-IF isolation, the band

pass filter can be removed from the receiver, resulting in fewer components required. Another important factor that conventional mixers [27] [28] [29] lack is the capability of operating with low LO power. Those designs require at least 0 dBm LO power to operate properly to provide conversion loss of less than -15 dB. A down-converter system that operates with lower LO power is beneficial, especially in large array radio telescope systems. A 1-dBm difference in LO power may seem small in a linearly polarized single dish telescope but it becomes significant when multiplied by the number of polarizations, sub-bands, bands and antennas of a large array of radio telescopes. The capability of

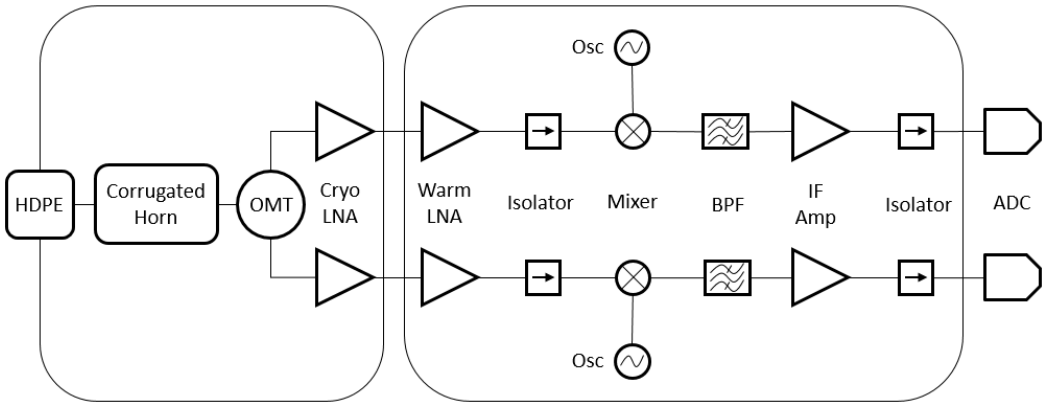

(a)

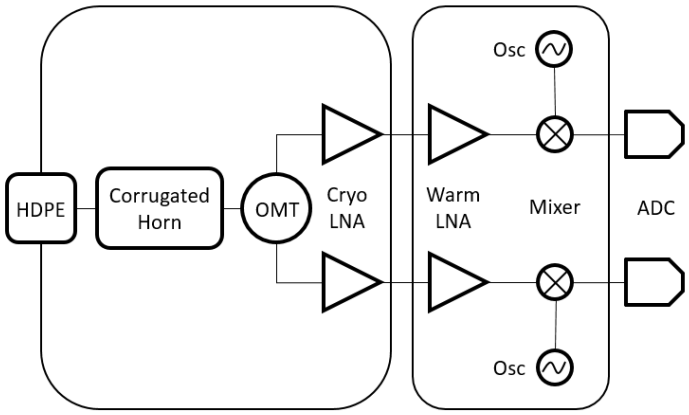

(b)

Figure 1.4. System block diagram of a typical super-heterodyne radio receiver front end, with isolators and bandpass filters. (b) Simplified super-heterodyne receiver that employs high gain low noise LNAs and a down-converter mixer with conversion gain, high LO-to-RF/LO-to-IF isolation and good input matching.

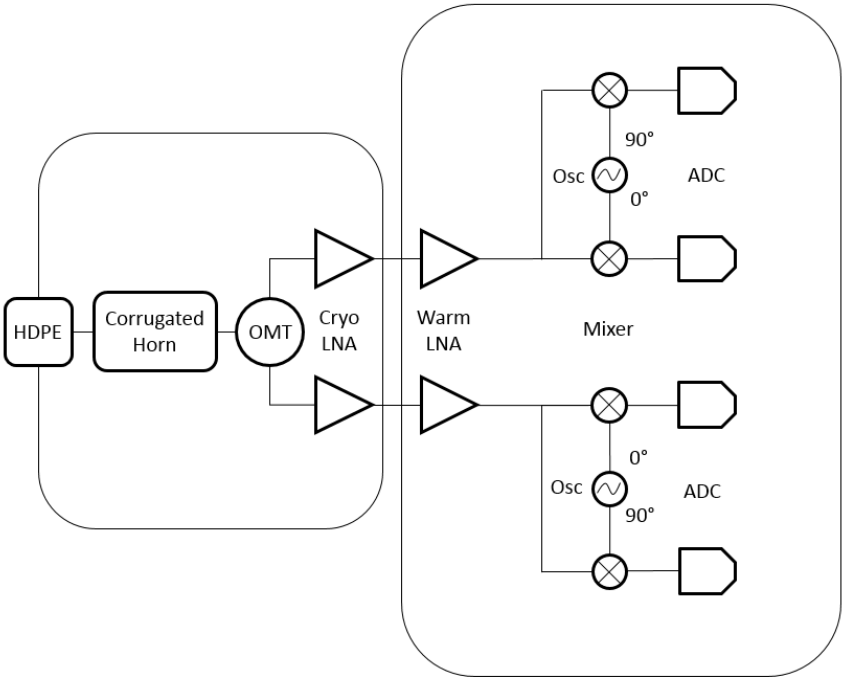

Figure 1.5. System block diagram of a direct conversion radio receiver

operation with low LO power reduces the complexity of the LO distribution system, especially in large telescope arrays with hundreds of receivers.

In case of direct conversion receiver architecture, the RF signal is split in-phase and multiplied by two LO signals that are 90° out of phase to generate in-phase (I) and quadrature (Q) components to be processed at baseband as shown in Figure 1.5. This requires quadrature LO generation of I/Q mixers that have the ability to create the quadrature LO internally. All ngVLA receiver are expected to employ direct conversion architecture and, except Band 1 that will be directly digitized, all other five require down-converting mixers.

1.3 MMIC and RFIC Technology in Radio Astronomy

Similar to radio astronomy, the transistor was born in the Bell Telephone Laboratories in 1947 to replace vacuum tubes which were problematic regarding power consumption, stability and longevity. It only took 12 years for the concept of the integrated circuit (IC) to be introduced by Jack Kilby of Texas Instruments in 1959 [30][31] [32]. And, six years later in 1965, Jim Turner fabricated the first GaAs field effect transistor (FET) with 24 μm

gate length at Plessey Research in the United Kingdom [33]. At the same time, this was also achieved by C.A. Mead at the California Institute of Technology in the United States. Finally, in 1976, the first GaAs monolithic microwave integrated circuit was fabricated by J.A. Turner and R.S. Pengelly using a FET working in the 7 – 12 GHz range [34].

The word monolithic (from the Greek word $\mu ονολιθικος$) means "as a single stone" and describes the fundamental characteristic of MMICs which is fabrication from a single piece of semiconductor material [30]. It mostly refers to III-V based integrated circuits such as GaAs, InP, InPb, InGaAs and GaN circuits that have been used at microwave and millimeter frequencies. Note that the term "RFIC" was traditionally used for Si based integrated circuits that operated in the low gigahertz regime. However, due to great advances in Si CMOS and SiGe BiCMOS processes, especially with the introduction of Cu back end of line (BEOL) and thick top metal layers, the existing RFICs can operate well above 100 GHz. Thus, the different names are used to differentiate the semiconductor technology used for IC fabrication (Si, SiGe vs. III-V) rather than the frequency capability.

MMICs and RFICs such as low noise amplifiers, mixers, oscillators, and power amplifiers have been developed, prototyped, and finally commercialized up to W-band in recent years. They may also incorporate various microwave passive circuits such as matching circuits, filters, power dividers and couplers, usually based on distributed circuit techniques, to develop a higher level of complexity. Wireless systems operating at 120 and 140 GHz also have been proposed which are in the research phase [35] [36] [37] and will be commercialized in the near future. This has been accelerating with the newer Si technology nodes that have cut-off frequencies above 300 GHz [18] [38] [39].

Among group III-V semiconductors, InP and GaAs have characteristics which make them a good solution for radio astronomy circuitry. InP offers the lowest noise reported at cryogenic temperatures at frequencies as high as 50 GHz [40]. GaAs technology has evolved in the past years and not only is now a reliable process in the millimeter-wave range, but achievements in decreasing the gate length continue to push performance to even higher frequencies. Today, a 20 nm gate length HEMT can operate up to 740 GHz with an f_{max} of 1040 GHz [41].

SiGe heterojunction bipolar transistors (HBTs) have been integrated with standard Si CMOS to form a BiCMOS process that shows very high frequency performance up to 500 GHz of f_T and 700 GHz of f_{max} [42]. The HBT devices can be used for high frequency front ends while the digital and control blocks are realized in CMOS.

Table 1.1 shows the state-of-the-art technologies available in industry regarding operational frequency and noise figure. A radio telescope can take advantage of each technology where it has strength. The InP and GaAs mHEMT cryogenic LNAs show the best cryogenic noise temperature; GaAs pHEMT have the best price/performance for warm amplifiers, and SiGe BiCMOS mm-wave mixers can greatly simplify the receiver architecture by offering the best performance and highest level of integration.

The next generation of radio telescopes are large arrays that include hundreds of antennas expanding over thousands of kilometers to provide scientists with the highest resolution and sensitivity. Thus, they must utilize simpler and more robust architecture to be cost effective and successful in their mission.

1.4 Thesis Outline

This work is dedicated to research and development of critical building blocks using the best available semiconductor technology suitable for each block for future radio astronomy instruments in the 1-120 GHz range such as ngVLA and CHORD radio telescopes. The focus is on designing very low noise amplifiers at UHF band (0.3-1.5 GHz), Ku band (12-24 GHz), Ka Band (18-36 GHz) and Q Band (30-52 GHz) based on GaAs mHEMT, GaAs pHEMT and InP HEMT, and millimeter wave down converters for Q band (35-50 GHz) and (33-55 GHz) and W band (70-120) based on SiGe BiCMOS and GaAs pHEMT technologies. Detailed design procedures of three LNAs including the packaging effect modeling are explained, and the results of simulations and measurements for these chips are presented in the following chapters.

In Chapter 2, the four semiconductor technologies that are used in this research, GaAs pHEMT, GaAs mHEMT, InP HEMT and SiGe HBT are reviewed, and the operation of transistors are explained. Moreover, the key features of the used processes are presented. In Chapter 3, the theory of LNA design is presented and the requirements for four LNAs at UHF, Ku, Ka and Q bands are defined. The design procedure is described, and the results are presented. In Chapter 4, the design procedures and techniques of mm-wave down-converter mixers are explained, and the three down-converter chips at Q and W bands based on GaAs pHEMT and SiGe BiCMOS are presented. In addition to the core mixer, the layout design and EM modeling of the critical on-chip passive structures such as transformers, baluns, Lange coupler, Wilkinson power divider, microstrip line and coplanar waveguide (CPW) are presented.

Finally, the results of fabrications and measurements are reviewed in Chapter 5 where the importance of multi-block MMICs and RFICs are described. Ultimately, the outcome of the thesis is discussed and an outline is drawn for future work.

Table 1.1. Features of different transistor technologies.

Technology	Typical feature size	f_T	Minimum noise figure (approximated based on reported noise figure)
InP HEMT	0.15-0.05 μm	200-400	0.4 dB @ 10 GHz [15] 1 dB @ 50 GHz [40] 2 dB @ 100 GHz [43] for 35 nm gate length
GaAs mHEMT	0.1-0.05 μm	200-300	1 dB @ 45 GHz [44] 3 dB @ 140 GHz [45] for 40 nm gate length
GaAs pHEMT	0.15-0.1 μm	100-200	0.5 dB @ 5 GHz [12] 1.2 dB @ 20 GHz [46]
SiGe HBT	0.25-0.13 μm	200-300 GHz	1.5 dB @ 22 GHz [47] 3.5 dB @ 100 GHz [11] 4 dB @ 140 GHz [48]

This thesis has been done in close collaboration with the Radio Instrumentation Group of the NRC Herzberg Astronomy and Astrophysics Research Centre and NRC Advanced Electronic and Photonic Research Centre.

1.5 Contributions

Reducing system the noise temperature and increasing the operational bandwidth of a radio telescope are cost effective ways to improve the receiver's signal to noise ratio without having to build larger dishes or increase the number of antennas in arrays. The contributions of this research are focused on developing practical techniques to reduce components' noise, increase their gain (for LNAs), and widen their bandwidth of operation. These techniques address the shortcomings of conventional methods that are not applicable to radio astronomy or not adequate for mm-wave frequencies.

Conventional packaging methods for electronic chips such as the quad flat package (QFP), quad flan no-lead (QFN), and ball grid array (BGA) are not suitable for radio astronomy applications since they are susceptible to failure in thermal cycling. Similarly, flip-chip bonding suffers from reliability issues when it goes through a cooling procedure. The standard procedure in cryogenically cooled receivers is to place components on copper alloy chassis. The copper has high thermal conductivity which is necessary to achieve the target temperature in the cooling process. However, unwanted waveguide modes could get excited inside the main channel (were the chip and transmission lines are placed) or the pockets of the chassis resulting in gain drop in the amplifiers and resonance in S-parameters of RF chips. Moreover, the wire bonds that connect the microstrip lines to the chip input/output pads introduce inductance that degrades the chip performance. This research employs a co-design method that includes the packaging (chassis effect and wire bond) through the design phase. Along with designing each MMIC/RFIC, a custom chassis is designed and modeled separately to ensure no resonance occurs at frequencies well above the highest operation frequency of the chip. Accurate 3D models of the assembled chip in the chassis were simulated to predict the packaging quality of each design. This co-design method includes the full EM model of the wire bonds in the design phase of input/output matching networks to consider any high frequency degradation. The boding effect is substantial in the millimeter wave frequency range, so a double-wire bond technique was

used to reduce the inductance of the connection. To further improve the performance of the packaged chip, bonding pads on the chip were sized to provide a capacitance that resonates with the reduced inductance of the double-wire bond and high frequencies and cancels its effect. This method automatically solves the bond pad capacitance issue and where the larger area allows two wires to be bonded on one pad. The Q-band GaAs mHEMT LNA, presented in Section 3.5 employs a resonance-free chassis with compensated double-wire bond. The LNA shows wideband gain, noise and return loss performance with minimum degradation at high frequencies. The co-design approach and chassis modeling is performed for other LNAs as well. A three-port chassis has been designed for the GaAs mixer presented in Section 4.3.

The SiGe technology used to design two millimeter-wave mixers in Section 4.2 and 4.4 offers a 7-layer metal stack up. The top two metal layers are thick and used for high frequency interconnection. However, the device models only include the first metal connection. The interconnection from the device to the top metal should be added to the device manually. A common practice is to extract the RC model of the interconnection with limited accuracy for millimeter wave frequency. In this work, however, a full 3D EM model of the interconnection from the most top metal to the device contact points is developed. Different versions of the interconnections are designed, each optimized to bandwidth or noise purposes. The metal stack-up is also used to define microstrip and grounded coplanar waveguide (GCPW) structures on the surface of the chip. Low loss compact structures are developed and a transition structures from bond pad to microstrip line is designed to minimize the effect of the bond pads. Both mixers utilize these techniques to achieve high conversion gain, low LO power and high isolation.

The GaAs and SiGe based chips in this research are designed based on ready-to-use process design kits (PDK) provided by the fabrication foundries, so the effort is entirely devoted to the design procedure. However, at the time of designing LNAs for this research, there was not a stablished PDK for the NRC InP MMIC technology. Therefore, it required extensive effort on transistor design, photolithography mask design, DC and RF measurements, small signal modeling, noise modeling, and passive components (resistor, capacitor, and inductor) modeling. All test structures and setups had to be designed and verified by

measurements before starting the LNA design process. This is a cortical step for process development.

The research on designing millimeter wave SiGe down-converter mixers in Section 4.2 and 4.4 is recognized by NRC as novel work, and a patent is being filed with 100% contribution of the author.

1.6 Publications

So far, this work has contributed to the following publications:

1. R. Ma, J. Lapointe, C. Storey, P. Poole, F. Jiang, A. Seyfollahi, A. W. Walker, J. Noël, A. Kam, and A. Densmore. "Impacts on access resistance of InP high electron mobility transistors from wafer processing." *J. Vacuum Science & Technology B, Nanotechnology and Microelectronics: Materials, Processing, Measurement, and Phenomena* 38. 2, 2020.

This paper studies the access resistance between metal contact and 2DEG in InP HEMT transistors. The contribution to this paper was designing various RF transistor geometries. The devices were fabricated and measured in AEP. The transistor models were used to design the LNAs presented in Section 3.3 and 3.4 of this dissertation.

2. A. Seyfollahi, N. Jiang, D. Garcia, and J. Bornemann, “UHF wideband GaAs MMIC LNA,” *Proc. IEEE 19th Int. Symp. Antenna Techn. Applied Electromagnetics*, pp. 1-2, Winnipeg, Canada, Aug. 2021.

This publication was the result of the effort on design and packaging of a UHF LNA presented in Section 3.2. The paper covers the design techniques and shows wideband gain, and very good input/output return loss and noise figure performance.

3. A. Seyfollahi, N. Jiang, L.B.G. Knee, and J. Bornemann, “Wideband SiGe Down-Converter for Radio Astronomy Applications,” accepted (09 Sep 2022) for publication in *Journal of Astronomical Telescopes, Instruments and Systems.*

The design of the SiGe mixer in Section 4.2 was presented as down-converter with high performance suitable for the DVA-2 radio telescope Q-band and a technology demonstrator for ngVLA band 5.

4. S. Salem Hesari, D. Henke, V. Reshetov, F. Jiang, A. Seyfollahi, L.B.G. Knee, L. Baker, J. Bornemann, and D. Chalmers, “Q-band receiver system design for the Canadian DVA-2 radio telescope,” *Proc. SPIE 11453 Astronomical Telescopes & Instrumentation*, pp. 1-16, Digital Forum, Dec. 2020.

This paper presents a system design for the Q-band of the DVA-2 radio telescope. The main building blocks of the receiver are individually discussed, and each section is authored by the responsible design engineer. The LNA and mixer presented in Section 3.5 and 4.2, respectively, were introduced in this manuscript. The custom chassis designed for the mixer is also presented.

5. S. Salem Hesari, D. Henke, V. Reshetov, B. Veidt, A. Seyfollahi, F. Jiang, L. Knee, “Design and Analysis of the NRC Q-Band Receiver for the ngVLA Band-5,” *SPIE Astronomical Telescopes & Instrumentation*,” June 2022.

The mixers in Section 4.2 and 4.3 and the Q-band LNA in Section 3.5 are introduced as key components of the developed receiver for ngVLA band 5. The paper describes the overall receiver architecture where key components are individually discussed.

6. D. Henke, F. Jiang, S.S. Hesari, A. Seyfollahi, B. Veidt, L.B.G. Knee, “Octave bandwidth receiver technology for radio and millimetre-wave telescopes,” *SPIE Astronomical Telescopes & Instrumentation*, June 2022.

This paper presents the technology for octave band radio receivers. Individual octave band components are studied for the receiver chain where the results of the work on designing octave band LNA, presented Section 3.3 and 3.5, are used to develop wideband LNAs for this work.

Chapter 2

Semiconductor Technologies

Silicon has been the dominant semiconductor technology in the electronic world for two main reasons. First of all, Si is cheap; low price is a convincing factor for both designers and manufacturers to work with Si. The second cause which makes Si more desirable is the oxide of Si. Chemical interaction of pure Si with oxygen creates a thin defectless oxide which sticks to the upper layer of Si and covers it uniformly. This oxide protects the Si and is used to form a metal oxide semiconductor (MOS) connection. The oxide layer is pure and its thickness can be controlled accurately, whereas the oxides of compound semiconductors are usually inferior and non-functional for electronic device implementation. This is why metal oxide semiconductor devices have not been developed based on group III-V semiconductors. Moreover, p-type FETs based on Si have acceptable performance (close to n-type) which allows the realization of complementary MOS (CMOS) circuitry, while there is a significant challenge to identifying high mobility III-V p-type FET candidates [49] [50] [51]. These advantages made silicon the foremost

semiconductor technology for digital and low frequency analog integrated circuits. However, due to lower electron mobility and resistive substrate and other scaling issues [52], Si did not provide the high frequency performance for mm/sub-mm wave integrated circuits. Although the operation frequency of Si based RFICs are expanding to the mm-wave domain, the intrinsically higher noise is still one of the main reasons that Si has not been widely used in high frequency radio instruments. On the other hand, the introduction of a new microwave transistor technology, almost every decade, enabled microwave designers to design high frequency integrated circuits from the early days of integrated circuits:

- GaAs metal-semiconductor field effect transistors (MESFET) in the 1970s
- III-V HEMTs and HBTs in the 1980s
- SiGe BiCMOS in the 1990s
- GaN HEMT in the 2000s
- New generation of MOFETs (LDMOS, SOI, FinFET) in the 2010s that incorporate some compound and heterojunctions material that allowed Si-based technologies to enter the mm-wave realm.

In particular, III-V HEMT technologies offered a combination of high frequency and low noise characteristics that made them the primary technology choice for radio astronomy. Elements of column III (Al, Ga and In) and column V (N, P, As and Sb) of the periodic table have been used to create compounds with higher electron mobility. From twelve possible combinations, GaAs, InP and GaN are the most important ones. III-V semiconductors can also be formed from more than two elements. Ternary compounds are made of a single V (III) element and a combination of two III (V) elements in form of $III_xIII_{1-x}V$ ($IIIV_xV_{1-x}$) such as InGaAs, AlInAs, and AlGaAs (GaAsP and InAsSb).

Table 2.1 shows the effective mass and electron mobility of a few semiconductors. III-V compounds have smaller effective mass and higher electron mobility which makes them a fitting solution for high frequency applications.

Electron mobility and peak velocity determine how fast the electrons react to the applied electromagnetic field and directly affect the frequency response of the device. When an electron is presented in an electric field, it is subject to a force equal to

$$\vec{F} = -q\vec{E} \tag{2.1}$$

and it accelerates in the opposite direction of the electric field and achieves the drift velocity of

$$v = -\left(\frac{q\tau_c}{m^*}\right)\vec{E} \tag{2.2}$$

$$\mu_n = \left(\frac{q\tau_c}{m^*}\right) \tag{2.3}$$

$$v = -\mu_n\vec{E} \tag{2.4}$$

where τ_c is the mean free time between collisions and m^* is the electron effective mass. The proportionality factor μ_n is the electron mobility.

On the other hand, III-V compounds have a smaller band gap compared to Si, leading to high leakage current. The energy band gap of the semiconductor is essential for power handling characteristics. For example, InSb has extremely high electron mobility but the band gap of 0.17 eV makes it less attractive because the transistor cannot deliver enough gain to the output of the device although the electrons move fast.

Table 2.1. Semiconductor characteristics.

	Si	Ge	GaAs	InP	InAs	InSb	GaN
Effective mass	0.19	0.08	0.067	0.08	0.023	0.014	0.37
Electron mobility (cm^2/Vs)	1300	3900	5000	4500	40000	77000	1500
Band gap energy (eV)	1.12	0.66	1.42	1.35	0.36	0.17	3.39
Permittivity	11.7	15.8	13.4	12.4	14.8	17.7	9

In this chapter, we review the characteristics of III-V semiconductors with focus on GaAs pHEMT, InP HEMT and GaAs mHEMT technologies as well as SiGe BiCMOS which are used in the design of MMICs and RFICs in this research for radio astronomy applications.

2.1 III-V HEMT

Among III-V semiconductors, GaAs is the most popular material: first created by Goldschmidt in 1929, it was only in 1952 when GaAs was considered as a semiconductor in the electronics world [53]. The GaAs crystal has a sphalerite or zinc blend structure. Based on quantum mechanics theory, electrons inside the crystal are allowed to have ranges of energies called valence and conduction bands. Electrons can be in these two energy levels if they possess adequate energy. However, these two energy bands are separated by the energy band gap. If an electron has sufficient energy, it is probably able to make a transition from the valence band to the conduction band. This probability is governed by the Fermi distribution function, and the Fermi level is the level of energy at which the probability of transition to the conduction band is 0.5. For an undoped semiconductor, the Fermi level is in the middle of the gap [54] [55].

In GaAs, the minimum of energy for the conduction band is aligned with the maximum of energy for the valence band or, in other words, GaAs has a direct band gap. In contrast, Si has an indirect band gap. This means that for electrons inside Si to move to the conduction band, not only the increase of energy level is necessary, but electrons have to change momentum as well. This is a major disadvantage in optoelectronic applications. On the other hand, GaAs electrons can emit photons when they change energy levels from the conduction band to the valence band, and they can move to the conduction band from the valence band by absorbing photons. This allows GaAs to be used in photo detectors.

The resistivity of the semiconductor substrate is another important factor in electronic applications. When the substrate is a semi-insulator, it affects the quality factor of the passive circuit components. Practically, the resistivity range for GaAs substrate is 10^{-3} Ωcm to 10^{8} Ωcm [55].

One of the earliest works available in the literature based on modern GaAs technology goes back to 1980 [56], where a Molecular Beam Epitaxy (MBE) grown $GaAs - Al_xGa_{1-x}As$

heterostructure was used to achieve an electron mobility of 6200 cm^2/Vs at room temperature. Five years later, in 1985, the concept of band-gap engineering was developed where the technique of mixing different semiconductors was used in order to achieve specific solid-state features from transistors which led to the development of high electron mobility and heterojunction bipolar transistors [30].

Figure 2.1 shows a simple view of a heterostructure commonly used in HEMT devices. In this structure a selectively undoped AlGaAs layer is placed between n-doped AlGaAs and undoped GaAs layers. Due to the higher electron affinity of GaAs, free electrons in the n-doped AlGaAs are transferred to the undoped GaAs layer where they form a quasi-two-dimensional Fermi gas. Electrons move toward the GaAs side of the interface and deplete the AlGaAs layer and leave positive ions behind as shown in Figure 2.2. The resulting mobility is higher than that of uniformly doped GaAs of equivalent doping concentration.

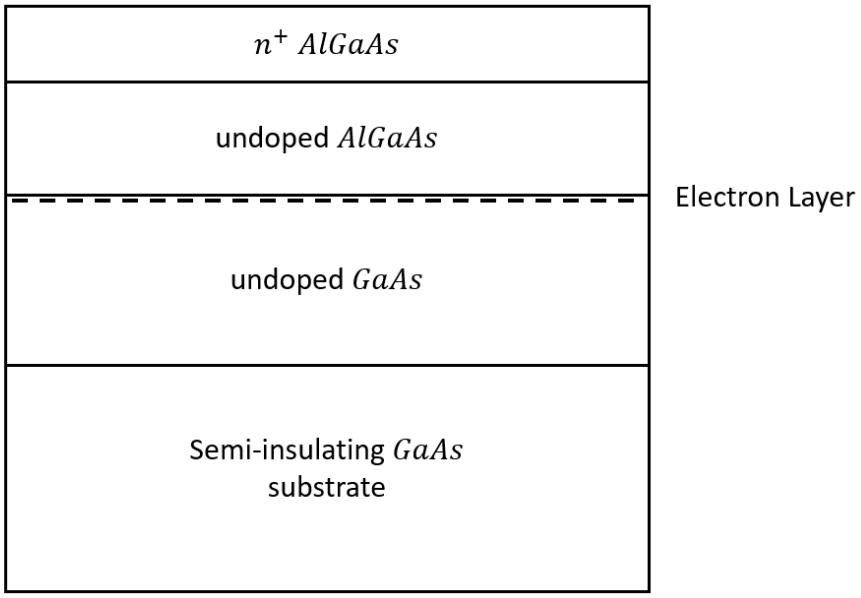

Figure 2.1. A generic HEMT heterostructure.

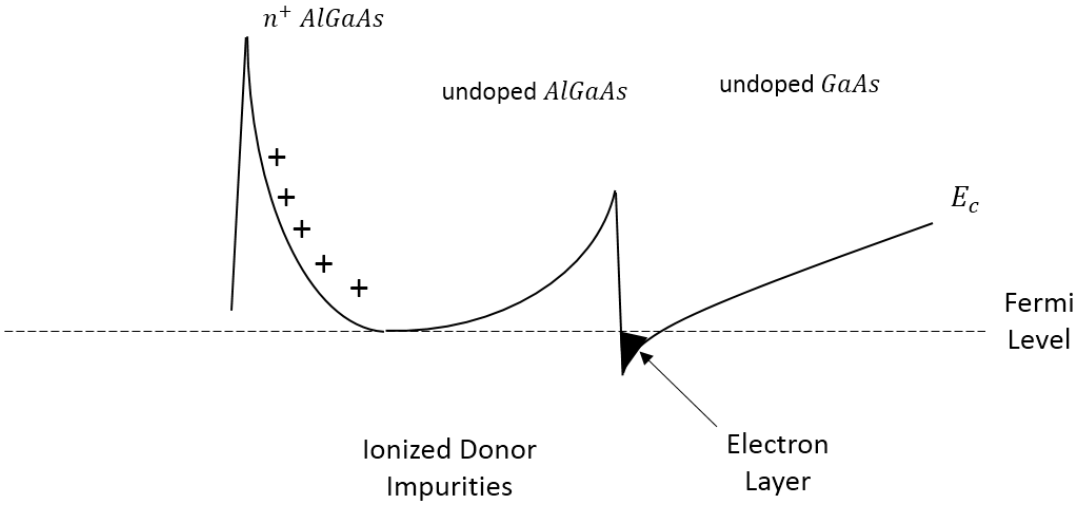

Figure 2.2. Energy band diagram of heterostructure.

The mobility enhancement is due to spatial separation between electrons and their parent donor impurities. The GaAs substrate must provide thermal stability during epitaxial growth or annealing of ion-implanted active layers, and lowest possible density of crystalline defects, such as dislocations and stacking faults. The active layer also should not have degradation due to out-diffusion of impurities from the substrate during thermal processing. To guarantee these requirements, a buffer layer is added in the epitaxial

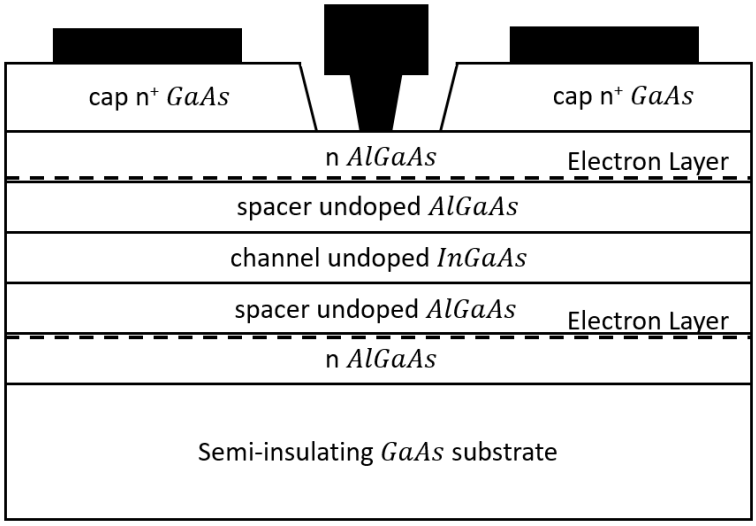

Figure 2.3. Epitaxial structure of a typical double delta-doped GaAs pHEMT

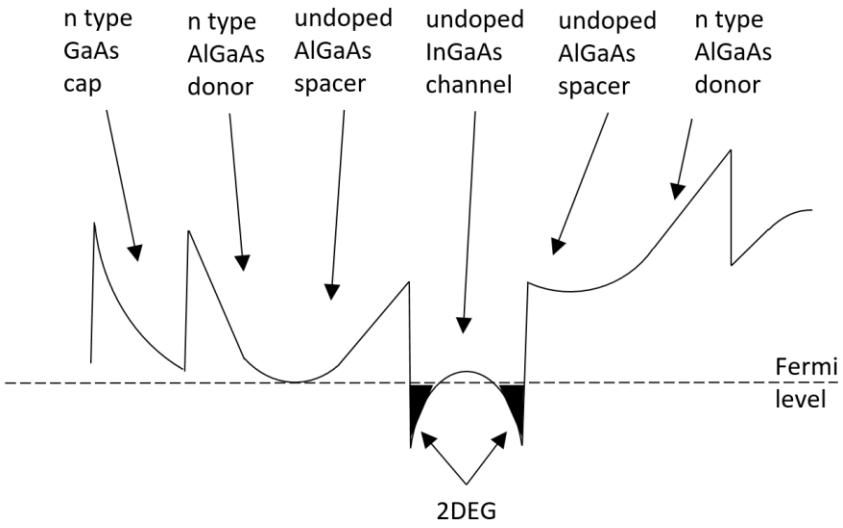

Figure 2.4. Conduction band diagram of the double heterojunction GaAs pHEMT.

structure. It is a relatively thick, high resistivity layer grown in the semi-insulating substrate to provide a physical barrier against undesirable substrate impurities and imperfections.

2.1.1 GaAs pHEMT

A typical GaAs pHEMT consist of double side doping to achieve high current density. The cross section of such a structure is sketched in Figure 2.3. The epitaxial structure consists of a thin, undoped InGaAs channel layer with high indium concentration. Double delta-

doped layers provide carriers to the channel. AlGaAs spacer layers are grown above and below the channel layer. An AlGaAs Schottky layer is placed on top of the upper spacer layer.

An additional supply of doping is introduced below the channel which results in doping carrier concentration of Two Dimensional Electron Gas (2DEG) with proportional increase in the drain current for a given gate width. This increases the power handling capability of the HEMT. The conduction band diagram of the double heterojunction GaAs pHEMT is shown in Figure 2.4.

As discussed in [57], WIN 0.15 μm pHEMTs Ohmic patterns are defined by stepper lithography, and Au/Ge/Ni/Au metals are evaporated in the contact regions in order to have good ohmic contact, and sintering is performed using rapid thermal annealing with optimized conditions. Low contact resistance (R_c) of 0.1 Ωmm is achieved.

Once the gate is patterned, the device is fully passivated by SiN of 100 nm thickness. Resistors are provided using both epitaxial layers and TaN thin films. The former one delivers MESA resistors with sheet resistance of 250 Ω/sqr, and the latter one is used for thin film resistors (TFRs) with a sheet resistance of 50 Ω/sqr.

A MESA type structure stands up above the substrate. In other words, the substrate is etched back to leave the resistor (or transistor) isolated from the surrounding material. This is usually done to stop parasitic capacitance. The metal-insulator-metal (MIM) capacitor has a capacitance of 6000 pF/mm^2. Optional protection silicon nitride layers provide handling robustness. Wafers are thinned to either 100 μm or 50 μm for improved thermal and RF performance.

The WIN 0.15 μm pHEMT process also shows high reproducibility and uniformity from wafer to wafer and lot to lot with DC and RF yields exceeding 90% based on the document published by the foundry. The WIN 0.15 μm pHEMT process is very suitable for low noise amplifiers at millimeter-waves [58]. The gate yield of each wafer for the WIN 0.15 μm pHEMT has been evaluated using 12 × 75 μm devices for the specification of 50 μA/mm in drain current defined at grounded source, -2 V gate bias and 1.5 V drain bias. Measurements across 6-inch GaAs wafers show normal FET characteristics with

Table 2.2. Main parameters of the 150 nm pHEMT technology from [57].

Parameter	Symbol	Unit	Value
Contact Resistance	R_c	Ωmm	0.1
Maximum drain current @ V_{gs} = 0.5 V	I_{max}	mA/mm	410
Threshold voltage @ I_{ds} = 1 mA/mm	V_t	V	-0.9
Maximum transconductance	g_m	mS/mm	690
Maximum cut-off frequency	f_t	GHz	92
Gate-drain breakdown @ I_{gd} = 1 mA/mm	V_{bgd}	V	11.5

satisfactory drain current pinch off. The typical parameters of a pHEMT are presented in Table 2.2. An extrinsic transconductance of 690 mS/mm and V_t of -0.3 V with f_t of 92 GHz is routinely reported on 6-inch GaAs substrates. The drain current density (I_{DSS}) at V_{gs} = 0 V is 80 mA/mm, and the saturation drain current density (I_{dmax}) at V_{gs} = 0.5 V and V_{ds} = 1.5 V is 410 mA/mm. The typical drain-to-gate breakdown voltage, V_{gd}, is 11.5 V. This is defined at I_g = 1 mA/mm. The f_t and f_{max} have uniform distribution across a 6-inch GaAs wafer. The typical f_{max} is around 209 GHz.

2.1.2 InP HEMT

InP has the unique property of high electron mobility in the channel, lower electron effective mass in the quantum well, high 2DEG electrons in the channel and transconductance that makes it the ultimate semiconductor technology for radio astronomy low noise amplifiers [59] [60] [61] [62] [63]. However, the smaller size of the InP wafer (maximum of 3-4 inches), and yet being very brittle, has caused difficulties in the production in high volume. Also, the difficulty in etching the InP substrate is another factor contributing to the low fabrication yield of InP HEMT devices. The high fabrication cost, which is 3-4 times higher compared to GaAs, is another downside to producing InP substrates [64] [65] [66] [67] [68] [69] [70] [71] [72] [73].

Figure 2.5 shows an example of an InP HEMT [59]. The conduction band diagram of the InP HEMT is shown in Figure 2.6.

At NRC HAA, in collaboration with the NRC Advance Electronic and Photonic research (AEP) center, an InP process has been developed for mm-wave radio astronomy low noise amplifiers. As described in [59], a highly doped InAlAs layer has been used to insure good contact from the cap layer to the 2DEG for 3-inch wafers. This results in about 9700 cm^2/Vs electron mobility at 300 K and a carrier density of about 1.2×10^{12} cm^{-2} for the 2DEG.

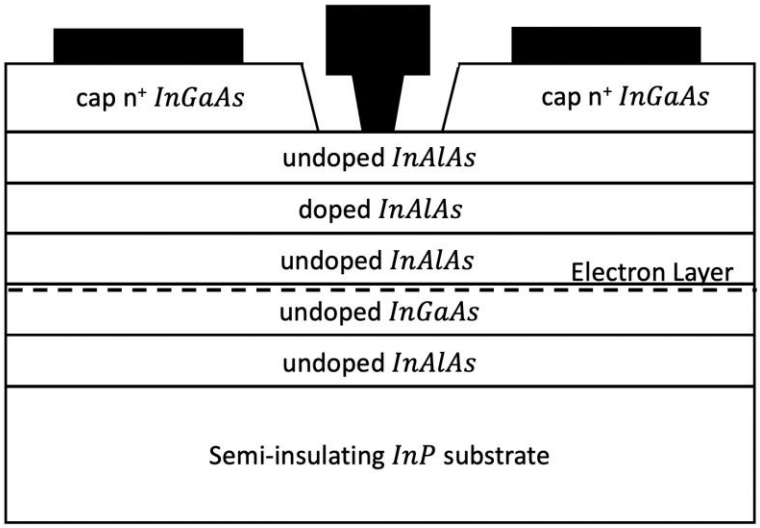

Figure 2.5. Epitaxial structure of a typical InP HEMT.

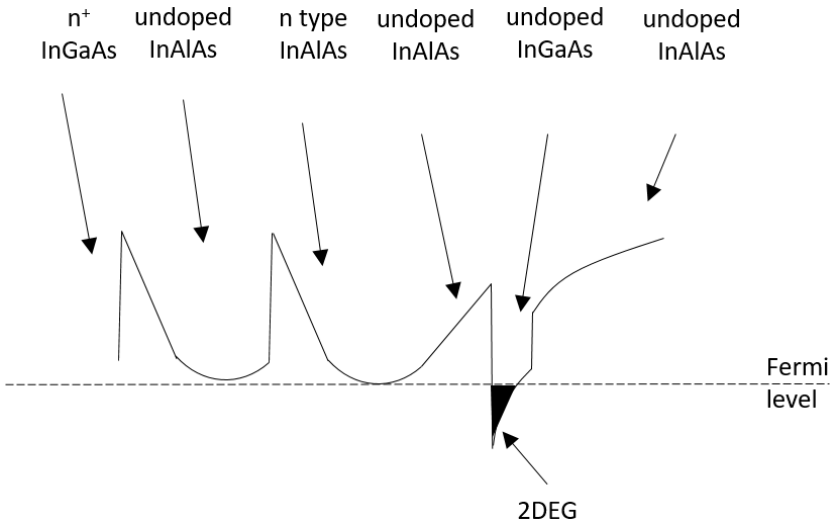

Figure 2.6. Conduction band diagram of a typical InP HEMT.

Also, a low contact resistance of 0.03 Ωmm is achieved by using a Palladium and Germanium (PdGe) metal stack.

Figure 2.7 from [59] shows the scanning electron microscopy (SEM) image of the cross section of a free-standing T-Gate with 50 nm gate length. Table 2.3 shows the main parameters of the process.

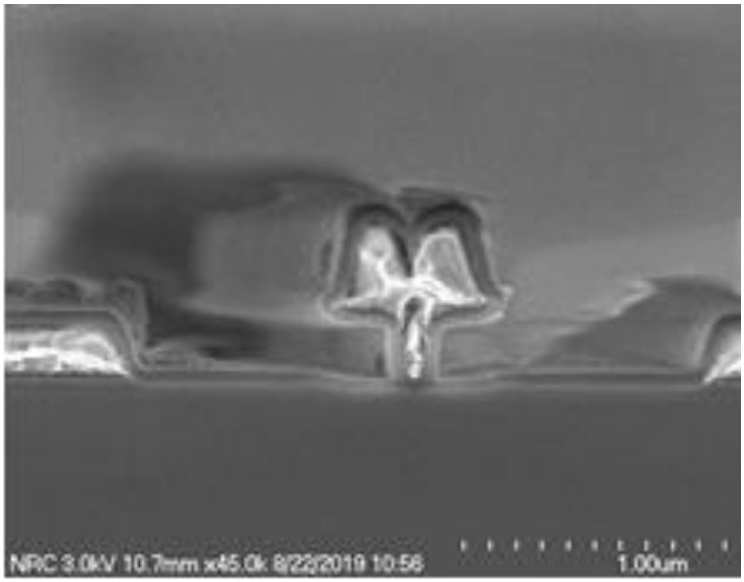

Figure 2.7. SEM image of the cross section of a free-standing T-gate with nominal length of 50 nm from [59].

Table 2.3. Main parameters of the 150 nm InP HEMT technology.

Parameter	Symbol	Unit	Value
Contact Resistance	R_c	Ωmm	0.03
Maximum drain current @ V_{gs} = 0 V	I_{max}	mA/mm	600
Threshold voltage @ I_{ds} = 1 mA/mm	V_t	V	-0.5
Maximum transconductance	g_m	mS/mm	700
Maximum cut-off frequency	f_t	GHz	250
Maximum stable gain @ 10 GHz	MSG	dB	15
Minimum noise figure @ 10 GHz	NF_{min}	dB	0.2

2.1.3 GaAs mHEMT

The original lattice matched HEMT had some disadvantages such the collapse of the I-V curve and sharp peak in the transconductance at lower temperatures which is caused by the presence of donor complex centers in $Al_xGa_{1-x}As$ at layers with $x > 0.23$ [74]. This led to a search for new material systems to improve the device performance and eliminate the outstanding issues which resulted in the use of compositionally graded layers that not only provides high mobility by using an indium-based compound semiconductor but also can be grown on GaAs substrates instead of InP for lower cost, larger size, and is less brittle [75]. This resulted in the introduction of GaAs mHEMT technology in 1988 [76] that has the high frequency and low noise performance of the InP HEMT and the process reliability and maturity of GaAs. Figure 2.8 shows an example of a GaAs metamorphic HEMT [77]. The conduction band diagram of the double heterojunction GaAs mHEMT is shown in Figure 2.9.

The mHEMT also allows for higher output power compared to InP that is an advantage in the development of high linearity low noise amplifiers at high frequencies.

Due to the reasons described above, mHEMT has been a technology of choice to develop low noise amplifiers above 30 GHz in addition to the NRC's InP process. There are two available foundries that offer multi project wafer runs for mHEMT technology: IAF and OMMIC, and the latter has been used to design the cryogenic LNA.

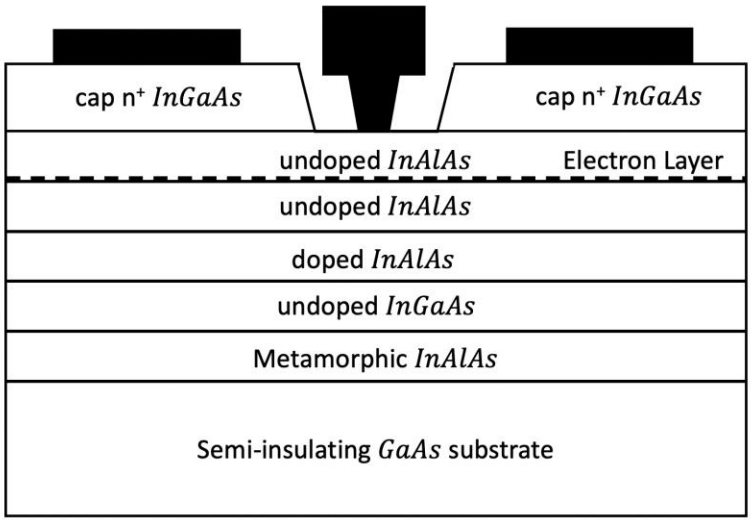

Figure 2.8. Epitaxial structure of a typical metamorphic GaAs mHEMT.

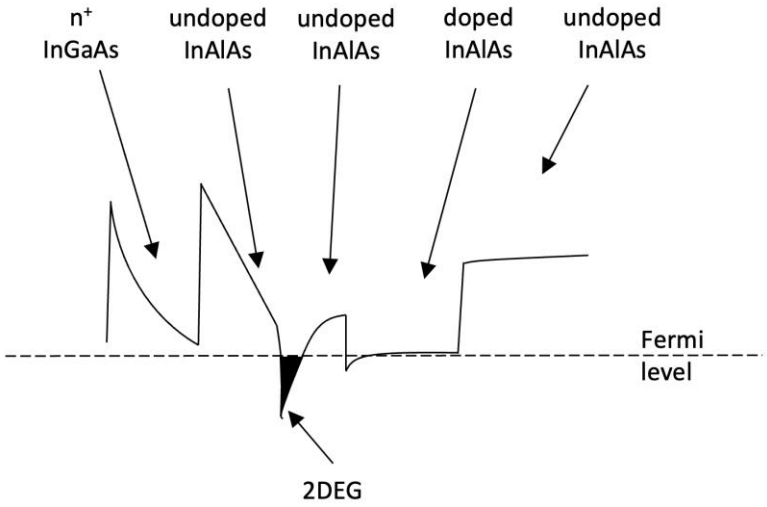

Figure 2.9. Conduction band diagram of a typical metamorphic GaAs.

Table 2.4. Main parameters of the 70 nm mHEMT technology from [78].

Parameter	Symbol	Unit	Value
Contact Resistance	R_c	Ωmm	0.2
Maximum drain current @ V_{gs} = 0.2 V	I_{max}	mA/mm	700
Threshold voltage @ I_{ds} = 1 mA/mm	V_t	V	-0.55
Maximum transconductance	g_m	mS/mm	1600
Maximum cut-off frequency	f_t	GHz	300
Maximum stable gain @ 30 GHz	MSG	dB	17
Minimum noise figure @ 30 GHz	NF_{min}	dB	0.55

As presented in [78], a 70 nm very high indium content of 70% is used to achieve low noise, low power performance at frequencies as high as 150 GHz. Moreover, a composite channel is used with a 53% GaInAs sub-channel to improve the on-state breakdown voltage [78]. The T-gates benefit from double mushroom technology that allows for minimum gate length realization and limits the gate resistance simultaneously [78].

The cut-off frequency of the process reaches up to 300 GHz with the extrinsic transconductance of 1600 mS/mm [78]. Table 2.4 shows the main parameters of the process based on published data in [78].

2.1.4 HEMT Model

When the gate is sufficiently reverse-biased, the 2DEG can be completely annihilated which causes no current flow from the source to the drain, and the device is pinched-off. If the gate is forward-biased (or slightly negatively-biased), a channel of undepleted carriers will be established in the doped AlGaAs, so there are two paths through which current can conduct from source to drain:

a) through the 2DEG

b) via doped and undoped AlGaAs

Since the mobility of AlGaAs is not as high as that of 2DEG, the device performance starts to degrade when it is operating in this mode [79].

The drain-source current can be modeled by using the mobility of the 2DEG in the linear region as

$$I_{ds} = qn_{2DEG}\mu W\frac{V_{ds}}{s} \tag{2.5}$$

where n_{2DEG} and μ are the concentration and mobility of the 2DEG, respectively. W is the device width, and s is the distance between source and drain contacts.

For a HEMT operating at saturation,

$$I_{ds} = qn_{2DEG}v_{eff}W \tag{2.6}$$

where v_{eff} is the effective channel velocity.

Above equations are based on a simplified model of the FET and provide approximate values for the drain-source current. There are other methods for describing the device behavior in nonlinear regions more accurately. Most of the nonlinearities involved in the III-V FETs are due to the bias dependent current-voltage and charge-voltage (*i*-*v* and *q*-*v*) relationships. There are many formulations based on large signal models available in the

literature such as the Curtice model [80], [81], the Angelov (Chalmers) model [82], [83], [84], the EEHEMT1 model [85], etc. Each model has its own strengths and shortcomings in different *i-v* regions of the device.

The Angelov model is one of the most popular models for HEMTs and MESFETs, for which the key parameters are the gate voltage, drain current for maximum transconductance and the coefficient for the peak value of the transconductance. This model accurately describes the device behavior in the intermediate *i-v* region while it does not offer the best solution in saturation and sub-threshold regions. However, some modified models have been proposed to overcome these deficiencies. The empirical *i-v* model of the HEMT is constructed by the product of two functions in the Angelov model [83]:

$$I_{ds}(V_{gs}, V_{ds}) = I_{ds_1}(V_{gs}, V_{ds}).I_{ds_2}(V_{gs}, V_{ds}) \tag{2.7}$$

I_{ds} is to model the drain-source dependent characteristics.

$$I_{ds_1} = I_{pk}(1 + \tanh(\psi)) \tag{2.8}$$

$$I_{ds_2} = \tanh(\alpha V_{ds})\,(1 + \lambda V_{ds}) \tag{2.9}$$

where

$$\psi = P_1.V_{gsp} \tag{2.10}$$

$$V_{gsp} = V_{gs} - V_{pk} \tag{2.11}$$

I_{pk} is the drain current and V_{pk} is the gate voltage at which the maximum of the transconductance occurs, and parameter P_1 can be measured. λ is the channel length modulation parameter, and α is the saturation voltage parameter. If α is small, the transition from the linear region to the saturation region is smooth while for a sharp knee region, α is large. The value of ψ can be expanded into a power series function which is a polynomial expansion of V_{gsp}

$$\psi = P_1.V_{gsp} + P_2.{V_{gsp}}^2 + P_3.{V_{gsp}}^3 + \cdots \tag{2.12}$$

The higher order coefficients such as P_2 and P_3 can be obtained only from an optimization process [82] [83] [84] [85] [86] [87] [88]. The more the power series expands, the more

accurate and the more complex the model will be. The derivative of the drain current with respect to the gate-source voltage is the transconductance of the device.

$$G_m = \frac{\delta I_{ds}}{\delta V_{gs}} = I_{pk}.sech^2(\psi).\frac{\delta \psi}{\delta V_{gs}}.I_{ds_2} \tag{2.13}$$

Based on the Angelov model, G_m has to be symmetric with respect to the peak of G_m while, in practice, the measured G_m is usually compressed. To address this issue, *i-v* models have been developed containing higher-order terms [89] where *Model-2* is the best choice for GaAs and InP HEMT, pHEMT and mHEMT. It includes G_m compression and shows good agreement with measurements for different gate widths and number of fingers.

$$I_{ds_1} = I_{pk}(1 + \tanh(\psi_1)) \tag{2.14}$$

$$I_{ds_2} = \tanh(\alpha V_{ds})\left(1 + \lambda V_{ds} + L_{sb}.exp\left(\frac{V_{dg}}{V_{tr}} - 1\right)\right) \tag{2.15}$$

$$\psi_1 = P_1.V_{gsp} + P_{21}.{V_{eff}}_{P_1}^{\ 2} + P_{31}.{V_{eff}}_{P_1}^{\ 3} + P_{22}.{V_{eff}}_{P_2}^{\ 2} + P_{32}.{V_{eff}}_{P_2}^{\ 3} \tag{2.16}$$

where

$$V_{gsp} = V_{gs} - V_{pk} \tag{2.17}$$

$${V_{eff}}_{P_1} = 0.5\left(V_{gsp} - V_{gspa}\right) \tag{2.18}$$

$${V_{eff}}_{P_2} = 0.5\left(V_{gsp} + V_{gspa}\right) \tag{2.19}$$

$$V_{gspa} = \frac{1}{n}.ln\left(2\cosh\left(n.V_{gsp}\right)\right) \tag{2.20}$$

And adding P_{21}, P_{31} and P_{22} enables the G_m compression.

The values of the small signal model are stablished based on the DC bias condition of the device. The cross section of a HEMT is shown in Figure 2.10. Each element models the electrical feature of a particular part of the device. The resistance of the gate is shown by R_g. The voltage-dependent charge at the source and gate is modeled by capacitance C_{gs}. This capacitance also models the coupling between the T-gate and the source contact which becomes significant as the frequency increases. The gate-drain capacitance C_{gd} is the capacitance associated with the capacitor whose plates are formed by the gate metal and 2DEG. The coupling between the T-gate and drain contact is involved in this capacitance as well. The channel shows a resistance because of limited conductivity of the doped semiconductor, R_s and R_d. The drain-source resistor R_{ds} represents the finite output resistance of the device. The drain-source capacitance C_{ds} is due to capacitive coupling between the doped regions of the drain and the source, separated by the depleted region at n-doped AlGaAs.

An important characteristic regarding RF behavior of the HEMT is that the gate capacitance is relatively constant with the changing gate bias as the "plate" separation is fixed by the thickness of the AlGaAs donor and spacer layers. Current modulation occurs as the charge is added to or removed from the 2DEG in response to variation in voltage applied to the gate.

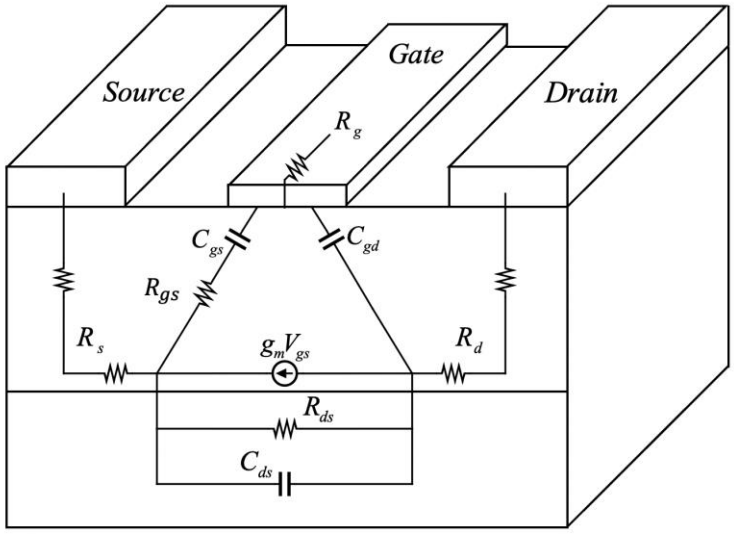

Figure 2.10. Cross section of a HEMT with equivalent lumped elements.

R_s and R_d have two components: the contact resistance of the heavily doped GaAs cap and the bulk resistance of the semiconductor in the access regions. The gate, drain and source parasitic inductances L_g, L_s and L_d arise from the feed pads of the electrodes. The parasitic geometrical capacitances C_1 and C_2 are caused by the electric field distribution between metallic contacts.

The small signal circuit used for the GaAs pHEMT, GaAs mHEMT and InP HEMT in this research is shown in Figure 2.11 where the dashed box shows the intrinsic device. The cut-off frequency f_t at which the current gain of the intrinsic device falls to unity with a shorted output is

$$\frac{i_d}{i_g} \approx \frac{g_m}{j\omega(C_{gs}+C_{gd})} \tag{2.21}$$

$$2\pi f_t(C_{gs}+C_{gd}) = g_m \tag{2.22}$$

$$f_t = \frac{g_m}{2\pi(C_{gs}+C_{gd})} \tag{2.23}$$

Equation (2.23) gives an approximate value for the cut-off frequency. If the contact resistances are considered in calculations, the cut-off frequency will be ($R_1$is neglected)

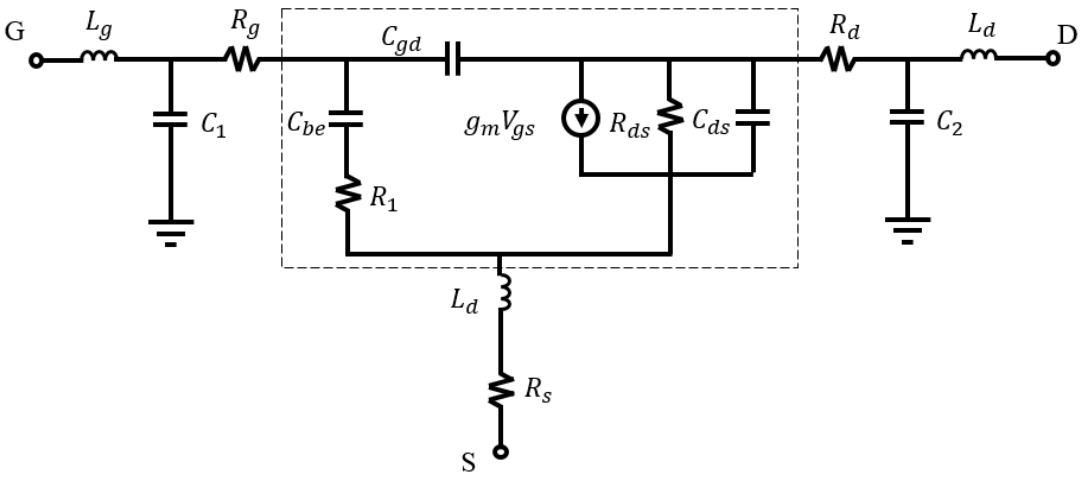

Figure 2.11. Small signal model of GaAs pHEMT, GaAs mHEMT and InP HEMT.

$$f_t = \frac{g_m}{2\pi\left[\left(C_{gs}+C_{gd}\right)+\left(1+\frac{R_s+R_d}{R_{ds}}\right)+g_m C_{gd}(R_s+R_d)\right]} \quad (2.24)$$

Equation (2.24) shows that maximizing the transconductance increases the device's operating frequency range while the gate capacitance and parasitic resistances should be minimized. Based on Equation (2.5) and (2.13), the transconductance is directly proportional to electron mobility, and the gate capacitance can be decreased by shortening the gate length.

2.2 HBT

The heterojunction bipolar transistor was introduced to improve the performance of existing bipolar junction transistors (BJTs) by improving the device current gain (β) through removing hole injection from the base into the emitter as well as employing a large bandgap difference between the base and emitter. Moreover, the carrier transition time was reduced between base and emitter by thinning the base region. Materials with higher electron mobility were used in the base that help to build faster devices. Figure 2.12 shows the cross section of a conventional HBT and Figure 2.13 shows the energy band diagram of the biased HBT.

HBT devices are different from field effect transistors in the principle of operation in two key fundamental characteristics [74]:

- While in a FET the controlling and controlled charges are physically separated and the current consists of one type of carrier (n or p), in a bipolar device both types coexist and contribute to the current.
- The current flow is vertical in an HBT; therefore, the minimum feature size is defined by the thickness of the base layer in contrast to FETs, where the current flows laterally, and the minimum feature size is defined by the gate length. Growing a very thin base layer with a few nanometer thickness is relatively easier compared to fabricating a few tens of nanometer gate using advanced lithography methods. This is the fundamental reason that HBTs can achieve a very high cut-off frequency.

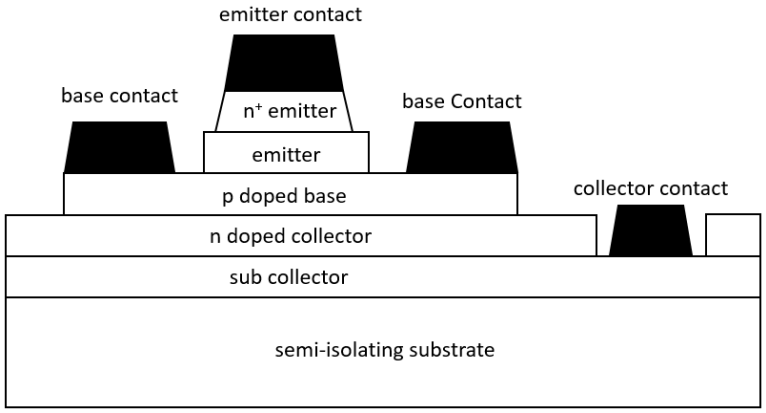

Figure 2.12. Cross-section of a typical HBT.

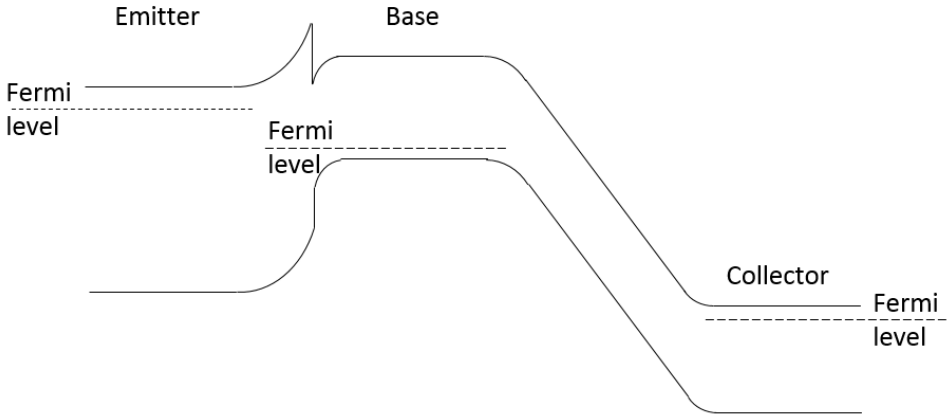

Figure 2.13. Conduction band diagram of a typical HBT while biased in active region.

2.2.1 SiGe BiCMOS

The BiCMOS technology is the result of integration of SiGe HBT with standard Si CMOS. This allows designers to take advantage of fast HBTs in designing mm-wave frontends while benefiting from the high level of integration, low power and small digital blocks of standard CMOS.

As shown in Figure 2.14, SiGe HBTs utilize a graded Ge concentration in the base, n^+ poly silicon emitter, selectively implanted collector (SIC), shallow trench isolation between base and collector, deep trench isolation (DTI) between collector and substrate, and a

heavily doped buried layer as sub-collector. The Ge in the base allows for a high level of doping that is necessary for high electron mobility which is not as high as that of III-V material. The Ge also increases the current gain β and lowers the base resistance suitable for higher f_{max} and lower noise.

The IHP 130 nm BiCMOS process, as described in [90], is used for in this research. The process offers f_t of about 300 GHz and f_{max} of 500 GHz with a variety of devices such as standard NMOS and PMOS, junction varactors, MOS varactors, poly and metal resistors, MIM capacitors, and seven layers of metallization that are crucial for designing mm-wave and low frequency blocks with a high level of integration [91] [92].

The BOEL metals are copper with two thick top metal layers for high Q inductors and low loss microstrip and grounded coplanar waveguide (GCPW) lines.

2.2.2 HBT Model

The HBT is biased in the active region. Assuming a very fast device with a very short base transit time, the collector current density equals [93]

$$I_C = A_E J_S \left(exp\left(\frac{qV_{BE}}{kT}\right) - 1 \right) \left(1 + \frac{V_{CE}}{V_A}\right) \tag{2.25}$$

where:

- A_E is the emitter area

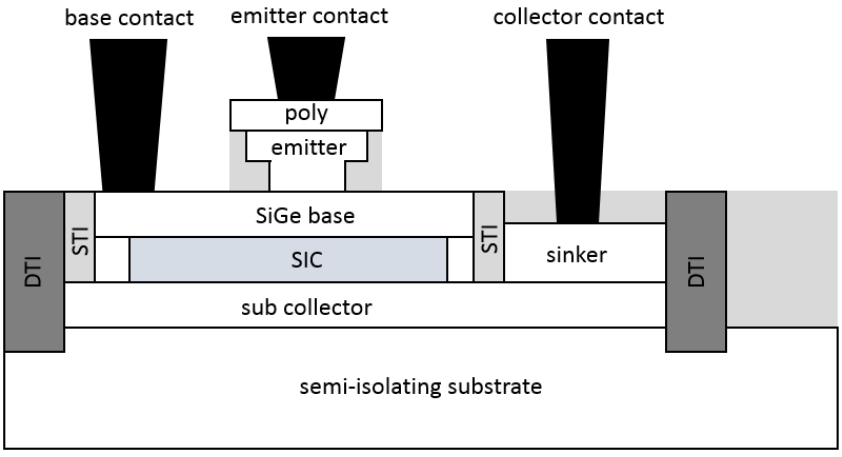

Figure 2.14. Cross-section of a SiGe HBT.

- J_S is the saturation current density
- q is the electron charge
- k is the Boltzmann constant
- T is the temperature
- V_A is the early voltage

The device current gain β is given by ratio of collector current to base current and equals

$$\beta = \frac{J_C}{J_B} = \frac{\int_0^{X_E} \frac{N_E(x)dx}{D_{pE}(x){n_{iE}}^2(x)}}{\int_0^{W_B} \frac{N_B(x)dx}{D_{nB}(x){n_{iB}}^2(x)}} \tag{2.26}$$

where:

- $N_E(x)$ and $N_B(x)$ are the location dependent doping profiles for the emitter and base, respectively,
- D_{pE} and D_{nB} are the diffusion constants of the holes and electrons for the emitter and base, respectively,
- ${n_{iE}}^2$ and ${n_{iB}}^2$ are the intrinsic concentrations of in the emitter and base, respectively.

The value of β at DC is about 600-800 for a high speed SiGe process in the active region. The small signal equivalent circuit for a HBT (SiGe or III-V) is shown in Figure. 2.15, where the dashed box shows the intrinsic device. The cut-off frequency is

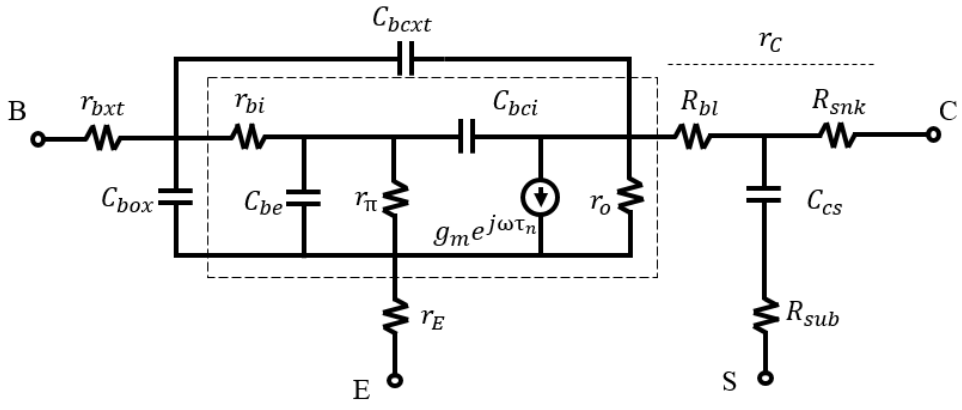

Figure 2.15. Small signal model of HBT.

$$f_t = \frac{g_m}{2\pi(C_{be} + C_{bc})} \tag{2.27}$$

Equation (2.27) gives an approximate value for the cut-off frequency. If the contact resistances are considered in calculations, the cut-off frequency will be

$$f_t = \frac{g_m}{2\pi[(C_{be} + C_{bc}) + g_m C_{bc}(r_E + r_C)]} \tag{2.28}$$

Chapter 3

Low Noise Amplifier Design

Low noise amplifier design is one of the most important aspects of radio astronomy receiver development and it largely determines the noise figure of the system, which has to be as low as possible since incoming radio signals from astronomical sources are extremely weak. Although noise is the main concern in LNA design for radio astronomy applications, other amplifier parameters such as gain, stability, matching and linearity play a critical role as well, and there are tradeoffs between these requirements.

Noise caused by the subsequent stages in the receiver chain also contributes to the overall system noise figure as shown by Equation (3.1).

$$NF_{total} = NF_1 + \frac{NF_2 - 1}{G_1} + \frac{NF_3 - 1}{G_1 G_2} + \cdots \tag{3.1}$$

The noise figure of the first stage directly contributes to the total noise while the noise of the following stage is divided by the gain of the previous stage. This is why the effort in

designing LNAs is focused on lowering the noise figure and increasing the gain of the amplifier. If the gain for the first block is not sufficient, the noise of the next component in the receiver chain, which is a mixer, will have a major effect on the overall noise performance, considering the fact that mixers have high noise figure.

In conventional wireless communication systems, the linearity of the LNA is of great concern to IC designers due to the presence of powerful interferers in adjacent channels. In the specific case of radio astronomy receivers, this issue is of less concern due to the weakness of incoming signals and the absence (hopefully!) of any significant transmitters in the operational bandwidth.

Low power consumption of the LNA is also of interest since a radio astronomy receiver operates for extended periods of time in long astronomical surveys. Excessive power dissipation could cause several problems. The energy dissipates in form of heat by increasing temperature which increases the noise of the amplifier. Radio receiver cartridges are usually cooled down to cryogenic temperatures, and a constant source of heat inside the cartridge has implications for the cooling system design.

Stability is one of the main concerns in LNA design. The amplifier has to be stable at all frequencies and for any values of loading from short circuit to open circuit. Unconditional stability prevents the amplifier from oscillation in and out of the bandwidth. Otherwise it is possible that the amplifier picks up a signal at its input which is not in the operating bandwidth and starts to resonate. This also results in gain degradation and increase of noise in the bandwidth of interest. Using resistive components to introduce some loss to the system is a common technique to stabilize an amplifier at the expense of degrading the noise performance.

Observing time on radio telescopes is limited and expensive, hence narrow-bandwidth and/or high noise receivers are very inefficient and limit the science outcome. A radio receiver is able to cover a wider portion of the spectrum if it has a wide bandwidth RF amplifier (LNA), mixer and IF amplifier. Therefore, there is always a great desire for lower noise and wider-band LNAs in the radio astronomy regime.

The input reflection coefficient of the LNA is an important criterion that often is sacrificed by the designers to achieve lower noise performance due to the inherent tradeoff between matching the input impedance for optimum noise and available power gain. Although the noise figure is not directly affected by high input reflection, designing a low noise amplifier with poor input return loss is a major drawback. The mismatch between the LNA and the feed reduces the power transfer from the feed into the LNA. This is the weak yet very valuable signal that has been picked up from the sky. The mismatch also creates a standing wave with a ripple equal to:

$$Gain\ Ripple = 20\ log\left(\frac{1 + S_{22,Feed}.S_{11,LNA}}{1 - S_{22,Feed}.S_{11,LNA}}\right) \tag{3.2}$$

S_{11} and S_{22} are in linear scales. This amounts to a 0.53 dB ripple in the gain when an LNA with -5 dB reflection coefficient (S_{11}) is connected to a feed with -10 dB output reflection coefficient. It increases to 0.81 dB when the LNA has a poor S_{11} of -3 dB. The gain ripple results in digitization error and overall system noise.

As discussed in Chapter 1, some receivers utilize isolators to mitigate the mismatch problem between the components; however, that comes at the cost of higher component counts, larger cryostat and excessive noise. Also, wideband cryogenic isolators are challenging to design because they introduce difficulty for next generation radio telescopes that expect to have an instantaneous bandwidth as wide as 16 GHz.

Another drawback of a poor input match is the reflection of the power back to the antenna and coupling to the adjacent antennas in an array. The inter-element coupling between the antennas reduces the array efficiency and increases overall system noise.

Figure 3.1 shows the diagram of a low noise amplifier. In most of the devices and processes, the optimum input impedance for the best noise performance is different from the conjugate of the input impedance. This is an important challenge for conventional microwave amplifier design and it becomes even more serious when the LNA has to operate over a wide bandwidth.

The frequency bands for radio astronomy are defined in the 1 MHz to 1 THz range where the band definitions below, about, 10 GHz have larger bandwidths, as high as 2:1, and

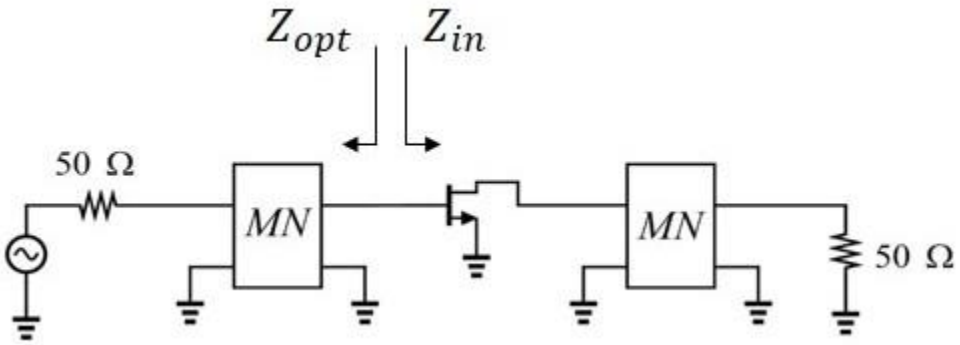

Figure 3.1. Optimum impedance for noise performance and input impedance (MN: matching network).

require broadband LNAs. On the other hand, at frequencies above 10 GHz up to 110 GHz where waveguide feed horns and waveguide interconnections are used, LNAs have a bandwidth of 1.5:1 to match the waveguide band definition. In a recent research by NRC HAA, an octave band (2:1) receiver is proposed based on octave band waveguides components and LNAs to improve the radio telescope performance for future radio telescopes such as ngVLA [94] [95].

In SIS based receivers, the RF bandwidths are still defined with standard waveguide components, and the LNA covers the IF bandwidth which can be larger than 2:1 (usually 4-12 GHz) and 4-20 GHz in recent radio telescope instrument upgrade cycles [96].

However, for achieving acceptable noise performance, input/output matching and gain flatness over wide bandwidths is challenging.

Cooling LNAs is a common method in astronomy to improve the system noise. Decreasing the temperature improves a semiconductor device's performance by increasing electron mobility and reducing thermal noise. The best performance for LNAs can be achieved in the 10-20 K cryogenic temperature range which is warmer compared with that of SIS mixers that need to be cooled down to below 4 K for proper operation. This further decrease in temperature introduces extra cost and complexity to the system. Therefore, in a comparable noise performance, a receiver with LNA is cheaper to operate compared to one with an SIS mixer. Moreover, as described by Equation (3.1), the noise of the next stage is divided by the gain of the previous stage which is 20-30 dB for an LNA and -3 dB to 0 dB for an SIS mixer. This is one of the reasons for changing the paradigm in W-Band receivers

where SIS mixers with comparable noise are being replaced with LNAs in the next generation of radio telescopes. The ALMA Band 2+3 receiver is an example of this change in mm-wave instrumentation [97].

At the transistor level, the transconductance improves by a factor of 1-2 while cooled down to cryogenic temperature and at the LNA level, the improvement in noise temperature is a factor of 7-10 (depending on the quality of cooling) with a gain increase of 2-4 dB.

When it comes to the technology of choice, InP has been offering the best noise performance. The noise can be further improved by employing devices with shorter gate length that have higher cut-off frequency. This trend continues to a gate length of 35 nm where the noise is dominated by the drain resistance and its equivalent noise temperature [98].

In the first part of this chapter, the method of low noise amplifier design is described for a generic FET device that is biased as an ideal two port network with known S-parameters which is applicable to GaAs pHEMT, InP HEMT and GaAs mHEMT technologies. The systematic mathematical and graphical design procedure is developed with the help of computer aided design (CAD) based on the S-parameters of the device. In the remaining parts, we present three MMIC LNAs based on GaAs pHEMT, InP HEMT and GaAs mHEMT technologies at UHF (300 MHz-1.5 GHz), Ka (18-36 GHz) and Q (30-55 GHz) bands, respectively. The specifications for these designs have been driven by the requirements of two future radio telescope instruments: ngVLA and CHORD.

3.1 LNA Design Theory

An amplifier can be designed based on the transistor's S-parameters and given requirements. In a nutshell, designing an amplifier is the task of finding the best source and load reflection coefficients (impedances) and matching the standard 50 Ω input and output ports to these reflection coefficients. In the specific case of a low noise amplifier, the source matching and noise matching are done simultaneously for low noise performance.

Despite having a relatively simple concept as a *randomly varying signal*, quantifying, modeling and measuring the noise in the electrical and electronic circuits is rather a

complicated process. The noise in an electrical circuit may be caused by different phenomena. The most important types of noise are:

1. thermal (Nyquist or Johnson) noise that is caused by random motion of electrons in lossy components,
2. shot noise from random motion of charged carriers in *pn* junctions,
3. flicker noise or 1/f noise in active devices.

In low noise amplifier design, the main focus is to minimize the thermal noise of the circuit, and the most widely used method of representation is the noise in linear two-port networks where the noisy network is modeled as a noiseless network with voltage **and** current noise sources referred to the input of the network as shown in Figure 3.2 (a). And for doing so, the device noise parameters are used as described in the [99]: the voltage and current noise sources represent all of the noises caused by the internal component of the network where the equivalent noise resistance (R_n) and equivalent noise conductance (g_n) are defined as:

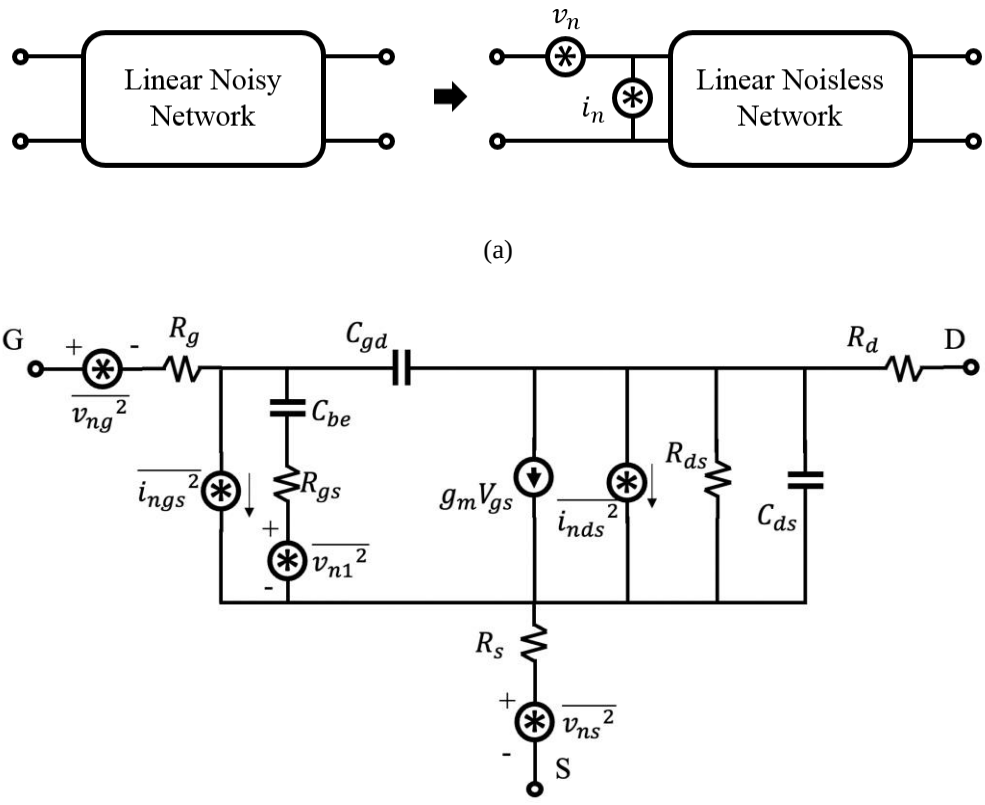

Figure 3.2. Representation of (a) noisy two port network, (b) noise-equivalent circuit of a FET.

$$R_n = \frac{\overline{|v_n|^2}}{4kT_0\Delta f} \tag{3.3}$$

$$G_n = \frac{\overline{|\imath_n|^2}}{4kT_0\Delta f} \tag{3.4}$$

where T_0 is the standard room temperature at which the noise is defined and is equal to 290 K, and k is the Boltzmann constant. As to random processes in a system, in general, the voltage and current noise sources can be correlated, and the correlation factor can be defined as:

$$\rho = \frac{\overline{|v_n \imath_n|}}{\sqrt{\overline{|v_n|^2}.\overline{|\imath_n|^2}}} \tag{3.5}$$

These values explain the noise of the circuit well; however, employing them in high frequency circuit design methodology, where waves and reflections coefficients (S-parameter) are used, results in complex mathematical equations. Instead, they are used to define noise parameters that can be easily used in the design process. The noise parameters of a network are [99]:

1. **Equivalent noise resistance** R_n as defined by Equation (3.3).
2. **Optimum noise impedance** $Z_{opt} = R_{opt} + jX_{opt}$ where

$$X_{opt} = \frac{imag\left(\rho\sqrt{R_n G_n}\right)}{g_n} \tag{3.6}$$

$$R_{opt} = \sqrt{\frac{R_n}{G_n} - {X_{opt}}^2} \tag{3.7}$$

   The optimum noise admittance, $Y_{opt} = G_{opt} + jB_{opt}$, and optimum noise reflection coefficient, Γ_{opt}, can be derived from the optimum noise impedance as:

$$Y_{opt} = \frac{1}{Z_{opt}} \tag{3.8}$$

$$\Gamma_{opt} = \frac{Z_{opt} - Z_0}{Z_{opt} + Z_0} \tag{3.9}$$

3. **Minimum noise temperature** T_{min}

$$T_{min} = 2T_0\left(N + real\left\{\rho\sqrt{R_n G_n}\right\}\right) \tag{3.10}$$

where

$$N = R_{opt}G_n = G_{opt}R_n \tag{3.11}$$

where the minimum noise factor, F_{min}, can be derived as

$$F_{min} = \frac{T_{min}}{T_0} + 1 \tag{3.12}$$

Finally, the noise of a two port network connected to an arbitrary source can be calculated as

$$T_n = T_{min} + 4NT_0 \frac{\left|Z_S - Z_{opt}\right|^2}{R_{opt}R_s} \tag{3.13}$$

where $Z_S = R_s + jX_s$ is the complex source impedance. The noise can be also represented as

$$T_n = T_{min} + NT_0 \frac{\left|\Gamma_S - \Gamma_{opt}\right|^2}{(1 - |\Gamma_s|^2)\left(1 - \left|\Gamma_{opt}\right|^2\right)^*} \tag{3.14}$$

Note that R_n and G_n are the representation of the physical phenomena that cause noise in a device while F_{min} and Γ_{opt} depend on the electrical model of the device (resistances, capacitances, inductances and dependent current source) and how individual components interact resulting in a minimum "achievable" noise figure. The optimum impedance is a source impedance at which the noise is minimized. Once physical noise sources and the small signal model of the transistor are known, all four parameters mentioned above can be calculated.

Figure 3.2 (b) shows the noise model of a FET where different components contribute to the overall device noise. This complex network can be simplified and represented by its equivalent model of Figure 3.2 (a) with four noise parameters calculated for each given frequency.

Once the noise parameters of the network (device) are specified, designing the matching network starts. However, the mathematical aspect of the issue is quite complex and has been covered in detail in microwave amplifier books [100]. Also, a detailed design

methodology including the geometrical methods (source, load and gain circles) for MMIC LNA has been presented in [101]. Alternatively, in a more minimalistic approach that has been traditionally adopted by RFIC designers, first the device is biased at the "known to be low noise" bias point (this information is provided by the device vendor or the semiconductor foundry or from measurements). Then its small signal model is used to design the matching networks at the input and output. As a matter of fact, this methodology provides a very good initial design at frequencies as high as 100 GHz. Once the lumped element values are defined, they can be optimized and finally changed to distributed components for higher frequency designs. It is important to point out that in this method, the device itself can be sized to make the real part of the optimum noise impedance equal to the source impedance (50 Ω) to avoid the gain-noise tradeoff as much as possible. This is easily applicable in Si-based technologies where designers have more control over the geometry of the device. On the other hand, III-V designs are more limited when it comes to transistor layout; therefore, some microwave low noise amplifier design methods can be useful.

In the method employed in this research, the low noise amplifier design starts with biasing the transistor at a current density that provides the lowest minimum noise and continues with designing a reactive matching network for the desired frequency with the following priorities in order for **radio astronomy** applications:

1. minimizing noise,
2. maximizing the gain,
3. minimizing input return loss,
4. minimizing output reflection,
5. minimizing DC power,
6. maximizing linearity.

In practice the minimum noise of a FET is achieved at an optimum current density that is constant at different frequencies as shown in Figure 3.3. This optimum bias current density is called J_{opt}. J_{opt} is independent of the size of the transistor and is about 150-250 mA/mm,

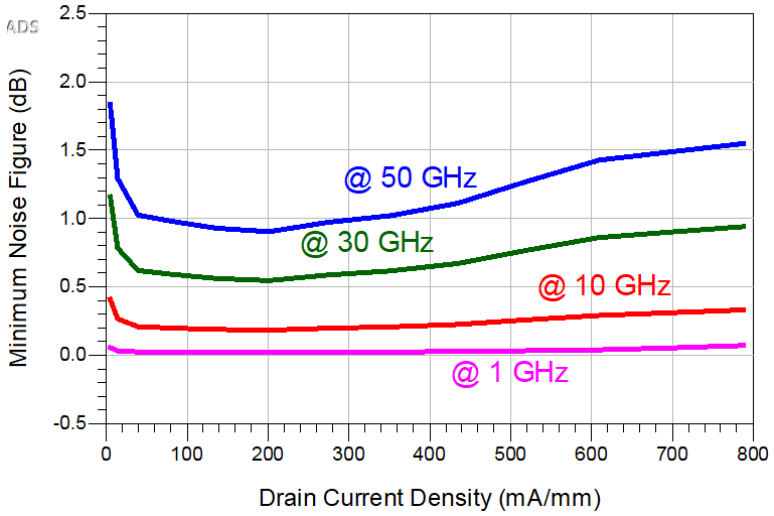

Figure 3.3. Optimum noise current density for a generic HEMT device (GaAs and InP).

depending on technology. In HBTs this value changes for different frequencies (increases with frequency).

The transistor size can be defined so that $real\{Z_{opt}\}$ = 50 Ω. If the real part of the optimum impedance cannot be designed to be 50 Ω, it results in a noise that is higher than NF_{min} (equivalent to "noise circle" concept in microwave amplifier design methodology).

Next, the real part of the input impedance is set to 50 Ω by using a source degeneration. The input impedance for the common source amplifier with a source degeneration as shown in Figure 3.4 (a) can be found from

$$Z_{in} = sL_s + \frac{1}{sC_{gs}} + \left(\frac{g_m L_s}{C_{gs}}\right) + R_g \tag{3.15}$$

Note that C_{gd} is neglected for simplicity. This is a valid at low frequencies. At higher frequencies the effect of C_{gd} is not negligible and results in an input impedance that is depends on the load of the transistor. Despite a low frequency estimate, Equation (3.15) provides a good initial point for the design. It shows that inductive degeneration translates into a real part of the input impedance by a factor of g_m/C_{gs} which, roughly, equals f_t. We can choose the L_s to have a real part of 50 Ω.

$$real\{Z_{in}\} = \frac{g_m L_s}{C_{gs}} + R_g \equiv 50\ \Omega \tag{3.16}$$

Next, the capacitive part of the input impedance is naturalized with a series inductance as shown in Figure 3.4 (b) where

$$Z_{in} = s\left(L_s + L_g\right) + \frac{1}{sC_{gs}} + \left(\frac{g_m L_s}{C_{gs}}\right) + R_g \tag{3.17}$$

At the frequency of interest, we design L_g such that

$$imag\{Z_{in}\} = j\omega\left(L_s + L_g\right) + \frac{1}{j\omega C_{gs}} = 0 \tag{3.18}$$

$$\frac{-\omega^2\left(L_s + L_g\right)C_{gs} + 1}{j\omega C_{gs}} = 0 \tag{3.19}$$

$$\frac{1}{\omega^2} = \left(L_s + L_g\right)C_{gs} \tag{3.20}$$

$$L_g = \frac{1}{\omega^2 C_{gs}} - L_s \tag{3.21}$$

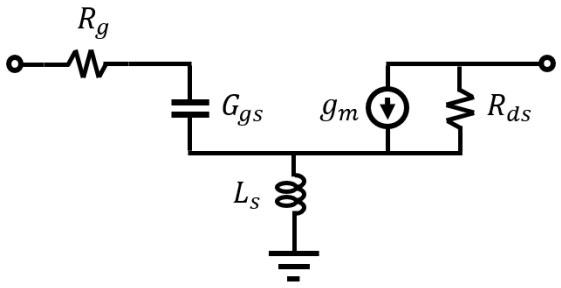

(a)

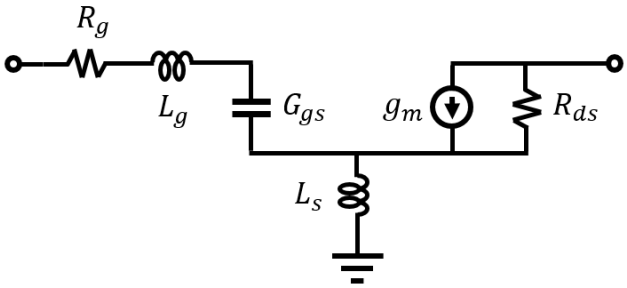

(b)

Figure 3.4. Transistor small signal input with (a) inductive degeneration and (b) gate inductor.

The output matching can be designed using an inductor to allow for maximum swing and minimizing the noise.

Once the RF matching networks are designed, the bias circuitry can be added. There are various topologies to bias a transistor in operation and each has its own advantages and disadvantages. These methods are different in terms of number of required DC supplies, dissipation power, noise, stability and output power. Figure 3.5 shows a few biasing networks. Network (a) is a desirable option when the supply is single polarity and the area is limited for adding biasing lines since only one biasing line is brought to the drain of the transistor, and the gate is self-biased. The noise performance is not the best due to the presence of the resistor in the source. To ground the resistor's noise, the source capacitor has to be quite large but the area on the chip is limited, and if the capacitor is not large enough, it causes the noise to enter the device and degrade the amplifier's performance. Moreover, a considerable amount of power is dissipated in the source resistor which creates

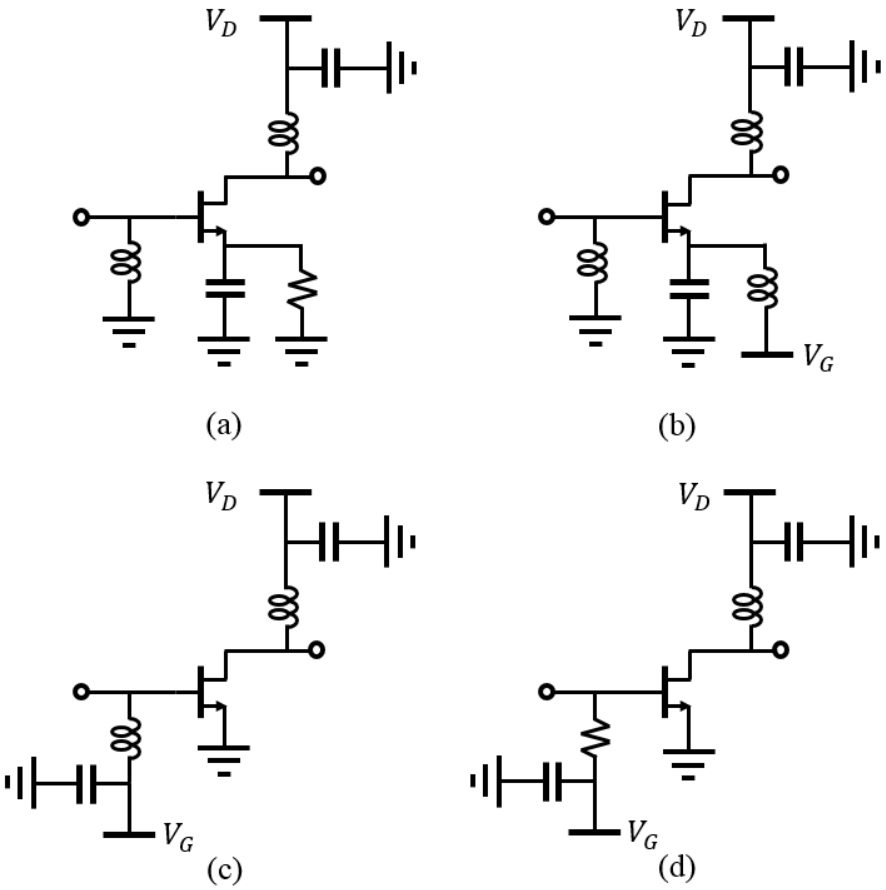

Figure 3.5. Biasing networks.

heat and more noise. Network (b) is the proper choice when the supply is single polarity and there is enough area to use two sets of biasing lines. The source capacitor might be problematic when the circuit operates at low frequencies since it must be quite large to pass the AC signal. Network (c) is the best choice regarding noise, efficiency and power at the cost of requiring two polarities of biasing supply. RF decoupling capacitors can be off-chip which means that the DC pads and wire bonds (or DC probes) are involved in the amplifier's frequency response. It is not possible to fabricate the DC decouplers on-chip because they will become too large and cannot fit on the designated area. Network (d) is very similar to (c) with the exception of using a large resistor instead of the inductor at the gate of the transistor. This is useful especially in designing a stage other than the first stage where the signal sensitivity to noise has reduced due to at least one stage of amplification. The resistor also helps the overall LNA stability.

3.2 UHF-Band GaAs pHEMT LNA

3.2.1 Telescope's Requirement

Radio telescopes that operate at sub-gigahertz frequencies are critical for observation of astronomical phenomena such as detecting fast radio bursts (FRBs), the study of magnetic radiations of the sun, and mapping the hydrogen intensity (HI) by using 21-cm emissions. All these science missions require instruments in the cm-wavelengths range. This is equivalent to the MHz and low GHz regime.

The Canadian Hydrogen Intensity Mapping Experiment (CHIME) is a transient radio telescope made of a 512 dual-polarization array that surveys the sky across the 400-800 MHz band. CHMIE's successor, the Canadian Hydrogen Observatory and Radio-transient Detector (CHORD), which is proposed for near future construction, is an ultra-wideband instrument covering frequencies as low as 300 MHz up to 1.5 GHz with outrigger stations in 1500 and 3000 km distances [102].

512 high-precision 6-m composite dishes are located in the Dominion Radio Telescope Observatory (DRAO) in Penticton, British Columbia and two CHIME-like 64-dish array

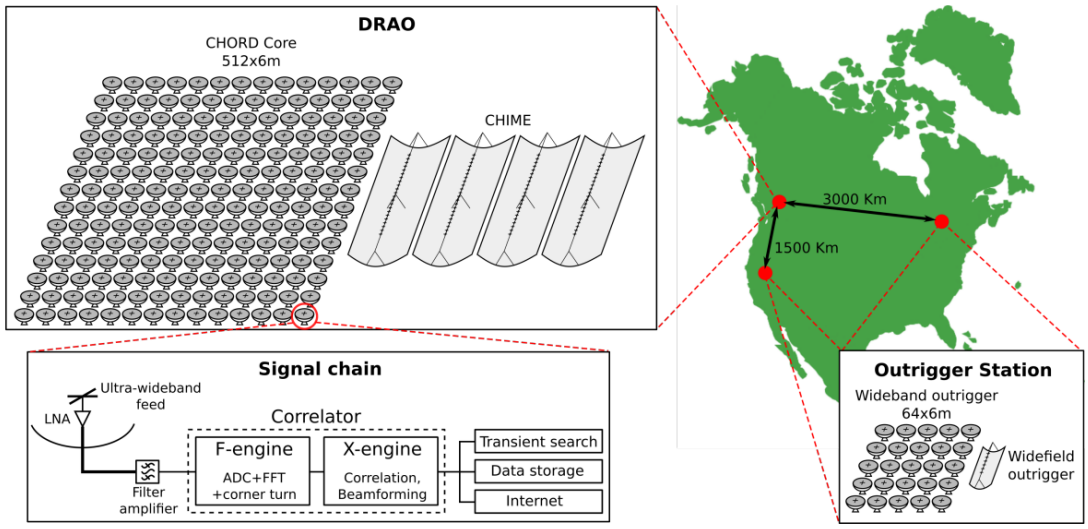

Figure 3.6. CHORD telescope overview. Taken directly form [102].

outrigger stations in 1500 and 3000 km distances to create a large collecting area. The array expands thousands of kilometers and in remote locations [102].

Despite conventional radio telescopes, CHORD will not employ a cryogenic-cooled frontend. To reduce the price and complexity of the system and the ability to operate in remote locations with minimum maintenance, the frontend including LNAs operates at room temperature.

As described in the technology roadmap of CHIME, the receivers utilize high precision composite dishes and ultra-wideband dual polarized feeds. The low noise amplifiers are required in large numbers that provide 5:1 bandwidth with high gain (30 dB) and low noise figure, below 0.8 dB.

3.2.2 Design

The main challenge in designing a wideband LNA in the UHF band is to achieve optimum noise matching over the 5:1 bandwidth ratio as well as matching the input impedance to a standard 50 Ω interface. The authors of [103] had to trade off input matching as high as -5 dB to achieve low noise performance. This is due to the fact that the transistor input impedance is very high, like an open circuit, at low frequencies, but the impedance significantly decreases at 1.5 GHz.

To overcome the high impedance issue, we can use the large number of transistor fingers to increase the gate capacitance. This can also help to reduce the device gate resistance leading to reduction of noise resistance, R_n. Also, it decreases the device's input/output impedances and relaxes the requirement of large value components for matching networks. Although we aggressively increased the transistor size to 22×40 μm^2 to reduce the input

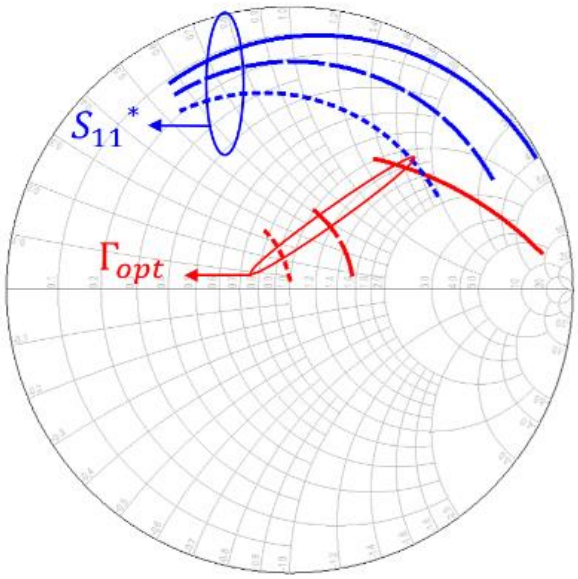

Figure 3.7. Optimum noise impedance (red) and conjugate of S_{11} (blue) without feedback (solid line), with 5 kΩ and 2 pF RF feedback (dashed line), and with 2 kΩ and 2 pF RF feedback (dotted line).

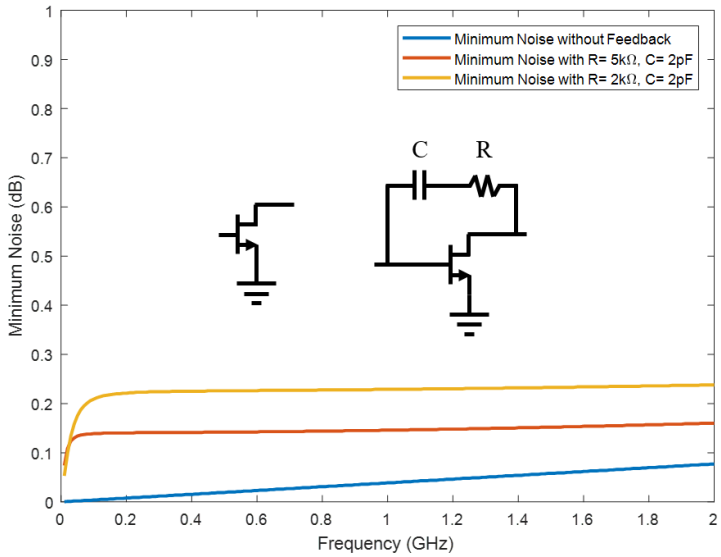

Figure 3.8. Minimum noise figure before and after adding RF feedback network.

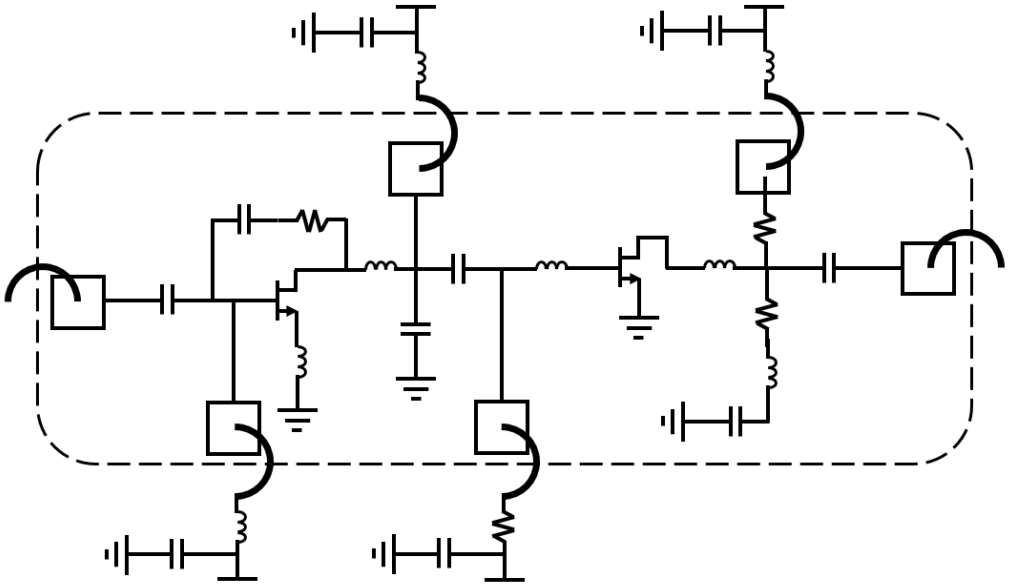

Figure 3.9. LNA schematic design.

impedance, it is still not enough to realize an acceptable input return loss. An RC feedback network can be used at the first stage to achieve the desired input impedance matching.

Figure 3.7 shows the input impedance change before and after the RC feedback network is added in. As can be seen, the optimum noise impedance Γ_{opt} and transistor S_{11} move closer to the 50 Ohm centre point on the Smith Chart. Figure 3.8 shows the minimum noise increasing due to thermal noise injected by the feedback resistor. The amount of feedback can be tuned for optimum noise and bandwidth performance.

Figure 3.9 shows the schematic of the LNA where adding the RC feedback network changes the input impedance closer to 50 Ω without the need for any input matching component except for the large DC decoupling capacitor. The first stage includes a large number of transistor fingers while the second one utilizes a smaller size transistor. Transistors are biased at 2 V drain voltage, and off-chip 50 nH RF chokes are used as well as 1 nF RF decoupling capacitors. The gate voltages are set at -0.95 V. The first stage uses an off-chip 50 nH inductor, and the second gate is biased via a 50 kΩ resistor for stability purposes. The inductances of the wire bonds at input/output (30 mil) and bias line bonding wires (60 mil) were included in the circuit design. Although adding the RC network improves noise matching and input impedance matching, the resistor's thermal noise

contributes extra noise to the overall amplifier noise. Decreasing the feedback resistance provides better input matching but results in higher thermal noise at the input of the transistor as well as lower gain for the first stage. Thus, it was optimized to the lowest possible noise with acceptable input reflection of about -10 dB.

3.2.3 Gain Equalizer

The purpose of increasing the size of transistors in the first stages is to lower the transistor input impedance for better wideband noise matching and input return loss. However, such a large device size provides a very high gain at 300 MHz, but the gain rolls off significantly over the 5-decade frequency range. Therefore, in order to have a flat gain, we employ an on-chip gain equalizer circuit Z_e in Figure 3.10 (a) at the output of the second stage of the amplifier to limit the low frequency gain with minimum change at the high end of the frequency band. Figure 3.10 (a) shows the proposed circuit that consists of a series RLC network. The L_e and C_e values are designed to have a resonance frequency at the low end of the band (f_{low}), which results in lowering an equivalent load impedance of ($Z_e = R_e$)||Z_0 as shown in Figure 3.10 (b), and reduces the amplifier gain at the low end of the frequency band. As the frequency increases, the series RLC network impedance shifts towards an open circuit as shown in Figure 3.10 (c), and the amplifier sees a higher equivalent load

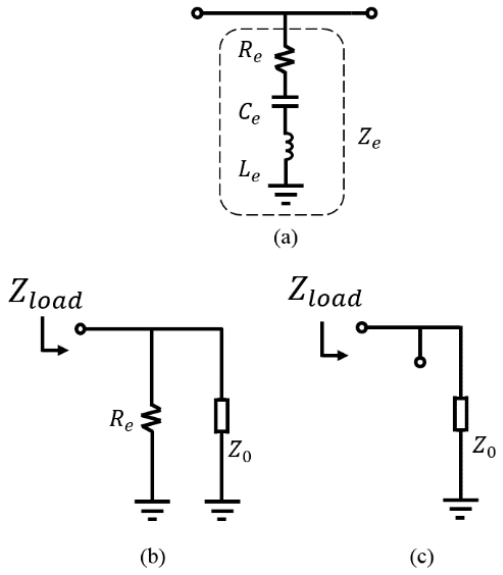

Figure 3.10. Gain equalizer: (a) proposed circuit, (b) equivalent load at low frequencies, (c) equivalent load at high frequencies.

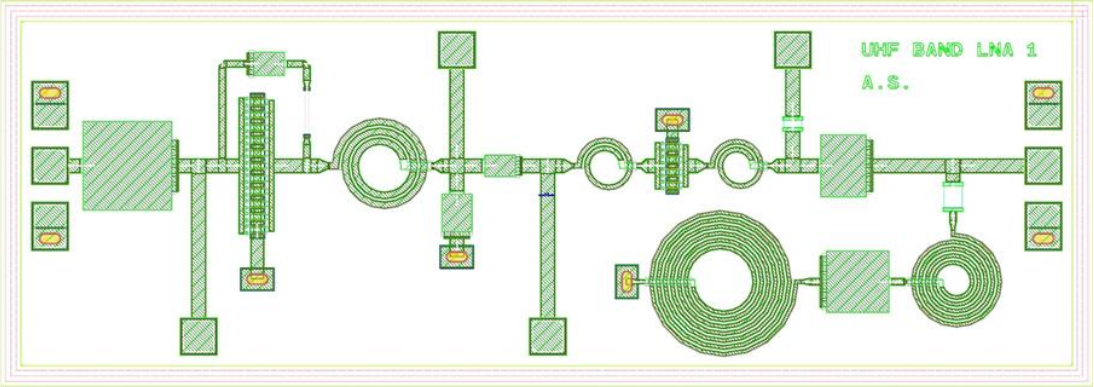

Figure 3.11. Layout of the UHF LNA.

impedance, $(Z_e \rightarrow \text{open}) \| Z_0$ as shown in Figure 3.10 (c) that corresponds to a higher output power gain. This equalizer circuit adds a positive gain slope with respect to increasing frequency. It is worth noting that the value of R_e is optimized for wideband performance and higher gain.

Figure 3.11 shows the final layout of the chip submitted to the WIN foundry, and Figure 3.12 shows the simulation results. The LNA achieves about 30 dB gain, S_{11} and S_{22} of about -10 dB over the band. The noise performance of the LNA is predicted to be 0.3-0.4 dB over the frequency of interest.

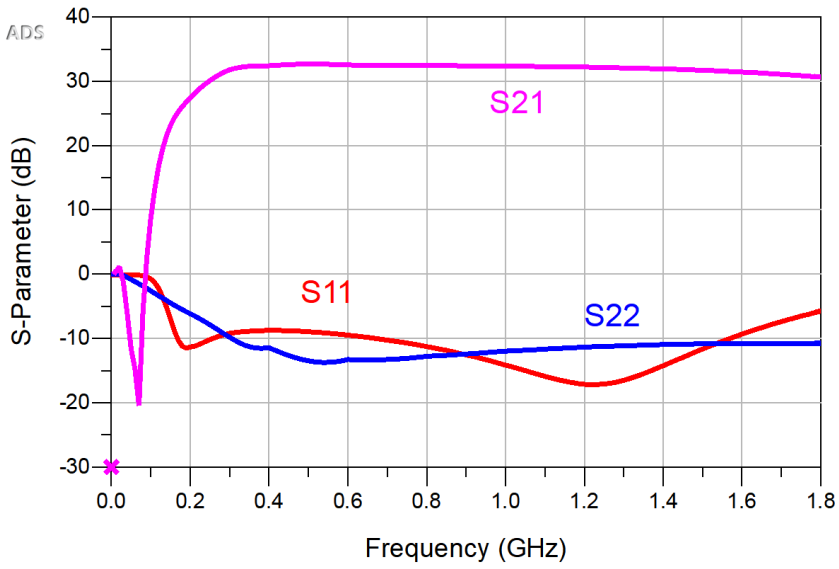

(a)

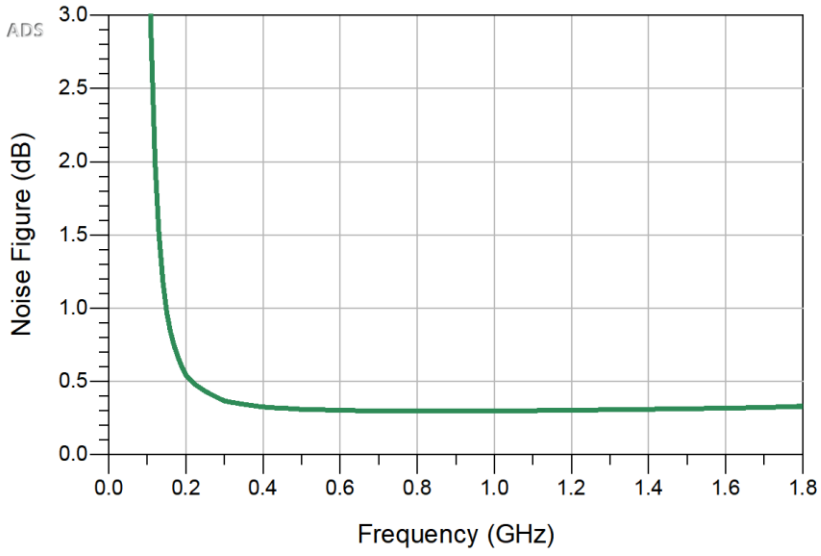

(b)

Figure 3.12. Simulation results of the UHF LNA: (a) S-parameters, (b) noise figure.

3.2.4 Alternative Design

An alternative design is shown in Figure. 3.13 (a) which employs an input matching network. The input of the transistor is matched to 50 Ω using an LC ladder circuit. Since the series inductor is directly located at the input signal path, it has a high quality (Q) factor

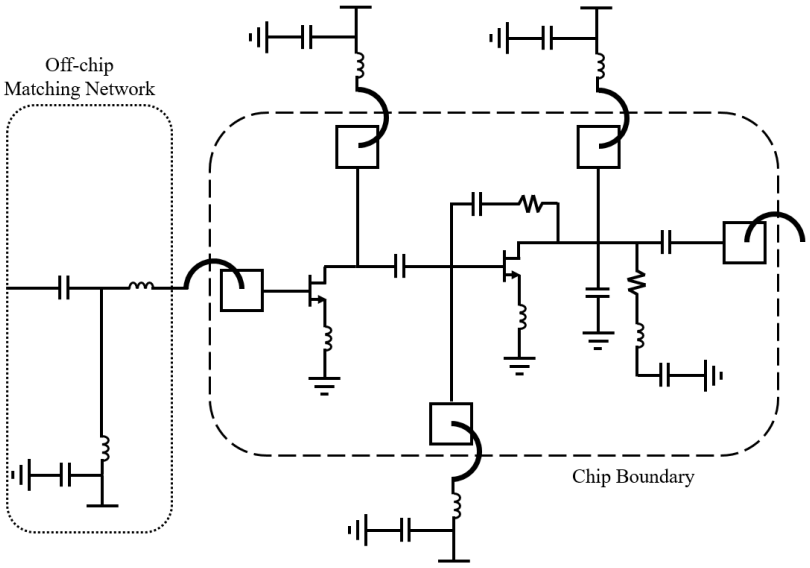

(a)

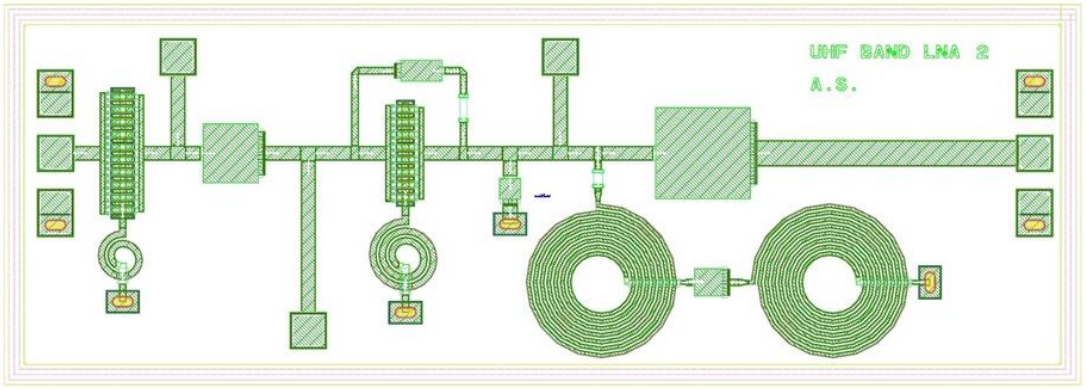

(b)

Figure 3.13. (a) Alternative LNA schematic (b) layout of the alternative UHF LNA design.

of at least 30, to minimize the noise contribution to the LNA's overall noise performance. On the other hand, the highest achievable Q factor for an on-chip inductor for the given technology is about 20. Thus, to minimize the resistive loss, the matching network is realized off-chip using inductors with Q-factor of 35 and 5 GHz self-resonance frequency. An RC feedback is used in the second stage to achieve optimum output matching and consistent gain over a wider bandwidth. Both transistors have a high number of fingers and are biased at 2 V drain voltage and -0.95 V gate voltage with a total drain current of 195 mA, resulting in a power consumption of 390 mW. Off-chip RF chokes are used for bias lines as well as RF decoupling capacitors. The second stage employs an RC feedback for

stability purposes. The inductance of the wire bonds at input/output (30 mil) and bias lines (60 mil) was considered as well. Figure 3.13 (b) shows the layout submitted to the foundry. The simulation results are presented in Figure 3.14, and similar performance compared to that in Fig. 3.11 is predicted.

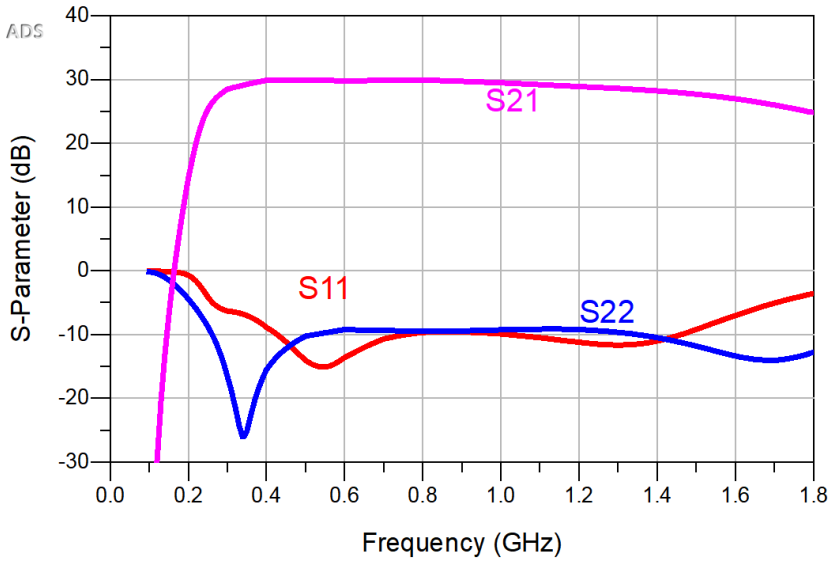

(a)

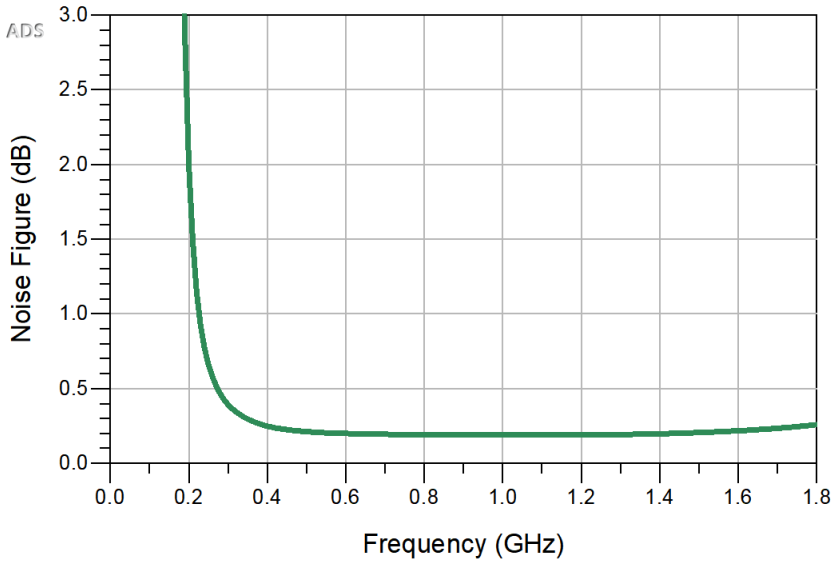

(b)

Figure 3.14. Simulation results of the alternative UHF LNA: (a) S-parameters, (b) noise figure.

3.2.5 Measured Results

Microphotographs of the fabricated MMICs are shown in Figure 3.15. The chips and off-chip components were integrated in a custom designed chassis. The chassis was made of gold plated copper with 3.5 mm coaxial input and output ports. Two different PCBs were fabricated on a RT/Duroid 5880 board with electroless nickel immersion gold (ENIG) finishing to bring the input/output and DC bias to the LNAs and to install the off-chip components. Our experiment showed that 0.4 μm thick gold finish results in some difficulty in wire bonding, and at least 2 μm of gold thickness is required for reliable wedge bonding. Figure 3.16 shows the assembled LNAs. The packaged amplifiers were measured using a Keysight N227B PNA with coaxial calibration to extract the S parameters, and the noise performance was evaluated by an Agilent (Keysight) N8975A Noise Figure Analyzer and an Agilent (Keysight) B400A1 Smart Noise Source. Figure 3.17 shows the measured results of the primary design; the LNA has around 28 dB gain across the band with low

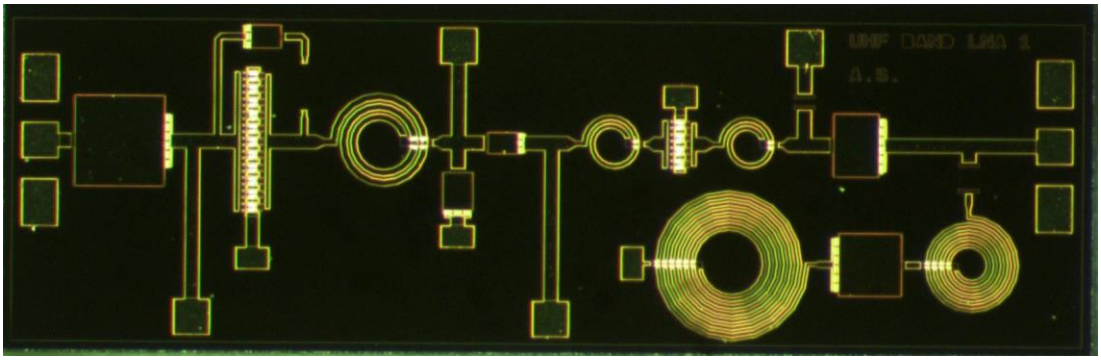

(a)

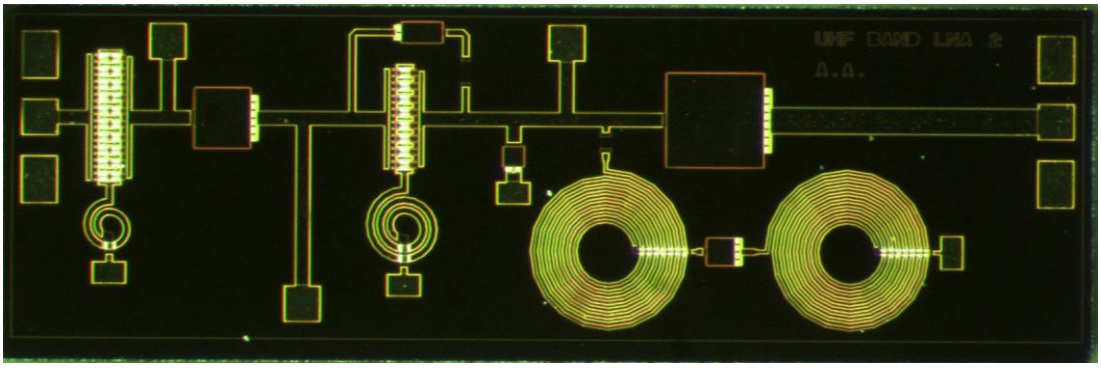

(b)

Figure 3.15. Microphotographs of the fabricated chips: (a) primary design, (b) alternative design.

output reflection. The input reflection shows the same wideband profile as simulation models; however, it is about 2-3 dB higher at the end of the band which is mainly due to the uncertainty associated with the transistor models for large number of fingers. The output reflection is below -15 dB in the band which is lower than expected.

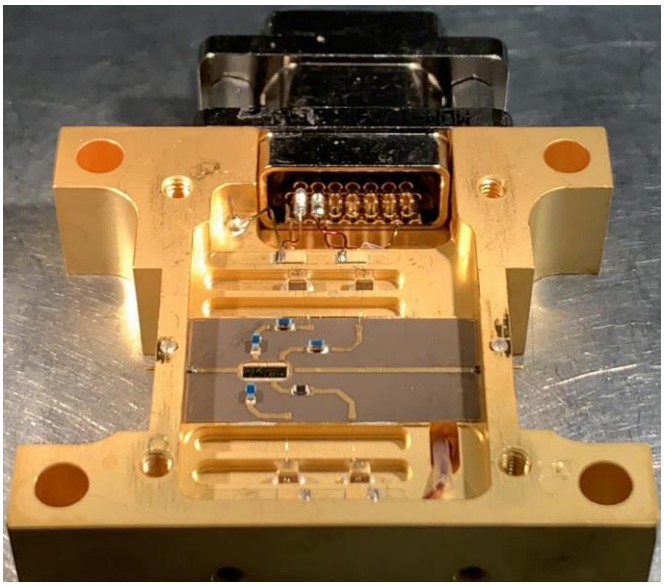

(a)

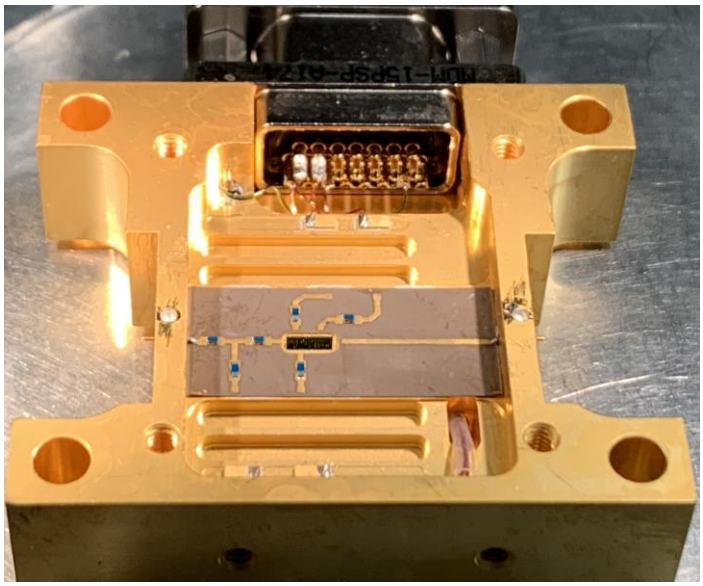

(b)

Figure 3.16. LNA assembly: (a) primary design, (b) alternative design. The large de-coupling capacitors are placed in the chassis' pockets. The off-chip matching network is placed at the input of the chip in the alternative design.

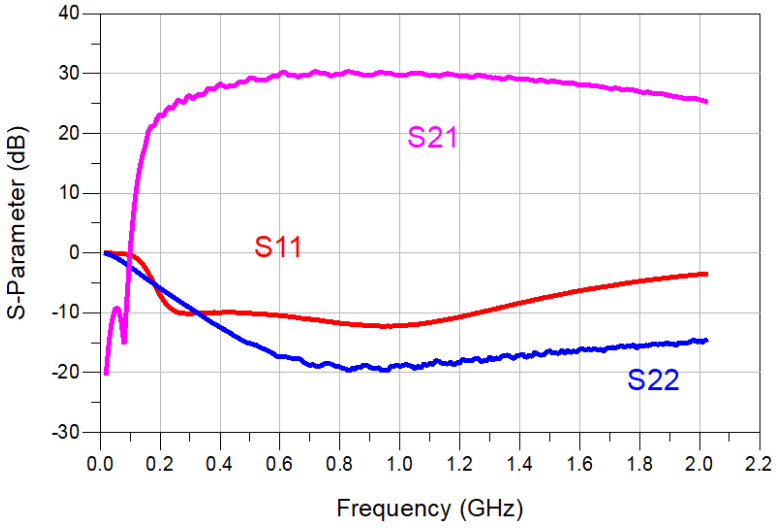

(a)

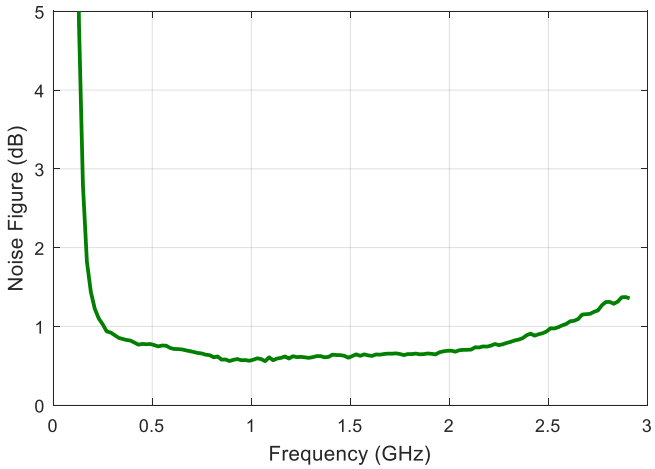

(b)

Figure 3.17. Measurement results of the UHF LNA: (a) S-parameters, (b) noise figure.

The noise figure has a minimum of 0.55 dB at 800 MHz and is about 0.6-0.625 dB over the rest of the band. An increase in noise towards lower frequencies is attributed mainly to impedance mismatch with the optimum noise impedance. The LNA chip was biased at 2.2 V, with total bias current of 160 mA, and consumes 350 mW DC power.

Figure 3.18 shows the measured results of the alternative design where the maximum gain reaches 30 dB at the lower side of the band and reduces toward higher frequencies. The gain roll off of the two transistors is so significant that even after using a feedback and the

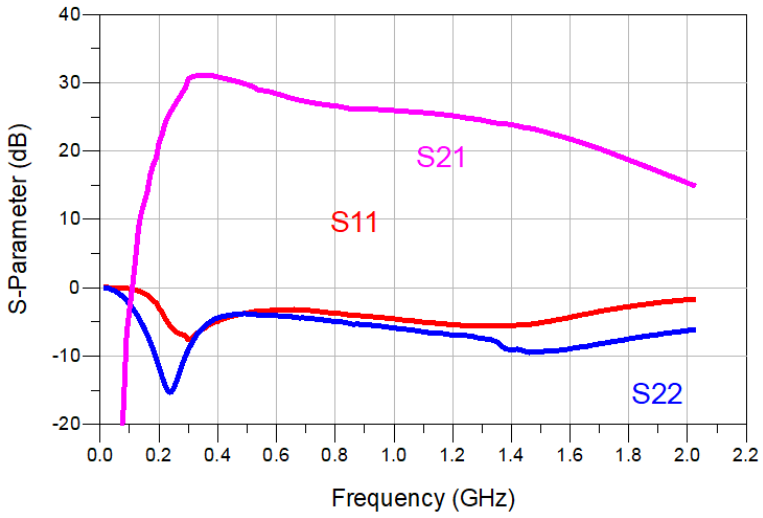

(a)

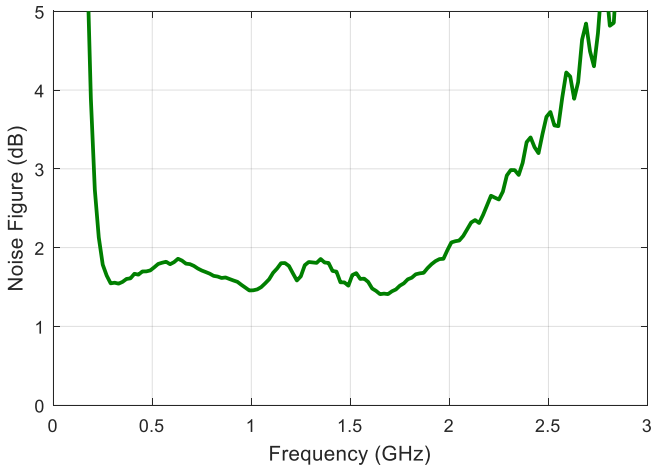

(b)

Figure 3.18. Measurement results of the alternative UHF LNA: (a) S-parameters, (b) noise figure.

gain equalizer, a 5 dB decrease was experienced. The less accurate transistor models for high finger count translates to high input/output reflections compared to the simulation as well as the off chip matching network (DC de-coupling capacitor, series gate inductor and parallel inductor) over which there is a limited control. The measured noise, however, is higher than in simulation and is about 1.8 dB. This is most likely caused by the off-chip components and soldering connections with limited conductivity. Table 3.1 summarizes the LNA results in comparison with other published works in similar frequency bands.

Table 3.1. Summary of published LNA performances.

Reference	Technology	Freq (GHz)	NF (dB)	S_{11} (dB)	Gain (dB)	V_{dd} (V)	P_{DC} (mW)
[103]	HEMT InP MMIC	0.3-14	0.8	-5	40	2	100
[104]	pHEMT GaAs Hybrid MIC	0.4-0.8	0.34	-8	41	1.4	400
[105]	mHEMT GaAs MMIC	0.6-1	0.5	-12	21	6	852
[106]	CMOS RFIC	0.7-1.4	0.35	-10	19	1	45
This work (primary design)	pHEMT GaAs MMIC	0.3-1.5	0.6	-10	28	2.2	350

3.3 Ku-Band InP HEMT LNA

3.3.1 Telescope's Requirement

In order to improve the instrument's efficiency, it is desirable to increase the bandwidth of each band in the radio telescope without sacrificing the performance to reduce the number of required bands to cover the spectrum of interest. Therefore, next generation telescopes take advantage of wideband front-ends with lowest achievable noise. As bridging instrument between cm- and mm-wavelength astronomy, the ngVLA is an array radio telescope composed of 244 reflector antennas with 18-meter diameter located in New Mexico. The telescope is currently in its conceptual design phase and component development process. The front end consists of six frequency bands ranging from 1.2 GHz to 116 GHz where there is an interest in the development of low noise amplifiers for multiple bands.

The ngVLA Band 3 is defined to cover the frequency range 12.3-20.5 GHz which has been used as the driving specification for a wideband LNA amplifier based on NRC's InP process.

3.3.2 Design

The design starts with developing a model for a fabricated transistor to be used for LNA design. The model is the result of two sets of measurements: S-parameter measurement

and noise figure measurement. Ideally, the best way to determine the noise parameters defined by Equations (3.3), (3.6), (3.7) and (3.10), is measuring the noise figure of the device for at least four different complex source impedance values and directly calculating the noise parameters. However, an impedance generator that generates complex impedance over the wide frequency of interest was not available. Therefore, an alternative method was used for this research as described below.

First, S-parameters were measured over the frequency range of 10-50 GHz using an RF-Probe station for at least two different bias points. A low power low noise bias as well as a high gain bias with the gate voltage of about -0.3 V to -0.2 V and drain voltage of about 0.6 V to 0.8 V was used for a few different device sizes. Noise measurements were performed for the same set of bias points and device sizes. Next the measured S-parameter were fitted to the small-signal model shown in Figure 3.2 to extract the values of small-signal components. Knowing the RLC values of the small-signal model in Figure 3.2, the noise sources' values were optimized so that the noise figure of the simulated small-signal model matches the measured noise figure of the device at a given bias point for each device size.

Once all the passive and noise source values are known the noise parameters are calculated using ADS for a given size at a fixed bias point. The models were used for designing low noise amplifiers.

The wideband LNA is to cover a frequency range of 12-24 GHz. It is designed to achieve above 30 dB gain and a noise figure of about 1.1 dB. A 4-stage amplifier is designed using 150 nm InP HEMT devices as shown in Figure 3.19. Low power low noise bias points (equivalent small signal model) were used for the first and second stage while the third and fourth stages utilize high gain bias points.

Figure 3.20 presents the final layout of the chip that is currently being fabricated. Figure 3.21 demonstrates the final EM simulated results. The LNA can achieve more than 35 dB gain and input/output return loss better than 10 dB. The room temperature noise figure is 1.1 dB at 17 GHz and is lower than 1.4 dB for the entire bandwidth of operation.

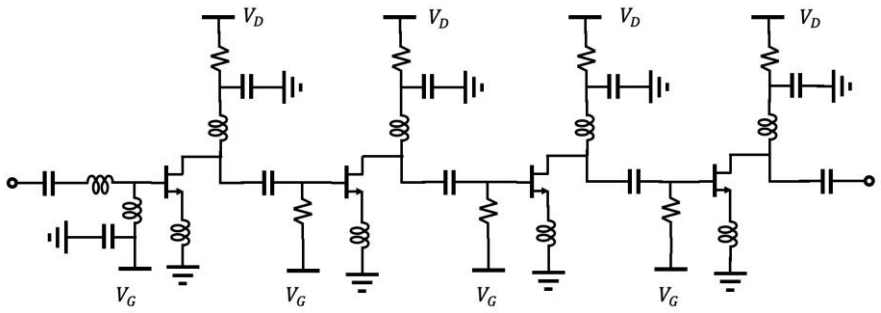

Figure 3.19. Schematic design of the Ku-band LNA.

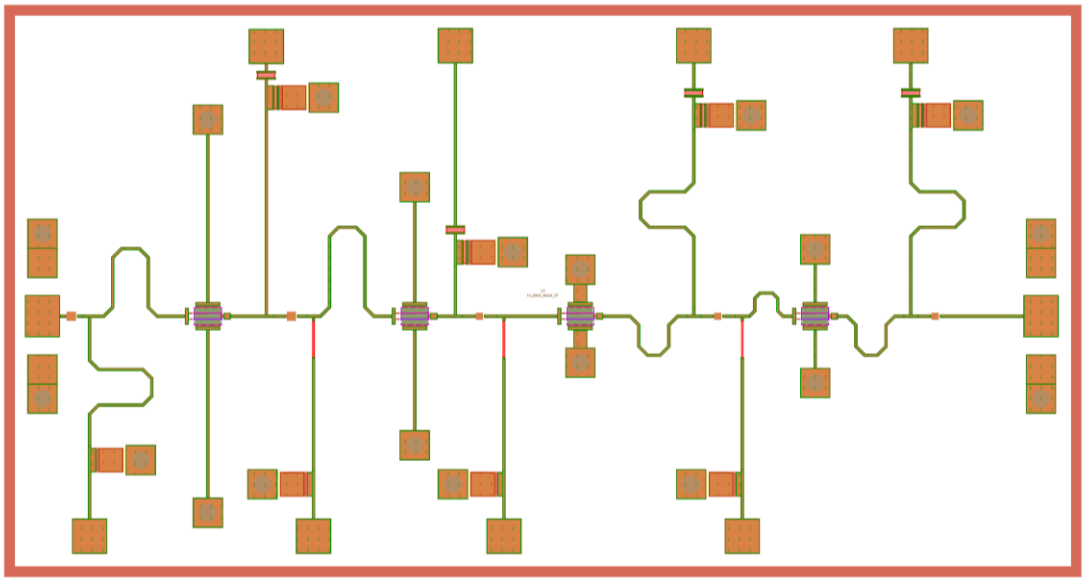

Figure 3.20. Layout of the Ku-band LNA.

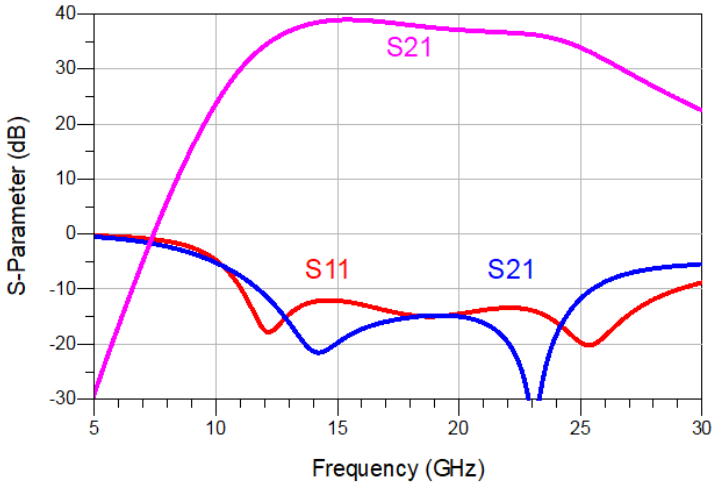

(a)

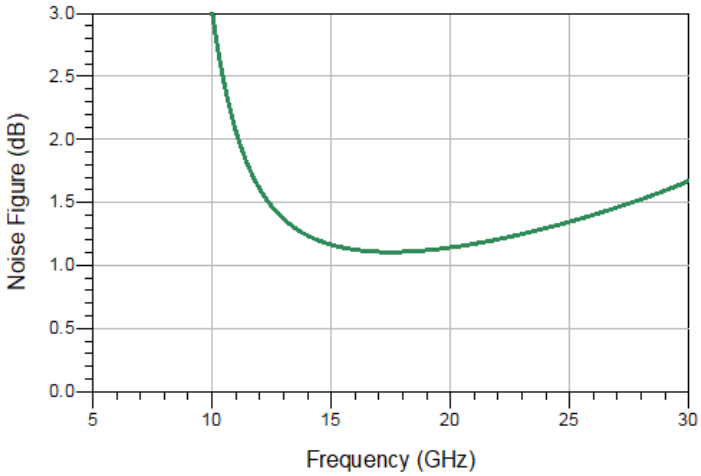

(b)

Figure 3.21. Simulation results of the Ku Band LNA: (a) S-parameters, (b) noise figure.

3.4 Ka-Band InP HEMT LNA

3.4.1 Telescope's Requirement

As described in [94], the ngVLA is interested to expand the band definition especially for Band 4 that is used to study major science cases of high red-shift and cosmology such as:

- study of the CO (1-0) line at the range of 28-38 GHz and galactic star formation at z ~ 2-3,
- study of CO (1-0) and CO (2-1) lines at around 16-28 GHz

Therefore, a wideband Band 4 is preferable for the telescope to cover these combinations. The original ngVLA Band 4 is 20.5-34 GHz that follows the traditional 1.67:1 band derived from waveguide and feed horn operation frequencies. However, it is proposed that this bandwidth is expanded to 18-36 GHz to satisfy the science goals. Therefore, all the frontend components including the LNA should satisfy the wideband performance.

The cryogenic LNA is required to have 7-9 K noise temperature at cryogenic temperature. The required gain is about 30 dB with appropriate (about 10 dB) input and output return loss.

3.4.2 Design

The design starts by developing small-signal and noise models for the frequency of interests as explained in Section 3.4.1. The S-parameters measurements (up to 50 GHz) cover the entire frequency range of interest; however, the noise measurements were performed up to 26 GHz (upper limit of the noise figure analyzer). Therefore, the data was fitted to test results up to 26 GHz and the noise data beyond this frequency are based on simulations.

The design utilizes four stages of amplification based on 150 nm InP HEMT devices in common source configuration. The first and second stage are biased at low power low noise condition while the third and fourth stages are designed at high gain bias.

Figure 3.22 shows the schematic of the octave band LNA. The layout of the chip is shown in Figure 3.23. Figure 3.24 presents the final EM simulation results. At the time of the submission of this thesis, the InP wafers are in the fabrication process. The LNA has about 35 dB gain across the band and input/output return loss better than 12 dB. The lowest noise figure is 1.3 dB at 26 GHz and is lower than 1.4 dB for the entire bandwidth of operation.

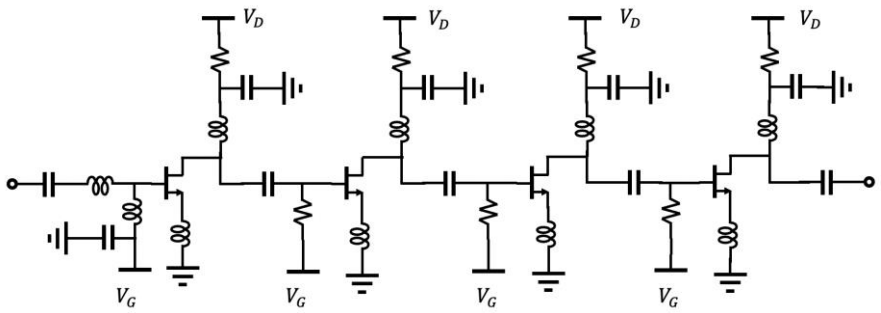

Figure 3.22. Schematic design of the Ka-band LNA.

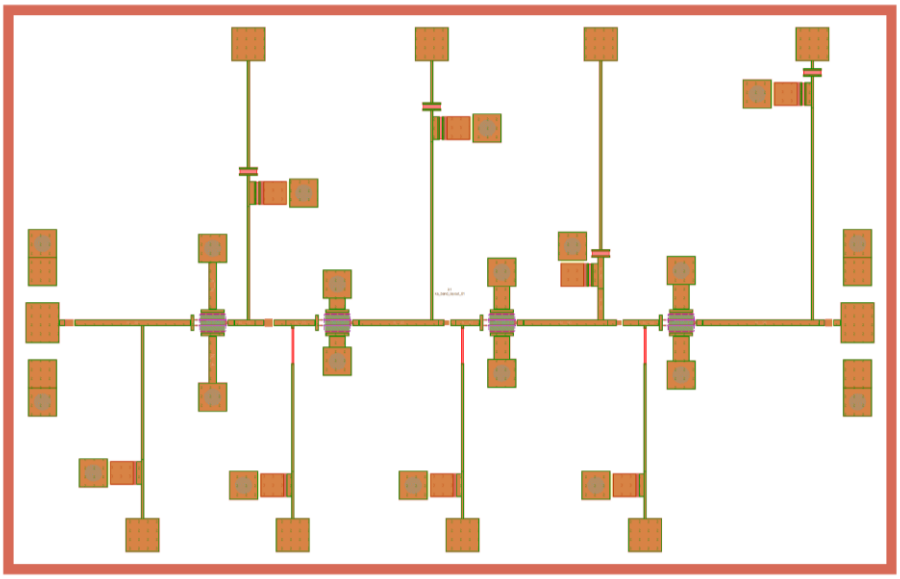

Figure 3.23. Layout of the Ka-band LNA.

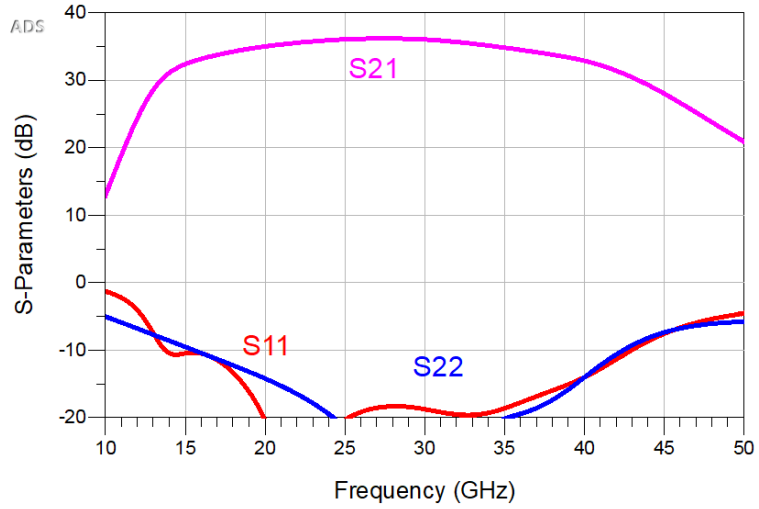

(a)

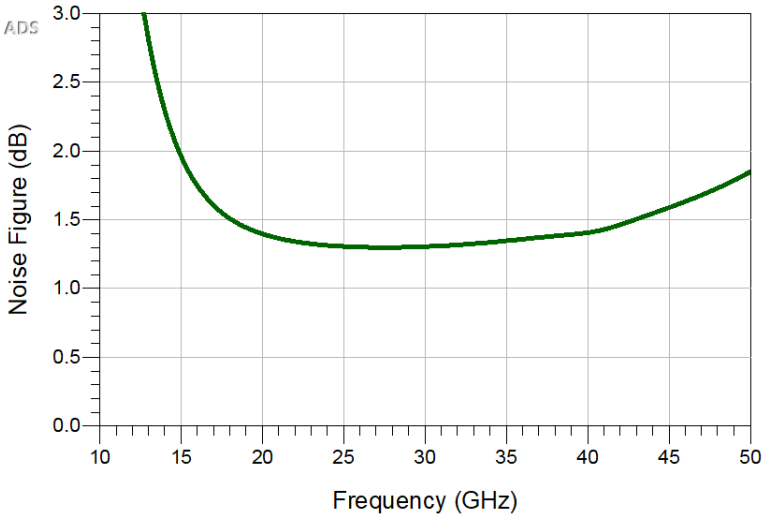

(b)

Figure 3.24. Simulation results of the Ka Band LNA: (a) S-parameters, (b) noise figure.

3.5 Q-Band GaAs mHEMT LNA

3.5.1 Telescope's Requirement

The majority of wideband LNAs presented for cryogenic receivers have been based on InP that offers the best noise temperature and frequency performance while cooled down. However, developing InP transistors and MMICs is costly and has its own challenges such as reliability, stability and kink [59], [60] effect. This is an advantage for projects with the

scale of ngVLA where a very large number of LNAs with great consistency and reliability are required for the telescope's construction and maintenance.

The cryogenic LNA is required to have about 12 K noise temperature at cryogenic temperature. The required gain is about 30 dB with appropriate (about 10 dB) input and output return loss. The 12 K noise temperature translates to 84-120 K noise temperature in room temperature (assuming a factor of 7-10 for performance improvement after cooling down); that amounts to a noise figure of about 1.1-1.5 dB.

3.5.2 Design

A wideband 5-stage low noise amplifier is designed that covers the 30-52 GHz band with a double resonance input matching technique that allows for simultaneous wideband noise and input reflection matching. The LNA is designed to achieve the average noise temperature of 12 K over the bandwidth of interest. A co-design approach was employed that takes into account the effect of interconnection at the input and output of the chip and compensates for the effect of wire bonds with on-chip pad design. The final simulation results show a minimum noise figure of 1 dB at room temperature and less than 1.2 dB over the entire band. The LNA gain is 33-36 dB over the bandwidth of interest with the coaxial chassis.

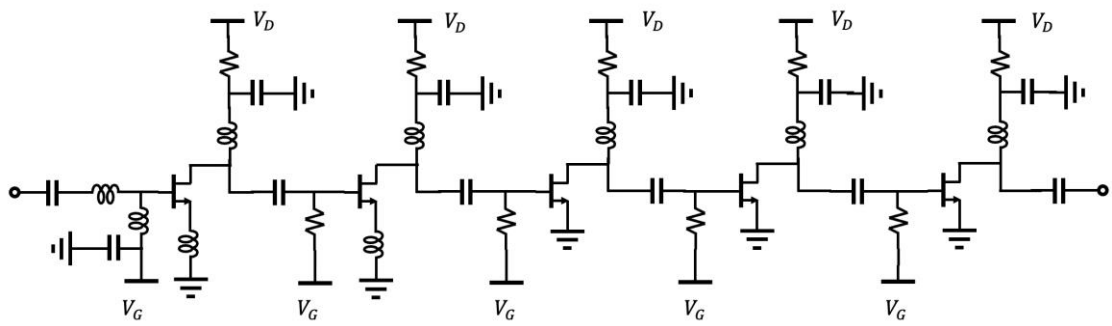

Figure 3.25. Schematic design of the Q-Band LNA.

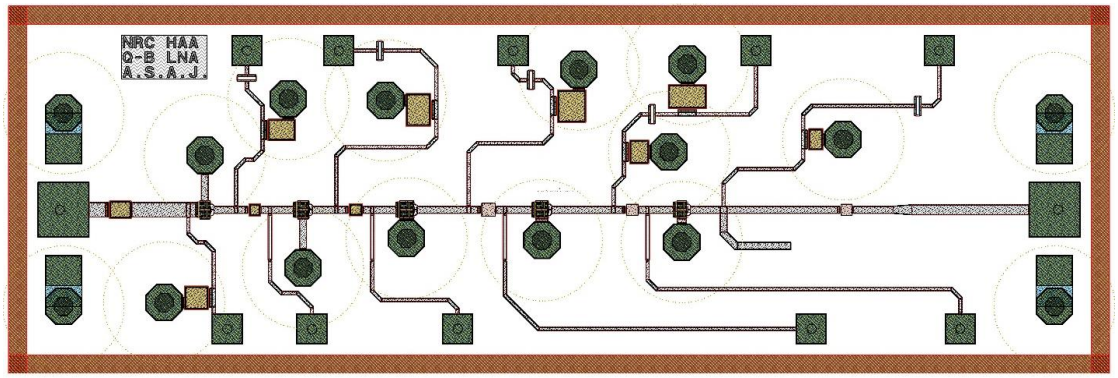

Figure 3.26. Layout of the Q-band LNA.

Figure 3.25 shows the schematic of the designed LNA. The LNA layout that is submitted to OMMIC for fabrication is shown in Figure 3.26. Figure 3.27 presents the final EM simulation results.

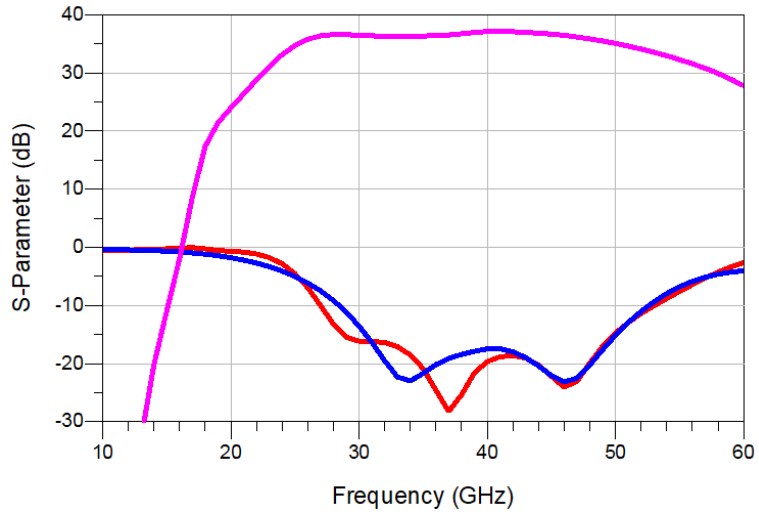

(a)

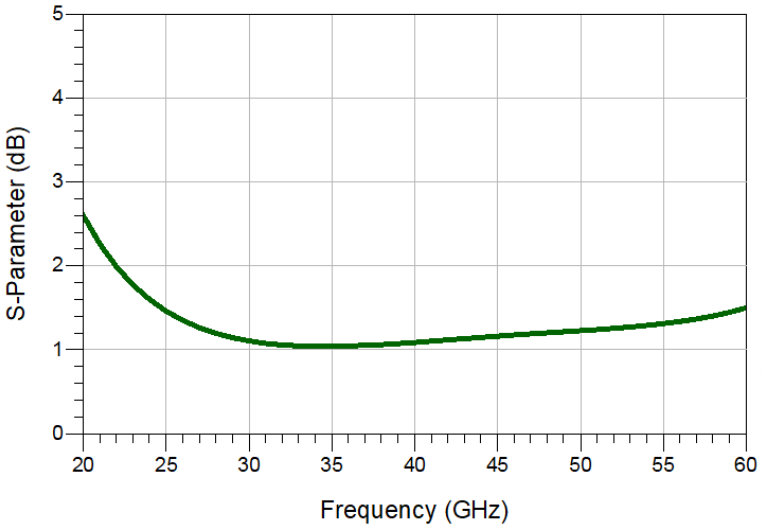

(b)

Figure 3.27. Simulated results of the Q-Band LNA

The fabricated LNA as shown in Figure 3.28 was first tested on the probe station to evaluate the bare die and next was assembled in a custom design coaxial chassis as shown in Figure 3.29. The gold plated copper-tellurium chassis was designed to provide thermal heat conductivity and biasing signals while preventing any higher order mode excitation in the main chamber. Careful design of the pillar size and gap allows openings for DC wire bonding without RF signal leaking to the outside.

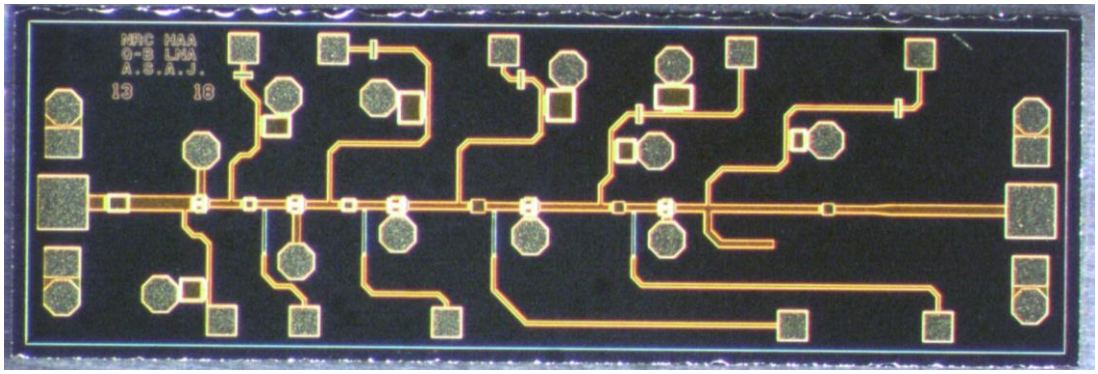

Figure 3.28. Microphotograph of Q-Band LNA.

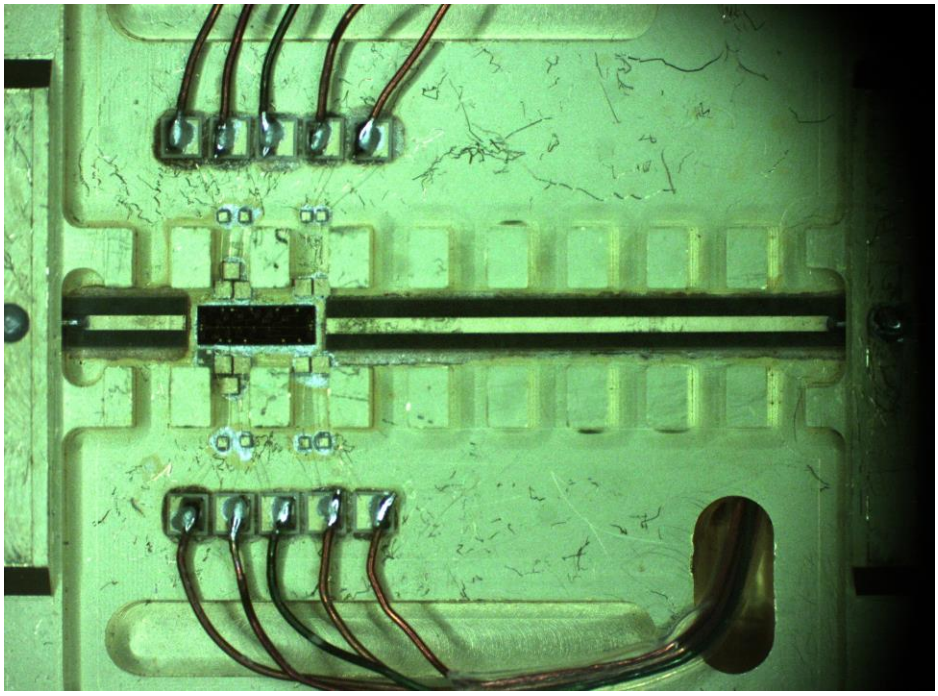

Figure 3.29. Assembled LNA in chassis. The pillars are placed on both side of the microstrip lines to prevent waveguide mode excitation in the chassis. The openings allow for access to the chip.

3.5.3 Measured Results

The packaged LNA was measured using a Keysight N227B PNA with coaxial calibration to extract the S-parameters, and the noise performance was evaluated by using a Rohde&Schwartz Spectrum Analyzer with noise figure measurement option.

Figure 3.30 shows the measured results; the LNA has more than 30 dB gain across the band with low output reflection. The input reflection shows the same wideband profile with

some degradation due to transitions between coaxial connectors, glass bead and microstrip line; similarly behavior is observed for the output reflection.

The LNA has a very wide bandwidth of 30-52 GHz; however, the measured results shown in Figure 3.30 (a) show that the amplifier has a gain of more than 23 dB at frequencies as low as 20 GHz and goes beyond 60 GHz. Such broad bandwidth creates many challenges in measuring the noise figure especially for a high gain low noise DUT at mm-wave frequencies where measurement equipment has high internal noise. To overcome the noise of the test equipment, a pre-amplifier is required to achieve a proper noise calibration (a calibration Y-factor that is higher than at least 3 dB) before performing the measurements. The use of a pre-amplifier with high enough gain while measuring a high gain DUT that is very wideband results in a high absolute power at the input of the noise analyzer that easily drives the internal receiver to saturation and corrupts the measurements. Considering the gain of the DUT and pre-amplifier used for this measurement as well as input matching of the LNA, the uncertainty of measurements is as high as 0.8 dB with the assumption of no saturation. Figure 3.30 (b) shows the measured noise figure where such an uncertainly is clearly visible around the predicted DUT noise figure. Considering this uncertainty, the LNA has measured noise figure is about 1.6 dB.

The entire LNA chip consumes 80 mW power using 0.8 V drain voltage and -0.2 V gate voltage. However, the bias lines can be separately tuned for the optimum V_{dd} and V_{gg} for further improvement in the results. The LNA is designed for a small size of 1 x 3 mm^2.

Table 3.2 summarizes the LNA results in comparison with other published works in similar frequency bands which shows this LNA provides a wideband gain and noise performance while maintaining a good input return loss (fully packaged) that is necessary for radio astronomy applications. This LNA is a five-stage amplifier in contrast to other designs that use four stages, hence the higher consumption.

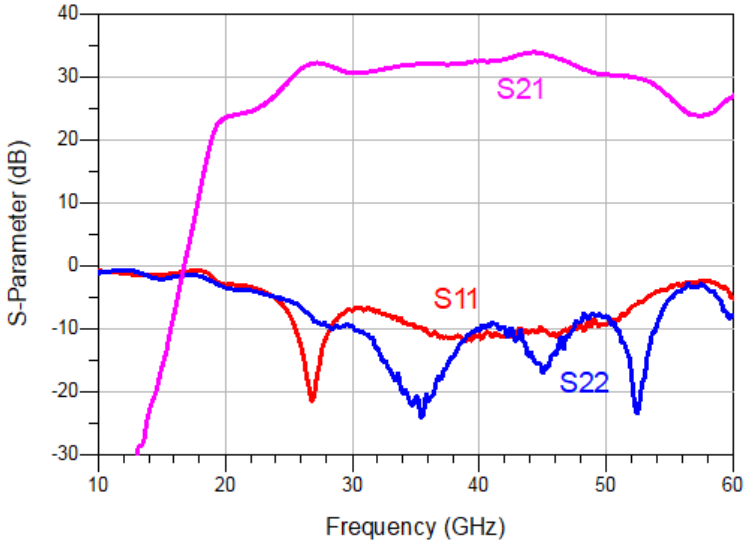

(a)

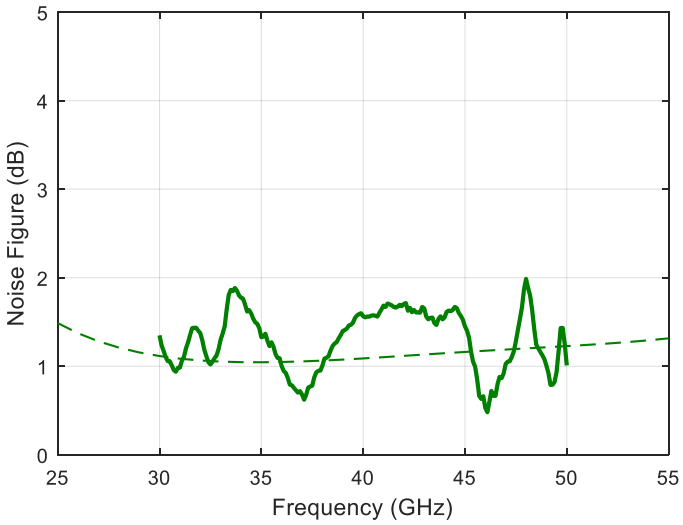

(b)

Figure 3.30. Measured results of the Q-Band LNA. Measured (solid line) and simulated (dashed line) (a) S-parameters. (b) noise figure.

Table 3.2. Summary of published Q-band LNA performances.

Reference	Technology	Freq (GHz)	NF (dB)	S_{11} (dB)	Gain (dB)	V_{dd} (V)	P_{DC} (mW)
[107]	mHEMT GaAs MMIC	33-50	1.8	-6	27	0.35	15.2
[108]	pHEMT GaAs MMIC	27-45	3.1	-5	25	1	38
[109]	pHEMT GaAs MMIC	37-52	3.2	N.A	32.5	2	46
[110]	InP HEMT MMIC	32-52	1.8	-10	35	1.2	52
This work	mHEMT GaAs MMIC	30-52	1.6	-10	32	0.8	60

Chapter 4

Mm-Wave Down-converter Design

Radio telescopes operate in the 1MHz to 1 THz range and, except for small fractions of the spectrum that can be directly digitized by analog to digital converters (ADCs), the majority of the receivers require a down converter to translate the RF signal into a low frequency band to be digitized. Regardless of the architecture of the receiver, whether it is super heterodyne or direct conversion, at frequencies above about 8 GHz, the RF band (sub-band) is multiplied by a local oscillator signal and down converted to the standard IF or base band (or low IF).

In mm-wave astronomy, especially where cryogenic low noise amplifiers can be used in the RF band (30-120 GHz), the RF signal must be down converted using a mm-wave mixer (at 150-1000 GHz, SIS mixers are used which down convert the signal before it is amplified by an IF LNA). The high frequency of operation constitutes a challenge for selecting commercial mixers that cover the frequency range of interest with consistent performance. Ideally, the mixers should have a constant conversion gain, high isolation, low input return

loss (at RF, LO and IF ports), and operate with a low power local oscillator since providing a high LO power at mm-wave frequencies is expensive and increases the complexity of the telescope's backend. To address these requirements, three mixers have been developed for mm-wave frequencies based on the driving requirements for near future radio telescopes such as DVA-2 and ngVLA: two mixers in Q-band based on SiGe HBT and GaAs pHEMT and one mixer in W-band (70-120 GHz) based on SiGe BiCMOS. The GaAs mixer (33-55 GHz) demonstrates a single cascode design for wideband performance. The Q-band SiGe HBT mixer (35-50 GHz) is a differential Gilbert cell for the super heterodyne receiver of the DVA2 telescope. And the W-band mixer is an in-phase/quadrature (I/Q) mixer with two Gilbert cell cores for a direct conversion receiver architecture of the ngVLA telescope.

4.1 Mixer Design Theory

The frequency translation is a nonlinear phenomenon that can be realized in a mixer when a parameter of the circuit, such as the gain transconductance that is associated with the primary signal (RF or IF) has nonlinear dependence to a secondary parameter in the circuit that can be controlled by a secondary signal (LO). Assume an RF signal is applied to the gate of a FET device as shown in Figure 4.1, where the AC current of the FET, i_{ds}, can be controlled by a secondary signal. Assuming a simple linear dependency of g_m to the LO signal:

$$v_o = i_{ds} R_d \tag{4.1}$$

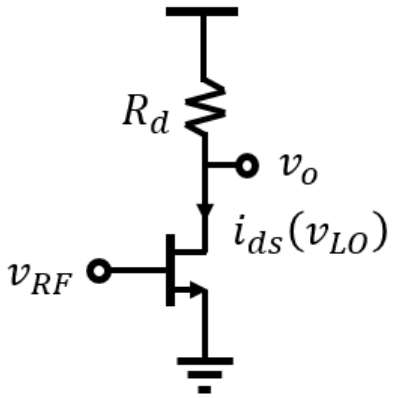

Figure. 4.1. Basic mixing device.

$$i_{ds} = g_m v_{LO} \tag{4.2}$$

$$v_o = g_m v_{LO} R_d v_{RF} \tag{4.3}$$

For two sinusoidal signals,

$$v_o = g_m R_d V_{LO} cos(\omega_{LO} t) V_{RF} cos(\omega_{RF} t) \tag{4.4}$$

$$v_o = \frac{g_m R_d V_{LO} V_{RF}}{2} \left[cos\big((\omega_{LO} - \omega_{RF})t\big) + cos((\omega_{LO} + \omega_{RF})t) \right] \tag{4.5}$$

In the case of a down converter, the difference term is set to fall into the desired IF frequency range and in an up converter, the summation falls into the RF frequency range.

In order to create the dependency of g_m on the LO signal, a secondary device is used as shown in the Figure 4.2. Note that in an enhancement mode FET with quadratic IV relation, g_m equals

$$I_{ds} = I_{sat}\big(V_{gs} - V_p\big)^2 \tag{4.6}$$

$$g_m = \frac{\delta I_{ds}}{\delta V_{gs}} = 2I_{sat}\big(V_{gs} - V_p\big) = 2\sqrt{I_{sat} I_{ds}} \tag{4.7}$$

And if the device is a bipolar device,

$$I_c = I_s exp\left(\frac{V_{be}}{v_{th}}\right) \tag{4.8}$$

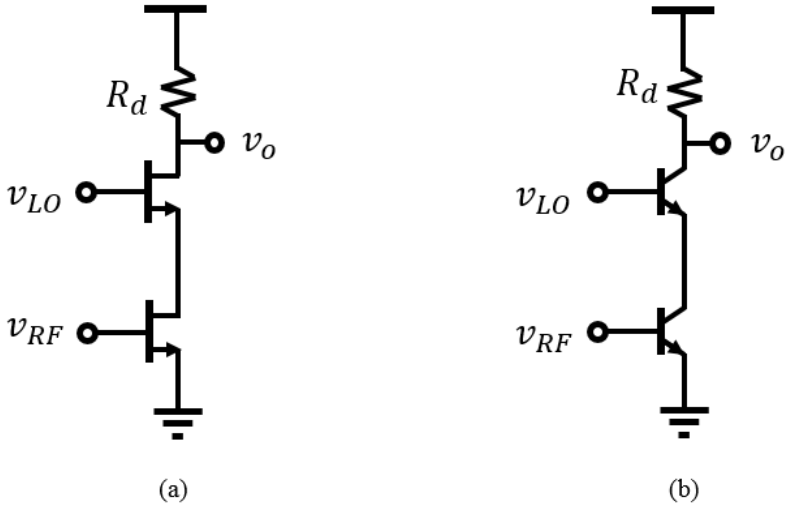

Figure 4.2. Basic mixer: (a) FET, (b) BJT.

$$g_m = \frac{\delta I_c}{\delta V_{be}} = \frac{1}{v_{th}} I_s exp\left(\frac{V_{be}}{v_{th}}\right) = \frac{I_c}{v_{th}} \tag{4.9}$$

This results in a mixer conversion gain of

$$Conversion\ Gain = \frac{1}{2} g_m R_d V_{LO} \tag{4.10}$$

This shows that the conversion gain can be improved by a resistive load, R_d, the transconductance of the cascode device, g_m, or the amplitude of the LO signal V_{LO}. However, increasing R_d limits the output swing, especially in low power applications, increasing g_m requires higher bias current and larger DC power, and a larger LO signal is expensive at mm-wave frequencies.

Note that in a FET device, g_m has a linear dependence on V_{gs} while in a bipolar device, it is nonlinear. The circuits shown in Figure 4.2 are cascode topologies that, along with circuits shown in Figure 4.3, are the simplest transistor based mixer topologies. In Figure 4.3 (a) and (b) the LO and RF signal appear in the V_{gs} and are multiplied by each other due to the quadratic I-V characteristic of the FET. Note that in all the three configurations in Figure 4.3, the RF and LO signals directly appear in the output in addition to the desired IF component, hence the isolation between RF and LO ports and the IF port is minimal.

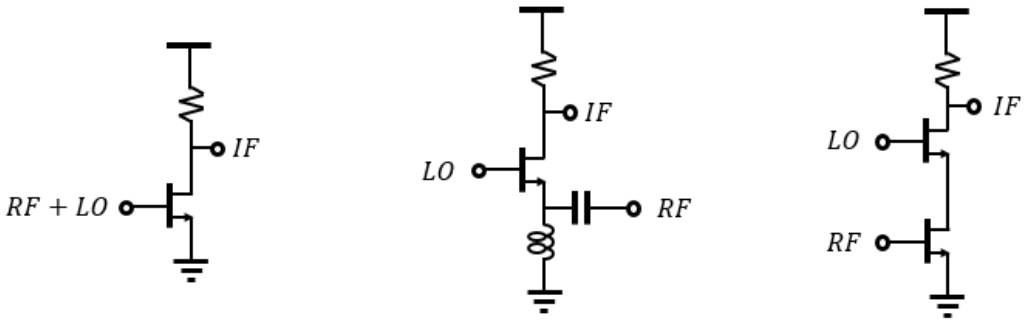

Figure 4.3. Active mixer topologies: (a) common source with LO and RF applied to gate, (b) common source where LO and RF are applied to gate and source, (c) cascode.

To remedy this and especially to reduce the LO and RF leakage, balanced configurations can be used for both FET and bipolar devices. Figure 4.4 shows a single balanced and

double balanced configuration. A single balanced mixer requires lower power and a simpler structure; however, the more complex double balanced circuit provides the best isolation at the cost of consuming more power. In addition, the double balanced circuit requires two baluns at the RF and LO port compared to the single balanced one that requires only one balun at the LO port.

In a double balanced mixer, commonly known as a Gilbert cell mixer, shown in Figure 4.5, the difference between currents (blue arrows) of Q_3 and Q_4 when the LO signal is applied can be obtained [74] as

$$\Delta I_{3,4} = I_3 - I_4$$

$$= I_{ss}\left[exp\left(\frac{V_{BE3}}{V_{th}}\right) - exp\left(\frac{V_{BE4}}{V_{th}}\right)\right] = I_{ss}exp\left(\frac{V_{BE4}}{V_{th}}\right)\left[exp\left(\frac{V_{BE3}-V_{BE4}}{V_{th}}\right) - 1\right]$$

$$= I_{ss}exp\left(\frac{V_{BE4}}{V_{th}}\right)\left[exp\left(\frac{v_{LO}}{V_{th}}\right) - 1\right] \quad (4.11)$$

where v_{LO} is the differential LO signal at the base of Q_3 and Q_4, and v_{th} is the thermal voltage. The sum of the Q_3 and Q_4 currents equals the Q_1 current:

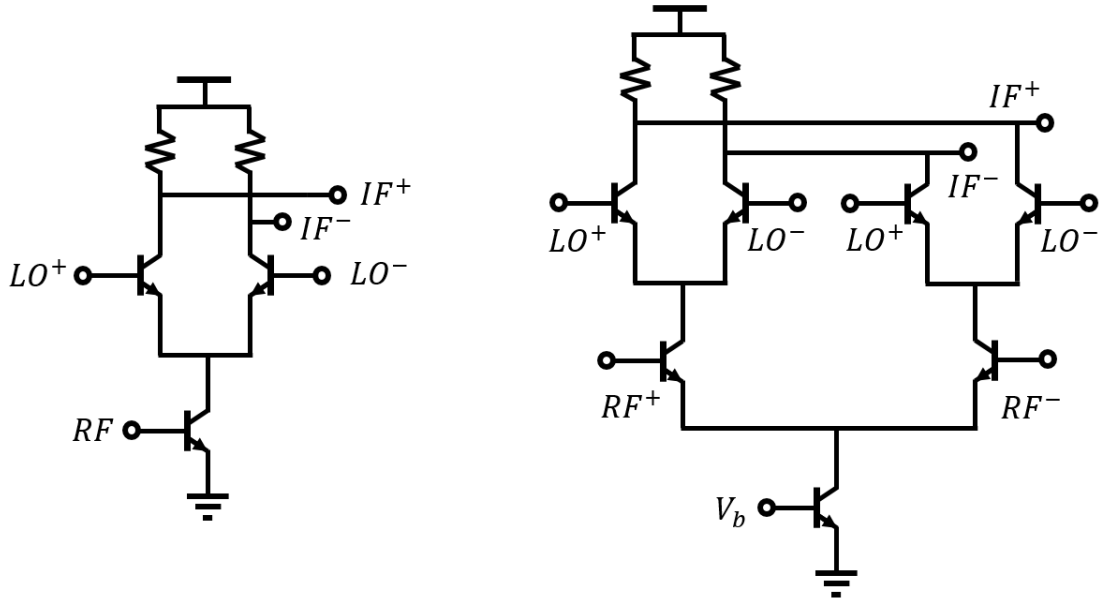

Figure 4.4. Single (left) and double (right) balanced cascode mixer topologies.

$$I_1 = I_3 + I_4$$

$$= I_{ss}\left[exp\left(\frac{V_{BE3}}{V_{th}}\right) + exp\left(\frac{V_{BE4}}{V_{th}}\right)\right] = I_{ss}exp\left(\frac{V_{BE4}}{V_{th}}\right)\left[exp\left(\frac{V_{BE3} - V_{BE4}}{V_{th}}\right) + 1\right]$$

$$= \quad I_{ss}exp\left(\frac{V_{BE4}}{V_{th}}\right)\left[exp\left(\frac{v_{LO}}{V_{th}}\right) + 1\right] \tag{4.12}$$

Combining (4.11) and (4.12),

$$\Delta I_{3,4} = I_1 tanh\left(\frac{v_{LO}}{2V_{th}}\right) \tag{4.13}$$

Similarly,

$$\Delta I_{5,6} = I_2 tanh\left(\frac{v_{LO}}{2V_{th}}\right) \tag{4.14}$$

Taking the same approach for Q_5, Q_6 and Q_2:

$$\Delta I_{1,2} = I_{tail} tanh\left(\frac{v_{RF}}{2V_{th}}\right) \tag{4.15}$$

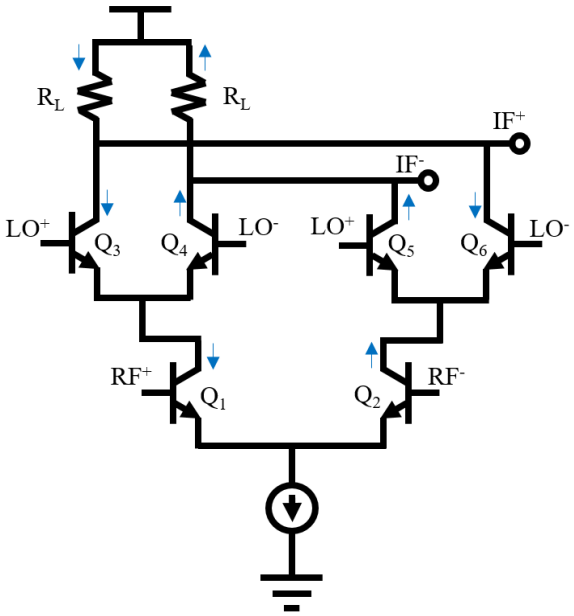

Figure 4.5. Gilbert cell AC current representation.

where I_{tail} is the total tail current, and v_{RF} is the differential RF voltage applied at the base of Q_1 and Q_2. The differential output voltage, v_{IF}, is

$$v_{IF} = \Delta I_{IF} R_L = [(I_3 + I_6) - (I_4 + I_5)]R_L = \left[\Delta I_{3,4} - \Delta I_{5,6}\right]R_L \tag{4.16}$$

where R_L is the load at the collector of the mixing quads. Replacing (4.13), (4.14) and (4.15) in (4.16) gives the large signal differential IF voltage

$$v_{IF} = R_L I_{tail} tanh\left(\frac{v_{RF}}{2V_{th}}\right) tanh\left(\frac{v_{LO}}{2V_{th}}\right) \tag{4.17}$$

Assuming that the RF signal is small, (4.17) simplifies to

$$v_{IF} = R_L \frac{I_{tail}}{2V_{th}} v_{RF} tanh\left(\frac{v_{LO}}{2V_{th}}\right) \tag{4.18}$$

In the case where the LO signal is large enough, the *tanh* function can be approximated by the Fourier series of a square wave, and taking into account the frequency component at the desired IF frequency, the mixer gain is

$$CG = \frac{v_{IF}}{v_{RF}} = \frac{2}{\pi} R_L g_m \tag{4.19}$$

where I_{tail}/V_{th} is the g_m of Q_1.

Mixing also can be realized using diodes that are switched by the LO signal as depicted in Figure 4.6. In a diode based design (or transistor based design when the FET or bipolar devices are switch on/off with a large signal LO), where the RF signal is switched to 1 and 0, the current through the load resistance, R_L, can be obtained by multiplying the RF voltage

with the time-varying transconductance of the switch that can be represented as a Fourier series of a train pulse [111]:

$$g_{switch}(t) = \frac{1}{2R_L} + \sum_{n=1}^{\infty} \frac{2}{n\pi R_L} sin\left(\frac{n\pi}{2}\right) cos(n\omega_{LO}t) \tag{4.20}$$

$$v_0 = g_{switch}(t) v_{RF} R_L \tag{4.21}$$

$$v_0 = \frac{R_L}{2R_L} V_{RF} cos(\omega_{RF}t) + \sum_{n=1}^{\infty} \frac{2R_L}{n\pi R_L} sin\left(\frac{n\pi}{2}\right) cos(n\omega_{LO}t) V_{RF} \cos(\omega_{RF}t) \tag{4.22}$$

$$v_0 = \frac{V_{RF}}{2R_L} cos(\omega_{RF}t) +$$

$$\sum_{n=1}^{\infty} \frac{V_{RF}}{n\pi} sin\left(\frac{n\pi}{2}\right) \left[cos\left((\omega_{LO} - \omega_{RF})t\right) + cos((\omega_{LO} + \omega_{RF})t)\right] \tag{4.23}$$

The first component, when *n*=1, results in the desired IF signal.

$$\frac{V_{RF}}{\pi} sin\left(\frac{\pi}{2}\right) cos\left((\omega_{LO} - \omega_{RF})t\right) \tag{4.24}$$

The conversion gain equals

$$Conversion\ Gain = \frac{1}{\pi} \tag{4.25}$$

This is the maximum available gain from a switch based mixer, about -9.9 dB. However, in practice, mismatch and resistive loss reduce the conversion gain. In this configuration the RF signal power is wasted for half of the LO signal cycle (when switch is open). Note

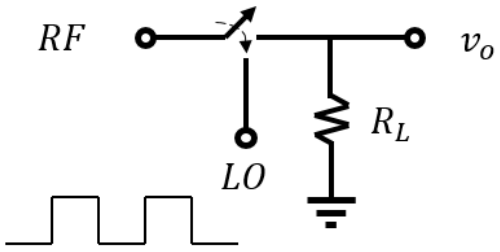

Figure 4.6. Switch based mixer.

that to remedy this, a balanced switch configuration can be used in which the signal power is used in both states of the LO resulting in 3dB higher conversion gain.

The output signal of the mixer contains many frequency components that ideally should be minimized as they are considered noise compared to the desired signal. However, each of the RF and LO signals as well as their higher order products emerge in the output signal spectrum. Thus a mixer in an RF system can be characterized by its

- conversion gain
- LO to IF leakage
- LO to RF leakage
- RF to IF leakage
- input matching at RF, LO and IF ports
- LO power level required for proper operation
- input/output gain compression point
- noise
- I/Q mismatch (in case of an I/Q mixer)

4.2 SiGe HBT Mixer for 35-50 GHz

The DVA-2 Q-band receiver design utilizes a heterodyne architecture where the 35-50 GHz RF spectrum is divided into two 8-GHz sub-bands, 35-43 GHz and 42-50 GHz for each of the two polarizations. Each sub-band is down-converted to an 8-16 GHz IF suitable for digital processing. The DVA-2 Q-band receiver design was a precursor for an ongoing development project at NRC targeted towards a design for the ngVLA Band 5 receiver. The mixer should be able to cover the entire RF band with acceptable input return loss, a consistent conversion gain and high isolation. The high conversion gain can relax the cryogenic LNA/warm RF amplifier gain requirement. Mixers presented in [112] [113] [114] [115] introduce conversion loss and poor input match at the RF port.

As discussed in Chapter 1, in a conventional radio receiver chain, many isolators and amplifiers are used after the low noise amplifier to prevent LO signals leaking back to the antenna and disturbing adjacent receivers as well as reducing the standing wave ratio between amplifier and mixer. However, if the mixer has high conversion gain, high LO-

to-RF isolation and good input matching, the isolator and extra buffer amplifiers can be removed to simplify the system architecture. It is important to note that unlike the LO and RF leakage to the IF path, the LO-to-RF leakage cannot be readily resolved by using a filter. The LO and RF frequencies are close and are only a few GHz apart in the mm-wave frequency band, and the LO frequency range overlaps with the RF frequency band. Thus, a fixed frequency filter is not practical for tunable LO operation. A common method is using subharmonic mixers [116] [117] where the RF and LO subharmonics are separated and the LO to RF leakage can be suppressed by using a simple filter. However, they require high LO power and are associated with conversion loss.

Moreover, if the mixer provides adequate LO-to-IF isolation, the band pass filter can be removed from the receiver, resulting in fewer components required.

Another important factor that mixers presented in [118] [119] [120] lack is the ability of operating with low LO power. Those designs require at least 0 dBm LO power to operate properly to provide conversion loss of less than 15 dB. A down-converter system that operates with lower LO power is beneficial, especially in large array radio telescope systems.

A 1 dBm difference in LO power may seem small in a linearly polarized single dish telescope but it becomes significant when multiplied by the number of polarizations, sub-bands, bands and antennas of a large array of radio telescopes. The ability of operation with low LO power reduces the complexity of the LO distribution system, especially in large telescope arrays with hundreds of receivers.

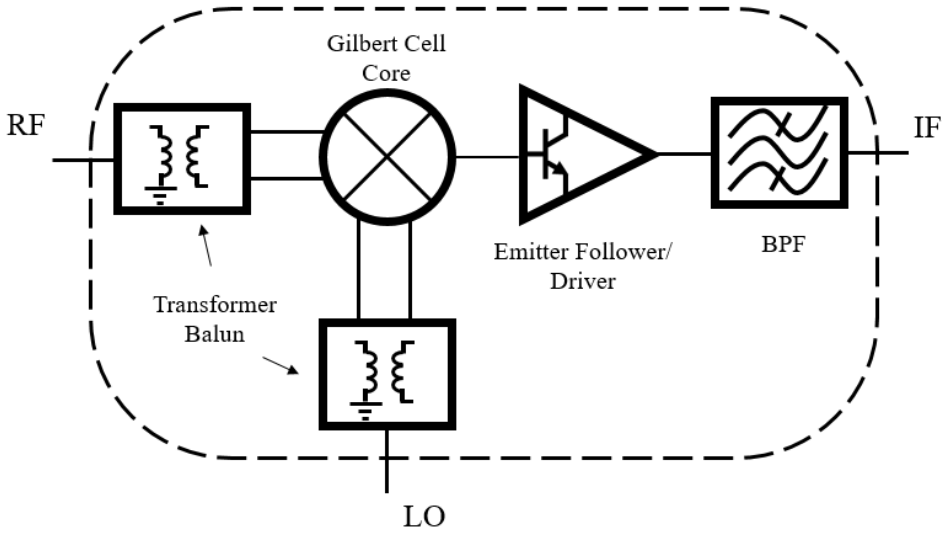

Figure 4.7. Bock diagram of the down-converter mixer.

The down-converter choice of technology is the IHP SiGe 130 nm process which offers high performance npn HBTs presented in Section 2.2.1. The down-converter block is designed based on a double balanced Gilbert cell mixer which provides a better LO to RF/IF isolation compared to single ended and single balanced configurations. The double balanced mixer requires differential RF and LO signals at the transconductor pair and the mixing quads, respectively. Thus, two on-chip transformer baluns at the RF and LO ports are used to convert the single-ended signals to differential ones. The mixer core is followed by a buffer stage that prevents the loading of the mixer by the next block.

Finally, an on- chip filter blocks the LO and RF signals from leaking into the IF outputs. Figure 4.7 shows the block diagram of the down-converter chip. And Table 4.1 summarizes the down converter requirements.

Table 4.1. 35-50 GHz down-converter requirements.

Conversion Gain (dB)	> 5
Gain flatness (dB)	2
LO driving power (dBm)	-10
RF frequency (GHz)	35-50
LO frequency (GHz)	27-34
IF frequency (GHz)	8-16
RF port return loss (dB)	< -10
IF port return loss (dB)	< -10
LO port return loss (dB)	< -10
LO to IF Isolation	> 30
LO to RF Isolation	> 40
RF to IF Isolation	> 30
3 % input gain compression point (dBm)	> -20

4.2.1 Mixing Core

Considering the power budget, a 3.3-V standard power supply and a 16-mA tail current were used as shown in Figure 4.8 (a) and the transistor sizes were designed accordingly for desired current density that provides high switching speed and low noise performance for the switching quad and transconductor pair, respectively. Resistive loading is chosen over inductive peaking to provide wideband performance. However, R_L and the tail current, and hence g_m, cannot be very large since the voltage drop across the resistor is limited, resulting in a relatively low gain. Therefore, considering the collector-emitter break-down voltage, the mixer is biased for maximum output swing which results in about 400 mV voltage drop across R_L. The main linearity constraint is imposed by the input swing that is very limited due to the fact that the voltage at the base of the transconductor pair cannot swing more than a few mV without the collector current, as described by Equation (4.21), showing a nonlinear dependence to v_{RF}. This results in a voltage saturation across the load, and the linear region is only a few mV wide, about v_{th} = 25 mV.

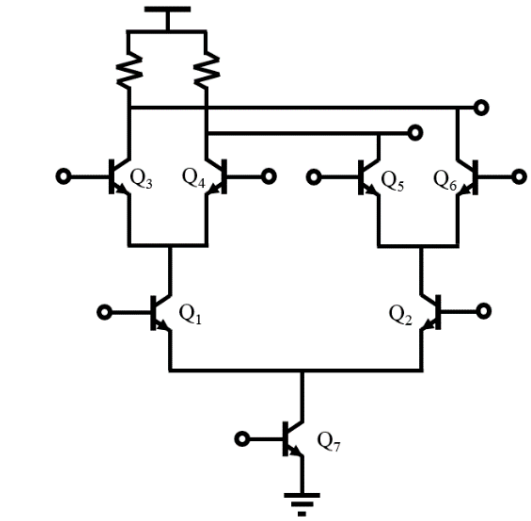

(a)

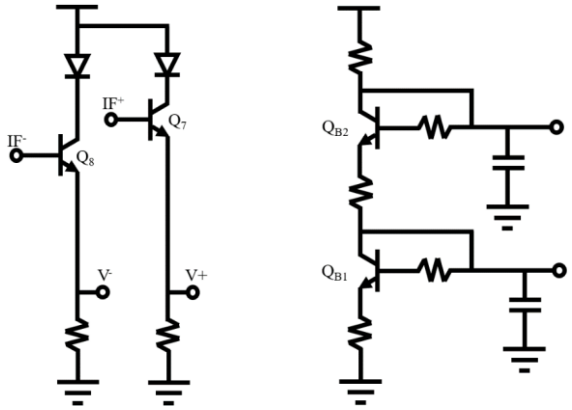

(b) (c)

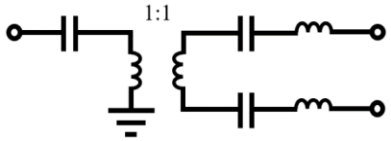

(d)

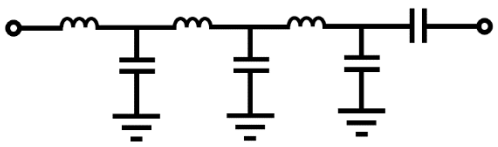

(f)

Figure 4.8. Simplified circuit schematics: (a) mixer core, (b) output buffer, (c) bias circuit, (d) RF and LO transfer balun, and (e) matching network filter.

In order to alleviate the input swing problem, an inductor can be added at the emitter of the transconductor pair. The degeneration allows the AC voltage of the emitter to be a non-zero value. Thus, the HBT can tolerate a larger swing at the input. This largely improves the 1-dB input compression point as well as the input impedance match. The major drawback of this approach is reducing the effective g_m and causing a lower conversion gain. Further degeneration could increase the input 1-dB compression, but the conversion gain will become negative. At some point, the linearity is limited by the output swing at the IF.

An emitter follower, shown in Figure 4.8 (b) is placed between the mixer output and the band pass filter to act as a buffer and reduce the loading of the mixer. The diodes at the collector of the emitter followers are diode-connected HBTs that shift the V_{DD} to a lower level to prevent the breakdown of transistors.

The bias circuit shown in Figure 4.8 (c) provides the required voltages for the mixer core. The resistor between the collector of Q_{B1} and the emitter of Q_{B2} in the bias circuit provides a voltage drop that allows for some headroom at the collector of the transconductor pair, thus allowing a larger swing. The resistor added at the collector of Q_{B2} allows using the standard 3.3-V supply voltage.

4.2.2 Passives

In order to capture the effect of the BEOL interconnection on the device performance, a 3D model of the metals and vias was developed. Normally, the device parameters provided by semiconductor foundries include the intrinsic device plus the first interconnect metal layer, and the rest are de-embedded. Therefore, it is critical to model the parasitic effects of the interconnections with access terminals at the top metal layers for mm-wave frequency circuits. For this purpose, two versions of the interconnection were designed as shown in Figure 4.9.

These structures were fully simulated, without via array simplification, using the Keysight Advanced Design System (ADS) finite element method (FEM) simulator. Figure 4.10 shows the insertion loss as well as the phase of the transition between device contact metal

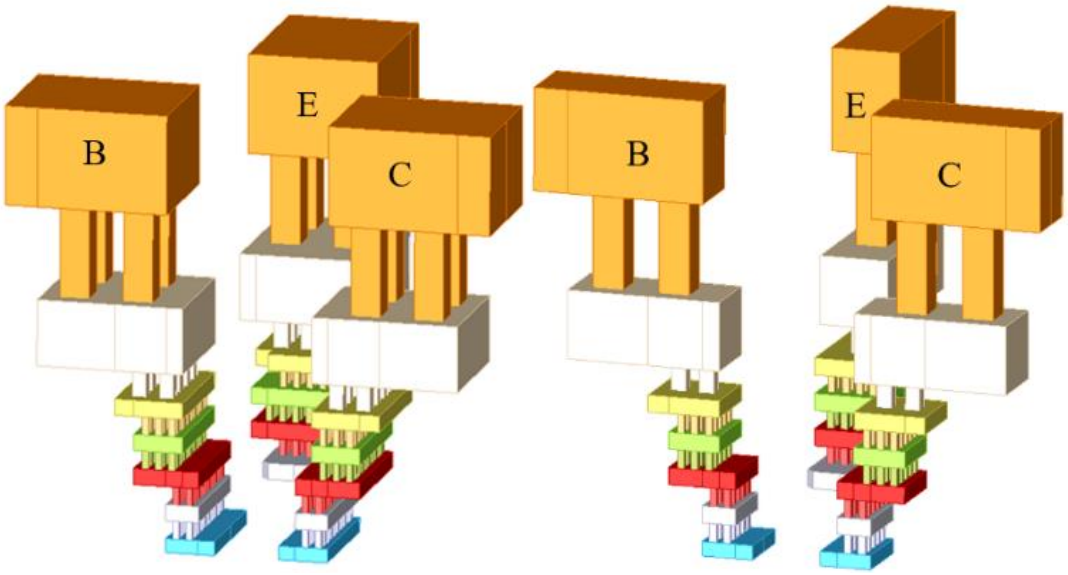

(a) (b)

Figure 4.9. 3D representation of a device metal interconnection for (a) low noise and (b) high speed mm-wave circuits.

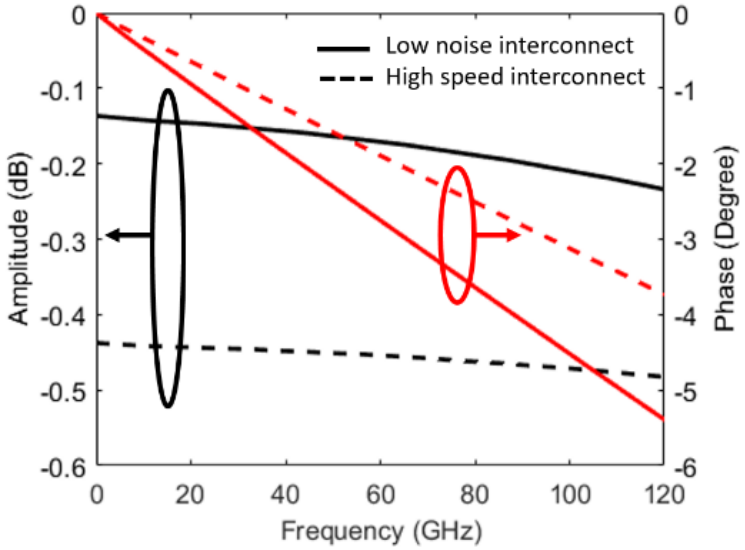

Figure 4.10. Simulated amplitude and phase of the transition between lower metal and top metal interconnect for the base of the HBT for low noise (solid line) and high speed (dashed line) interconnections.

and the top-metal terminals for low noise and for high speed. The former utilizes wider connections with more via counts that reduce the access resistance, making it a suitable choice for devices that are operating in low noise conditions.

However, the parasitic capacitances of the interconnections reduce the cut-off frequency of the device by 20%, as shown in Figure 4.11, compared to a device without the metal

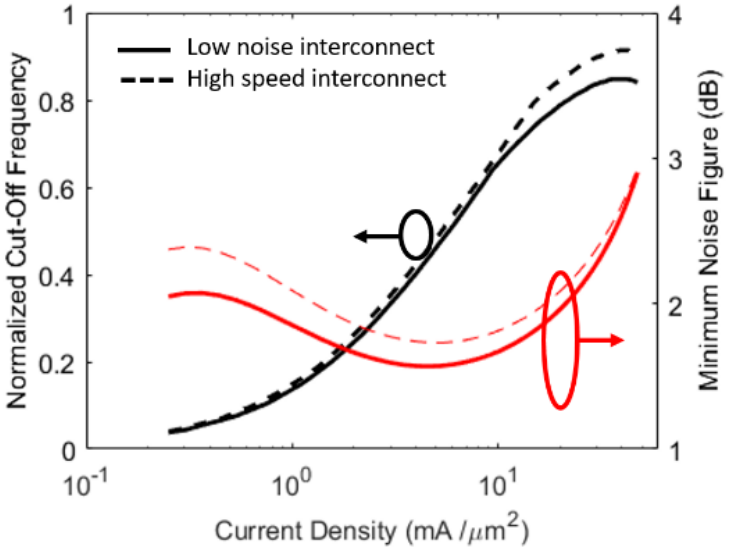

Figure 4.11. Simulated cut-off frequency (normalized to maximum cut-off frequency of the transistor without metal interconnect) and minimum noise figure (at 60 GHz) for a device with low noise (solid line) and high speed (dashed line) interconnects.

interconnections. The increase in minimum noise figure is 0.15 dB at 60 GHz. The latter, used in this design, is a high speed version where narrower interconnects are used to reduce the parasitic capacitance and preserve the cut-off frequency, with only 10% reduction in maximum cut-off frequency. This leads to a higher resistance and 0.32 dB increase in minimum noise figure of the device at 60 GHz compared to a bare transistor as shown in Figure 4.11.

Figure 4.12 (a) shows the transmission and bias line structure used in this work. The supply voltage is distributed using wide tracks with low impedance that are shielded by ground planes and walls. The base bias lines are at the lower narrow metal layers with high impedance and proper shielding. The transmission lines are realized by using a grounded coplanar structures with 6-7-6 µm G-S-G structure on the top metal, providing 50 Ω signal lines. Figure 4.12 (b) depicts the simulation results of the GCPW line with less than 1 dB/mm loss at 70 GHz.

To minimize the effect of bonding pads on the performance of the chip, the connection to the GCPW, shown in Figure 4.13 (a), was optimized for a 100 µm-pitch GSG. Figure 4.13 (b) presents the simulated GSG transition using FEM. The tapered ground location was

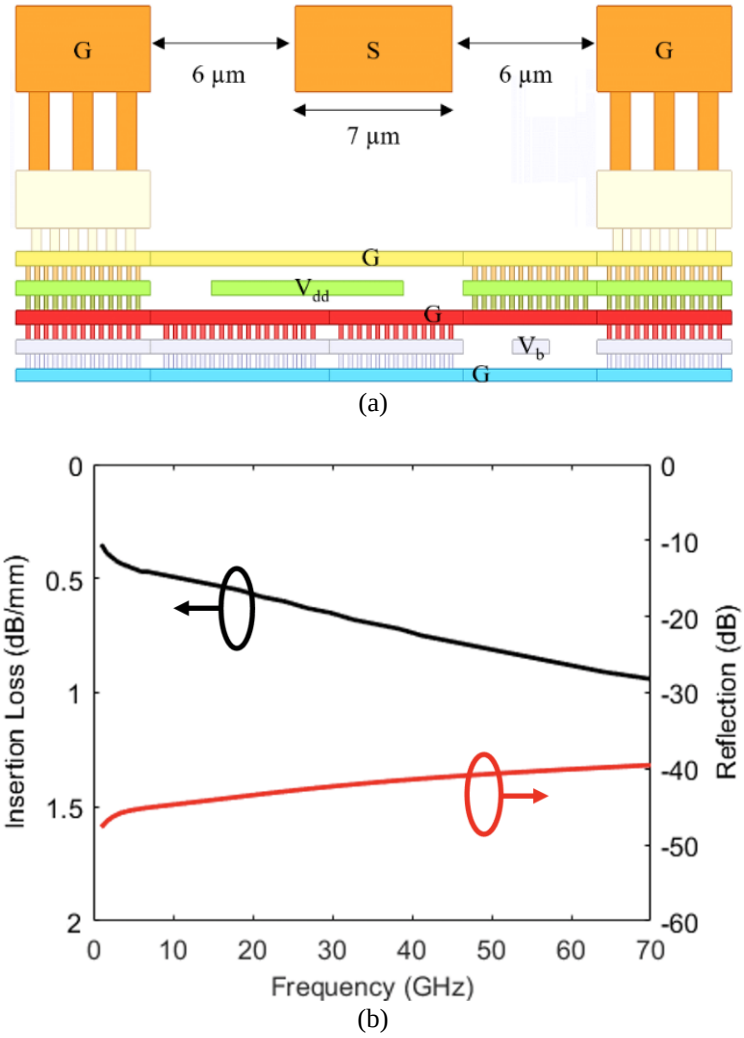

Figure 4.12. (a) Interconnection stack-up of transmission bias line structure, and (b) simulated performance of the GCPW.

chosen to provide low insertion loss and wideband match to 50 Ω up to 60 GHz. The simulation shows S_{11} < - 30 dB and S_{21} > -0.1 dB over the frequency of interest.

To convert the single ended input signals to differential ones, two on-chip transformer baluns were designed using the two thick top metal layers. As shown in Figure 4.8 (d), they are co-designed with the input matching network for RF and LO ports. As shown in Figure 4.14, both transformers have a 1:1 turn ratio and better than 0.6 dB and 0.8 dB amplitude and 1.5° and 2° phase balance for RF and LO baluns, respectively.

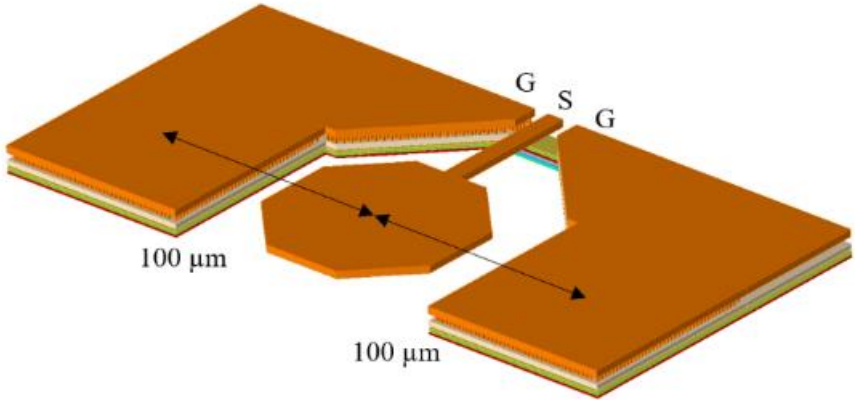

(a)

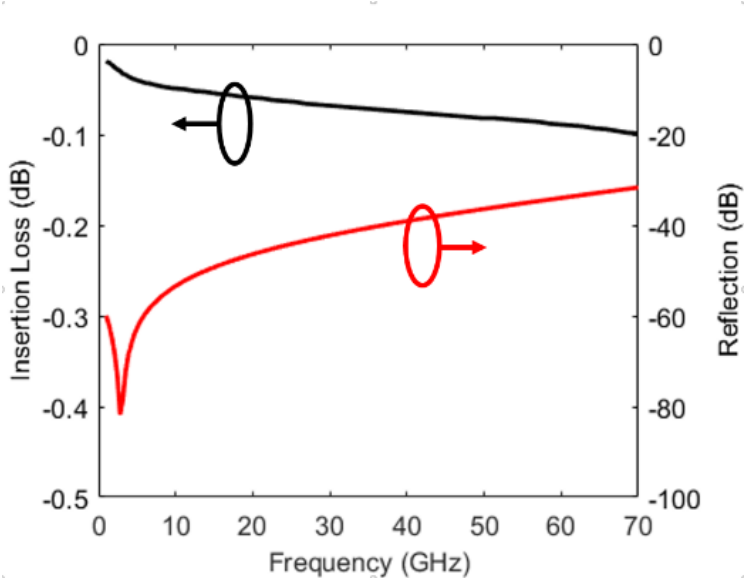

(b)

Figure 4.13. (a) 100 µm GSG transition to GCPW, and (b) simulation results of the 100 µm GSG transition to GCPW.

An offset in the diameter of the primary and secondary coils is applied to improve the frequency performance by reducing the capacitive coupling between metal tracks. Also, it helps to reduce the amplitude imbalance by compensating the difference in the resistive loss of the coils caused by different metal thickness.

Prior to connecting to the output pad, a 5th-order LC filter with a decoupling capacitor and having 30 dB attenuation in the stop band above 24 GHz, as depicted in Figure 4.8 (e), is placed at the IF port. Note that one of the differential IF signals is routed to the output.

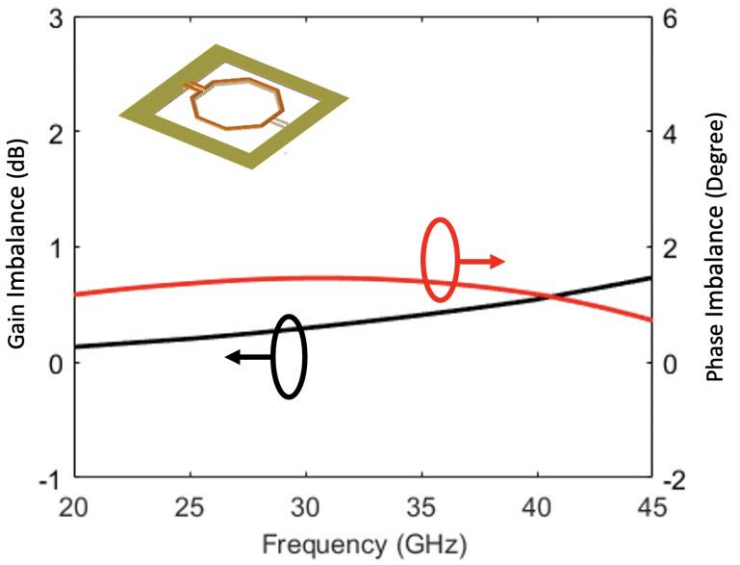

(a)

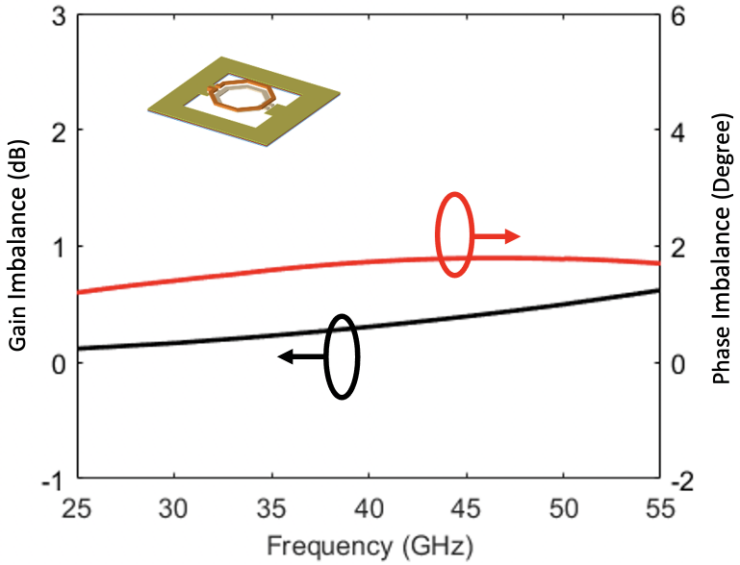

(b)

Figure 4.14. Simulated performance of the (a) LO and (b) RF transformer baluns.

Figure 4.15 shows the final layout of the down-converter after adding fillings and slits to pass the DRC.

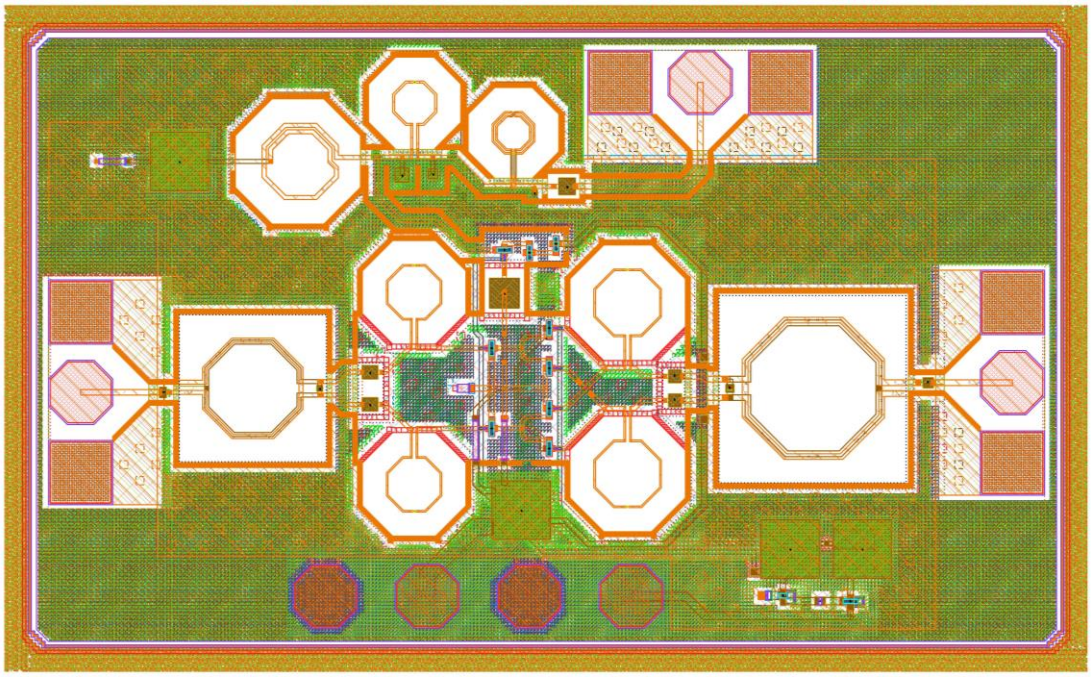

Figure 4.15. Layout of the down-converter chip.

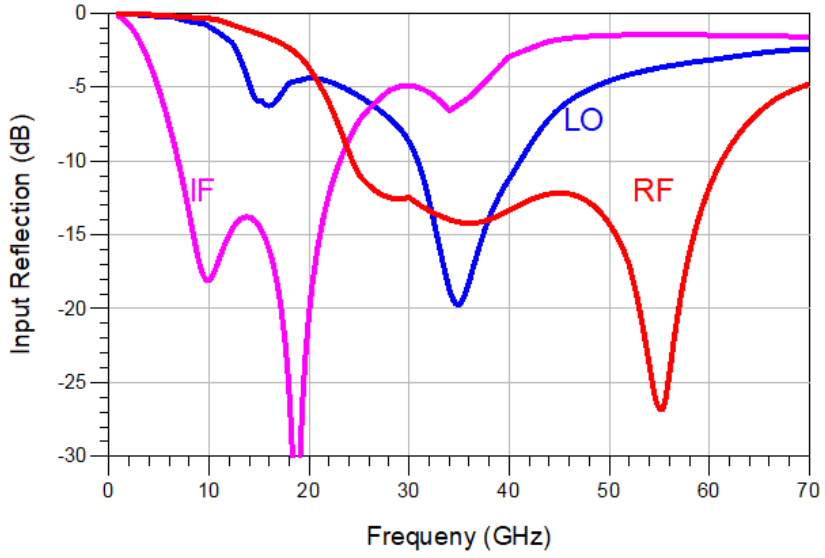

Figure 4.16. Simulated input reflection of the down-converter.

Figure 4.16 shows the simulated reflection of the three ports which is below -10 dB for all parts over the frequency range of interest.

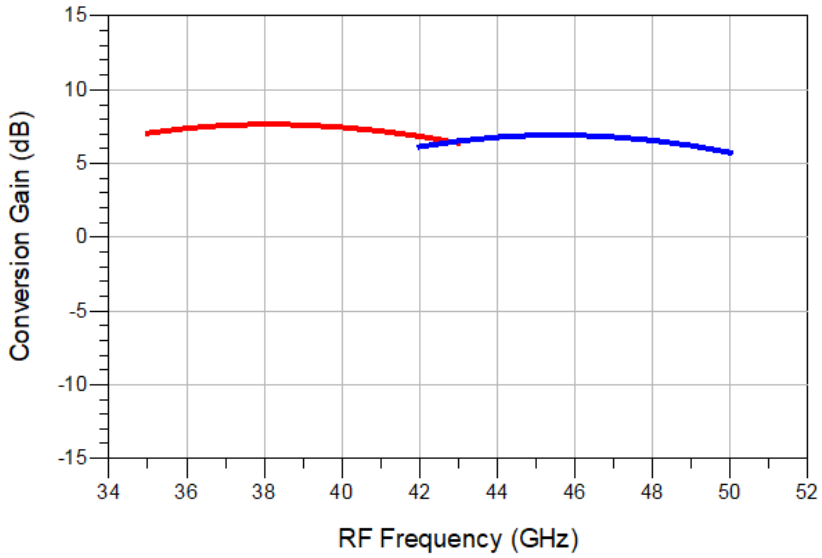

Figure 4.17. Simulated conversion gain for upper two RF sub-bands.

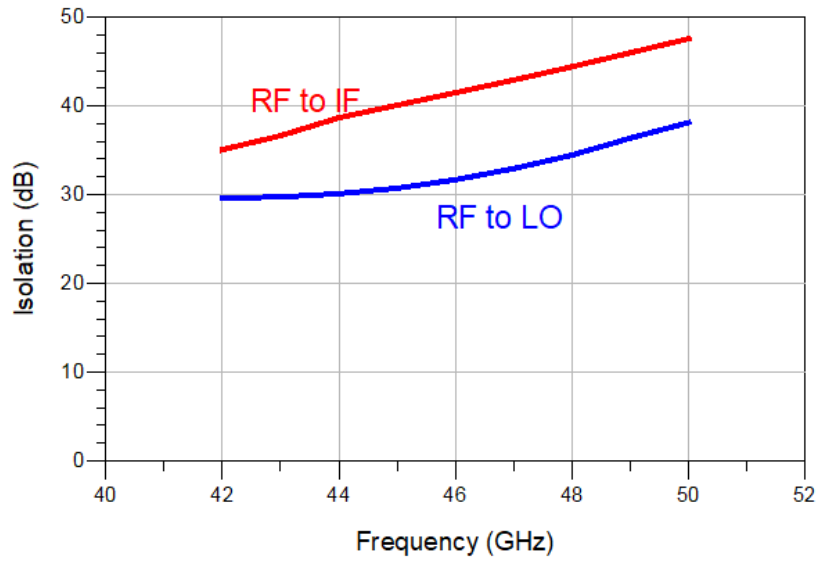

Figure 4.18. Simulated isolation of RF to IF and LO.

The conversion gain of the mixer, shown in Figure 4.17, is 5-8 dB over the entire RF band. The isolation of the mixer for LO to IF and RF and RF to IF and LO is presented in Figure 4.18 and 4.19, respectively. The conversion gain compression is a good criterion for the linearity of the mixer that is shown in Figure 4.20. Values for a different LO, 34 GHz, are similar. The mixer has a -13 dBm input compression and equivalent -7 dBm output

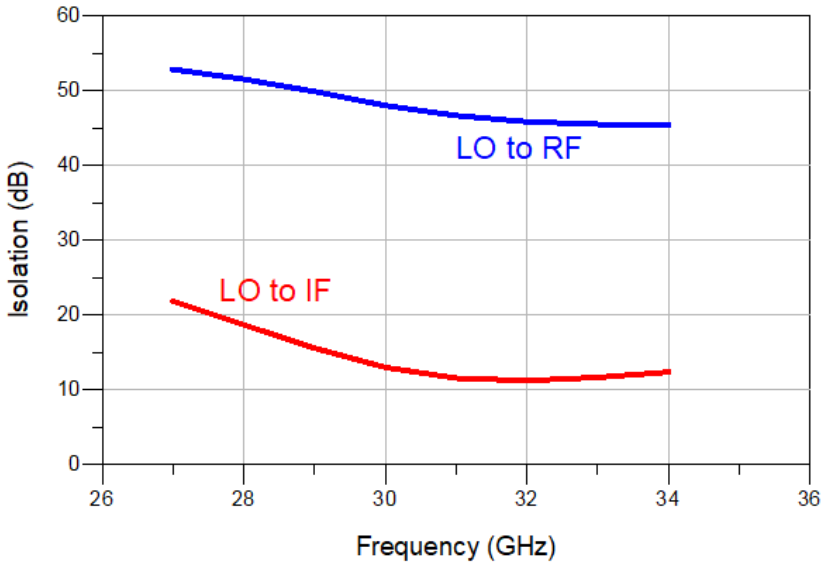

Figure 4.19. Simulated isolation of LO to IF and RF.

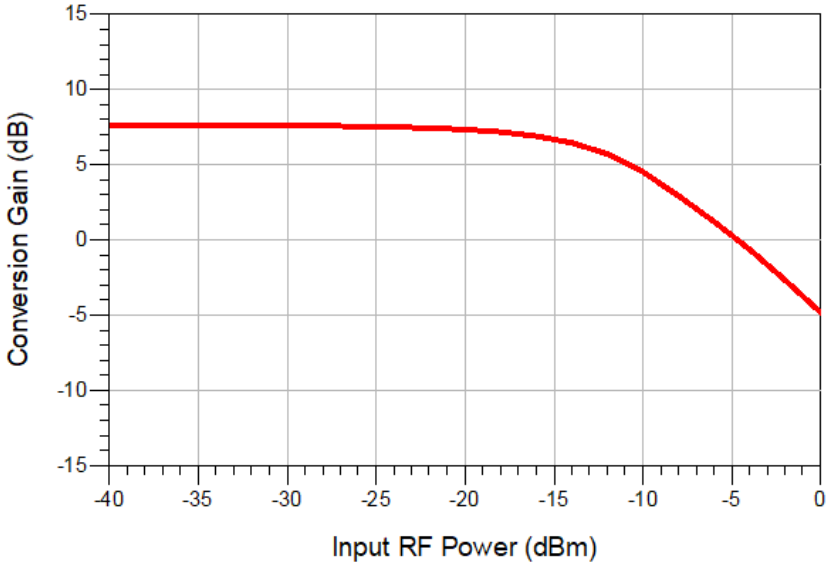

Figure 4.20. Conversion gain compression at f_{RF} =37 GHz and f_{LO} =27 GHz.

compression. Finally, Figure 4.21 shows the conversion gain dependence on the LO power. This shows how the down-converter delivers conversion gain with an LO power as low as -15 dBm. Fig. 4.22 shows the microphotograph of the fabricated chip with size of 0.8 x 1.2 mm^2.

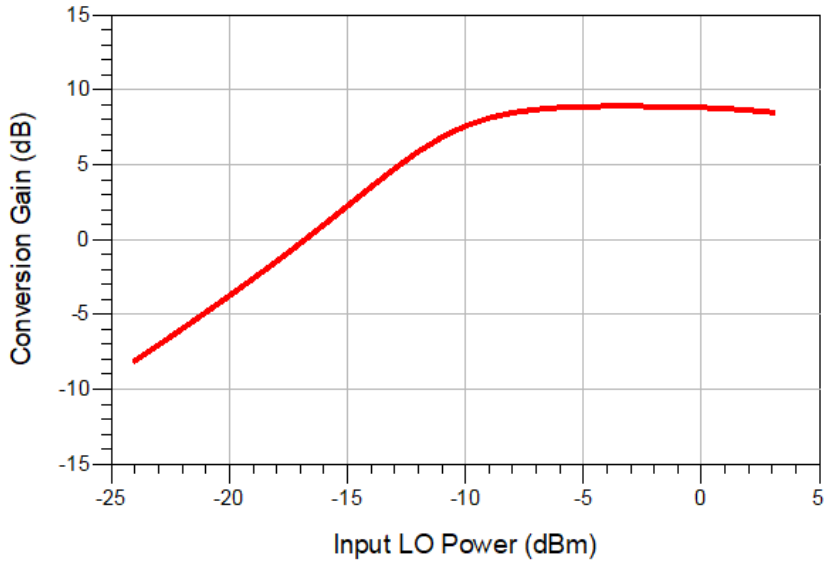

Figure 4.21. Conversion gain dependency on LO power at f_{RF}=37 GHz and f_{LO}=27 GHz.

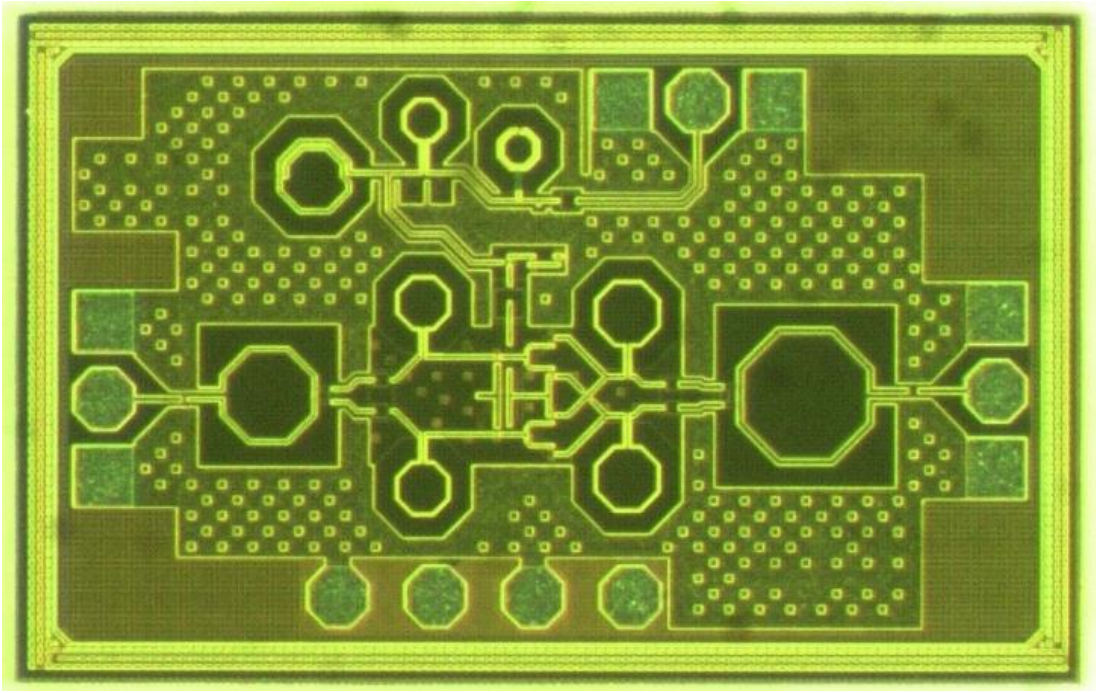

Figure 4.22. Microphotograph of the down-converter chip (size of 0.8 x 1.2 mm^2).

4.2.3 Measured Results

Figure 4.23 shows the measurement set up used to characterize the chip on an RF probe station. A Keysight PNA 5227B with frequency off-set and 4 ports was used to measure the *S*-parameters, conversion gain and isolations. Figure 4.24 shows the measured input reflection coefficient at three ports with a three-port SOLT calibration. All three ports have < -10 dB matching over the frequencies of interest. This shows a good agreement with simulation results depicted in Figure 4.16.

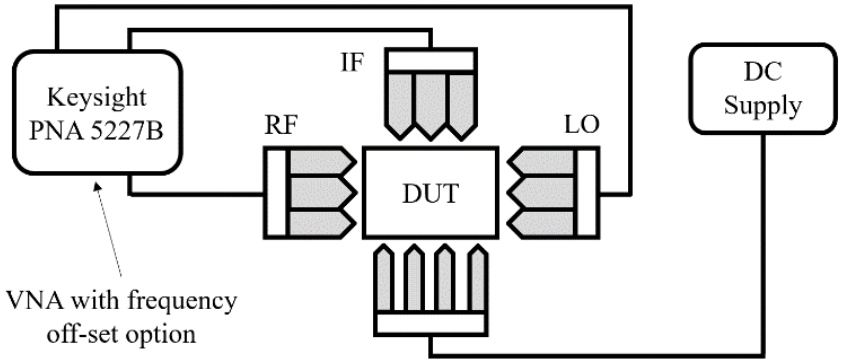

Figure 4.23. Measurement setup configuration using a 4-port VNA with frequency off-set option.

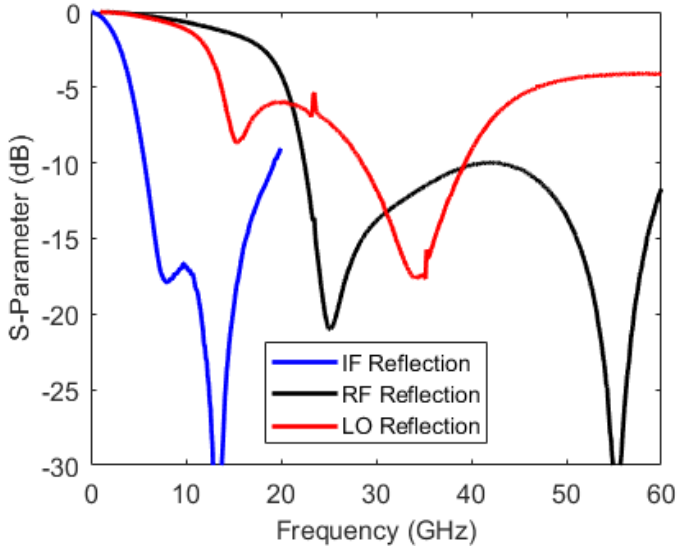

Figure 4.24. Measured input reflection of the down-converter ports.

Figure 4.25 shows the measured conversion gain of the mixer for two sub-band LO frequencies with an IF of 8-16 GHz under an LO power of -6 dBm and nominal RF power of -30 dBm. An 8 dB conversion gain was measured with 3 dB gain flatness in the 8-16 GHz IF range. Figure 4.26 shows a 4-8 dB conversion gain over the IF bandwidth of 6-18 GHz which is 4 GHz wider than the original design requirement. This corresponds to 33-52 GHz RF bandwidth.

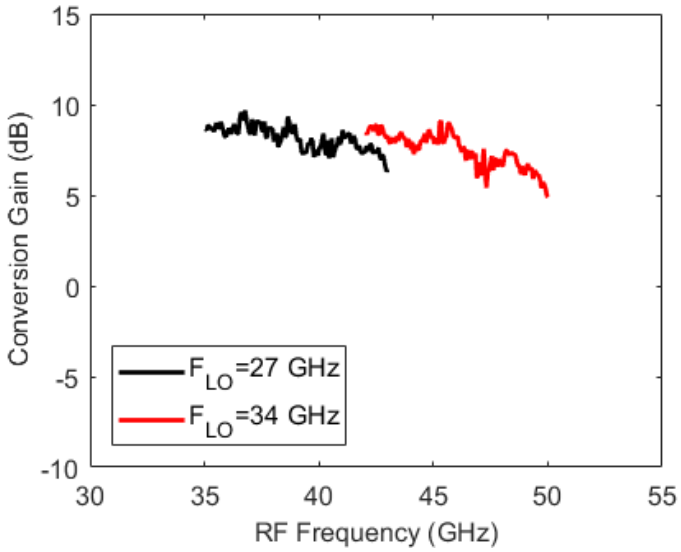

Figure 4.25. Measured down-converter conversion gain for two RF sub-bands with 8-16 GHz IF.

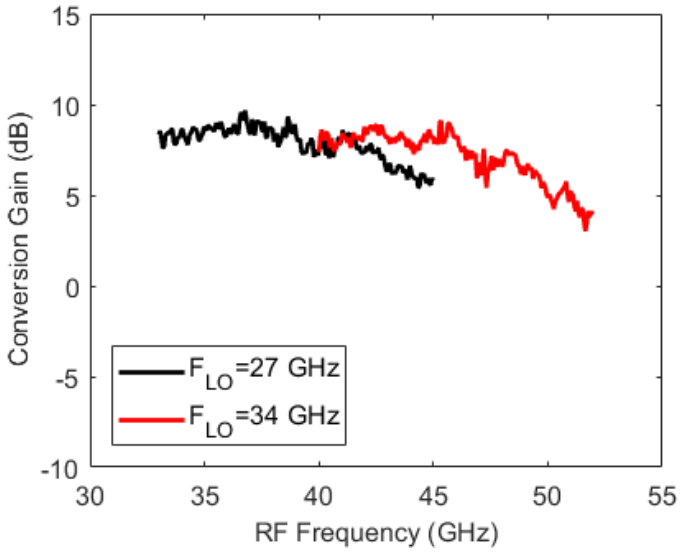

Figure 4.26. Measured down-converter conversion gain with a wide IF of 6-18 GHz.

Also, the RF frequency can be expanded from 35-50 GHz to 28-56 GHz if lower conversion gain is acceptable as shown in Figure 4.27. Figure 4.28 shows the measured isolation between the LO and other two ports. Note that the LO to IF leakage is less than -30 dB; a better performance compared to the -25 dB predicted from simulated results.

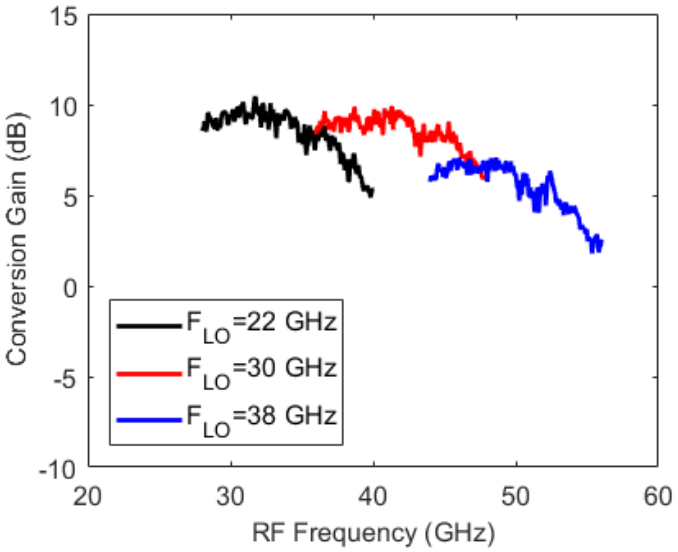

Figure 4.27. Measured down-converter conversion gain for a wideband RF of 28-56 GHz.

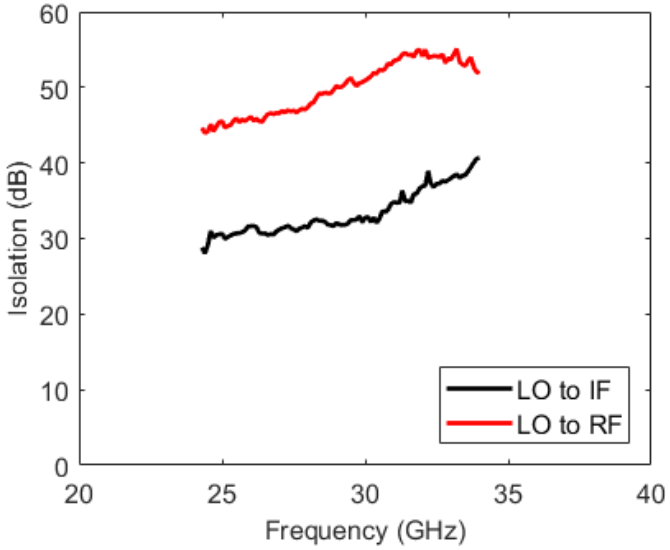

Figure 4.28. Measured isolation of the down-converter from LO to IF and RF.

Figure 4.29 demonstrates that the RF leakage to IF isolation is higher than 40 dB. And the RF to LO isolation is better than 30 dB over most of the bandwidth. For the conversion gain compression test, the LO frequency was set at 30 GHz with -6 dBm power, and the RF power of a 48-GHz signal was swept. Figure 4.30 shows the conversion gain change with respect to RF input power. It depicts the IF output power as a function of the input RF power. The 1dB compression point occurs at -14 dBm input power and corresponds to a -10 dBm output swing.

Figure 4.31 shows the conversion gain dependency on the level of the pumping LO signal for LO and RF signals set at 30 GHz and 42 GHz, respectively. This shows that the down-converter is able to provide conversion "gain" with the LO power as low as -12 dBm which greatly relaxes the LO generation and distribution requirements regarding the circuit complexity, component count and power consumption. We can see that choosing the LO power at around -5 dBm would minimize the gain variation due to LO power level fluctuation while providing 10 dB gain.

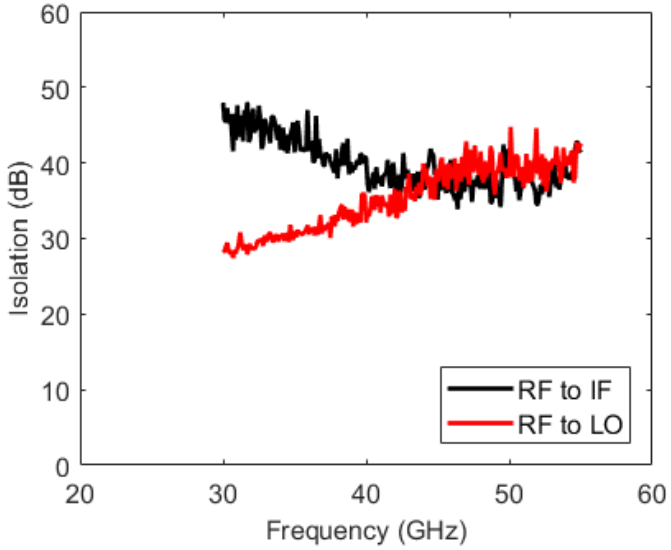

Figure 4.29. Measured down-converter RF to IF and LO isolation.

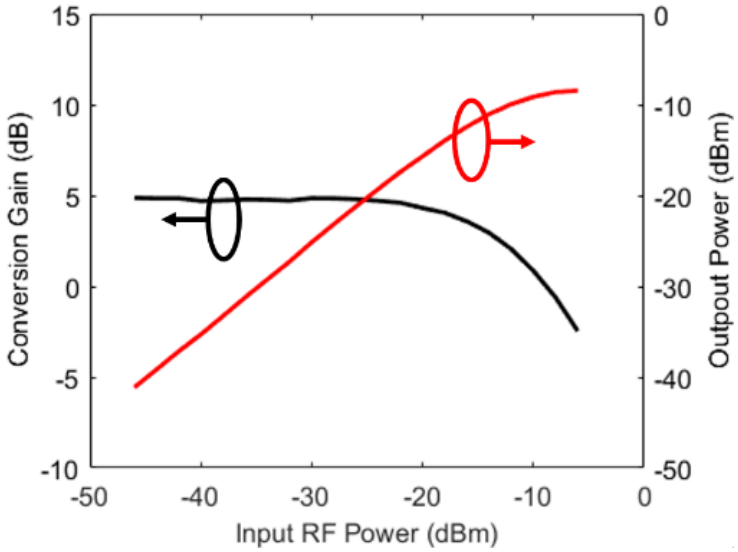

Figure 4.30. Down-converter conversion gain compression and output power; measured at f_{RF} = 48 GHz, f_{LO} = 30 GHz, LO power = -6 dBm.

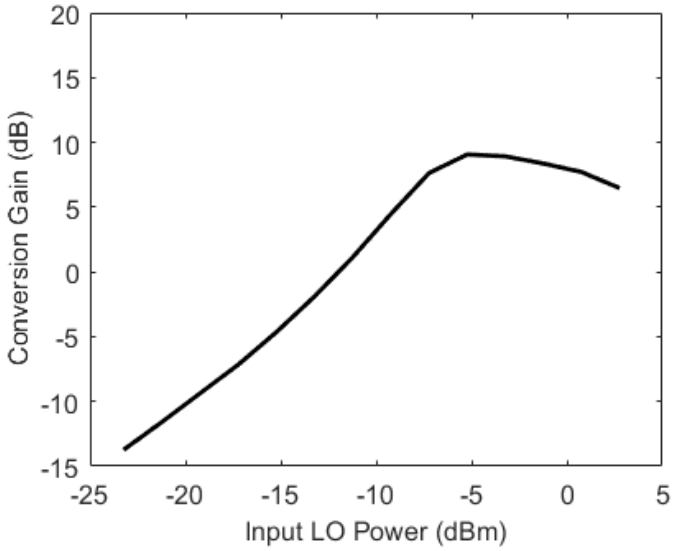

Figure 4.31. Down-converter conversion gain dependence on LO power; measured at f_{RF} = 42 GHz, f_{LO} = 30 GHz, RF power = -30 dBm.

Table 4.2. Summary of published Q-band mixer performances.

Ref.	Technology	RF Freq. (GHz)	IF Freq. (GHz)	CG (dB)	LO/RF ISO (dB)	LO/IF ISO (dB)	LO Power (dBm)	Size (mm2)	Power (mW)
[121]	GaAs pHEMT	32-52	2-12	4-7	38	35	4	2	N.A.
[122]	180 nm SiGe	50-067	0.5-8.5	13	N.A	N.A	3	0.146	66
[123]	90 nm CMOS	30-90	DC-20	-7.5	> 30	N.A	2.5	0.389	0.6
[114]	150 nm GaAs pHEMT	34-53	3-13	-2	> 37	> 21	0	2.25	36
This Work	SiGe	35-50 28-56	8-16 6-18	5-8 3-8	> 42	> 30	-6	0.96	80

Table 4.2 summarizes the down converter performance in comparison with published mixers for radio astronomy applications in similar frequency bands. This work demonstrates high conversion gain, high LO-to-RF and LO-to-IF isolation, and the lowest LO power requirement.

The fabricated chip demonstrates a measured single-ended conversion gain of 5-8 dB with less than 3 dB variation and a low LO power of -6 dBm over the IF bandwidth of 8-16 GHz as the LO frequency range varies from 27 to 34 GHz, meeting the primary design goals. Furthermore, the test results show a wider RF frequency performance of 28-56 GHz with 3-8 dB conversion gain in the IF bandwidth of 6-18 GHz with the LO frequency of 22 to 38 GHz at an LO power of -5 dBm.

A measured LO-to-RF isolation greater than 40 dB is achieved in addition to wideband RF port matching to 50 Ω, allowing to directly connect the down-converter to the post amplifier without the need of an isolator.

The entire down-converter chip consumes 80 mW power in a small size of 0.96 mm^2 including pads and chip streets which is considerably smaller even when compared to stand-alone mixers [118] [120]. The low LO drive power and DC power consumption of the mixer makes it potentially integratable with a SiGe-based post-LNA (warm amplifier) operating at room temperature to further decrease the receiver size of the telescope's frontend.

4.3 GaAs pHEMT Mixer for 33-55 GHz

Although Gilbert cell mixers are superior when it comes to isolation and conversion gain, they have a complex topology which requires a BEOL that offers multiple interconnect metals. On the other hand, III-V technologies usually employ two layers of metallization which is more suitable for simpler circuit topologies.

Figure 4.32 shows the chip block diagram, and Table 4.3 presents the mixer design requirements. This mixer is designed with the inspiration of ALMA radio telescope Band 1 that operates at 30-50 GHz with an IF frequency of 4-12 GHz.

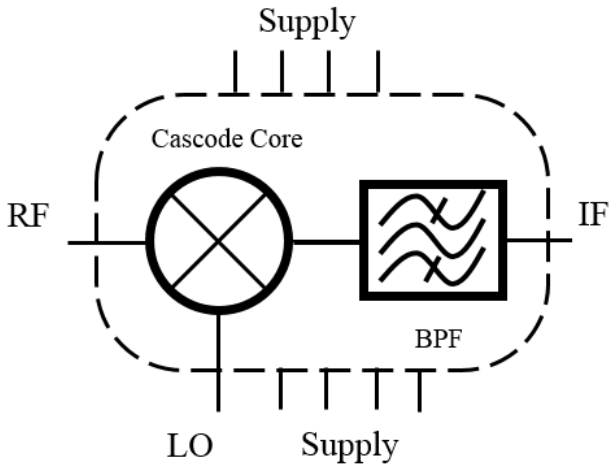

Figure 4.32. 30-55 GHz down-converter block diagram.

Table 4.3. 30-50 GHz mixer design goals.

Conversion Gain (dB)	> -6
Conversion Gain flatness (dB)	2
LO driving power (dBm)	0
RF frequency (GHz)	33-55
LO frequency (GHz)	29-39
IF frequency (GHz)	4-16
RF port return loss (dB)	< -10
LO port return loss (dB)	< -10
IF port return loss (dB)	< -10
LO to IF Isolation	> 30
LO to RF Isolation	> 30
RF to IF Isolation	> 30
Input 1-dB gain compression point (dBm)	> -10

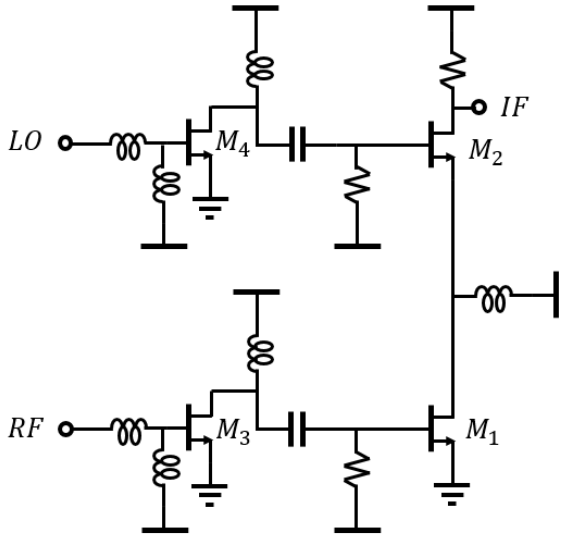

(a)

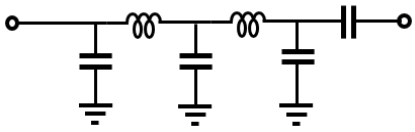

(b)

Figure 4.33. (a) Improved cascode mixer core, (b) bandpass filter.

4.3.1 Mixer Design

The proposed work is designed to cover wider RF and IF bandwidths of 33-55 GHz and 4-16 GHz, respectively.

Single ended cascode configurations can be easily realized in GaAs technology. However, to overcome the cascode limitations while benefiting from simple architecture with lower power consumption, an improved design is proposed as shown in Figure 4.33 (a).

This design employs a cascode core using M_1 and M_2 where M_3 and M_4 are used for input RF and LO matching allowing the cascode core to be separately optimized for the highest conversion gain. This allows to achieve a wideband performance for both conversion gain and input matching. M_3 and M_4 amplify signals requiring lower LO power considering the fact that standalone GaAs cascode cores require 0-4 dBm LO power to achieve conversion gain of about 0 dB [124].

Moreover, M_3 and M_4 provide an extra 10-20 dB isolation between the LO and RF.

One of the main limitations of the traditional cascode is the shared bias current between the upper and lower transistor. However, adding a shunt inductor (or a quarter wavelength short stub) allows the DC current of the upper transistor to be different from the common source device while the AC current is still common between the two (necessary for cascode mixer operation). Taking advantage of this technique allows M_2 to be biased at V_{gs} close to its pinch-off for best switching performance when the LO signal is applied while consuming no DC power. Finally, to resolve the LO and RF leakage to IF, a band pass filter, shown in Figure 4.33 (b), is placed at the IF port to suppress the unwanted mixing produced and to provide the matching to the 50 Ω at the IF port.

Figure 4.34 shows the final layout of the mixer after DRC that was submitted to the WIN Foundry. The devices in the LO path are 2×40 μm and RF devices are 2×25 μm. Figure 4.35 shows the simulated reflection of the three ports which is below -10 dB for all parts over the frequencies of interest. The conversion gain of the mixer, shown in Figure 4.36, is -5-0 dB over the entire RF band. The isolation of the mixer for LO to IF and RF and RF to IF and LO is presented in Figure 4.37 and 4.38, respectively.

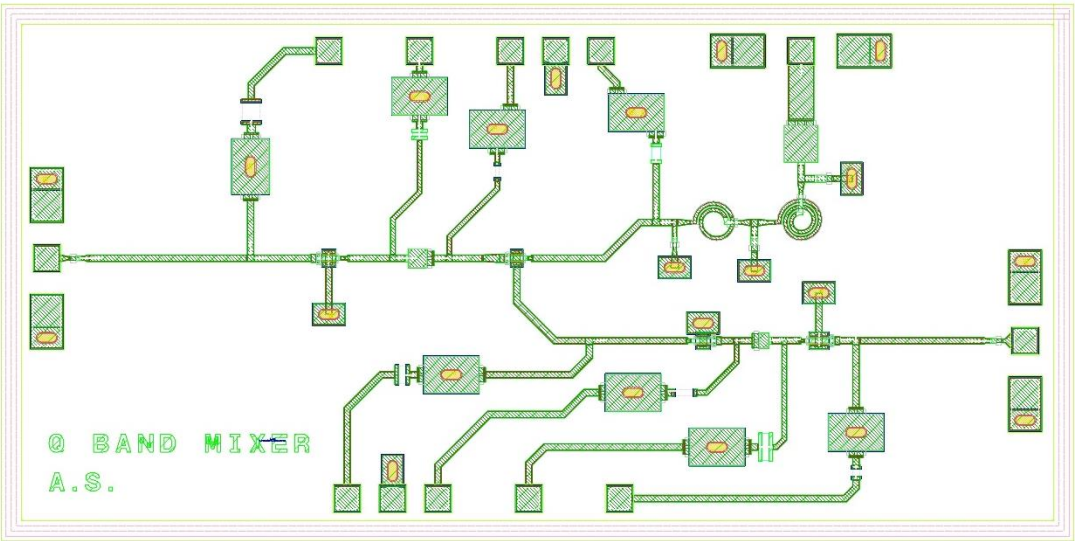

Figure 4.34. Layout of the mixer chip.

The conversion gain compression is a good criterion for linearity of the mixer that is shown in Figure 4.39. The mixer has a -8 dBm input compression at -4.5 dB conversion gain. Finally, Figure 4.40 shows the conversion gain dependence on the LO power.

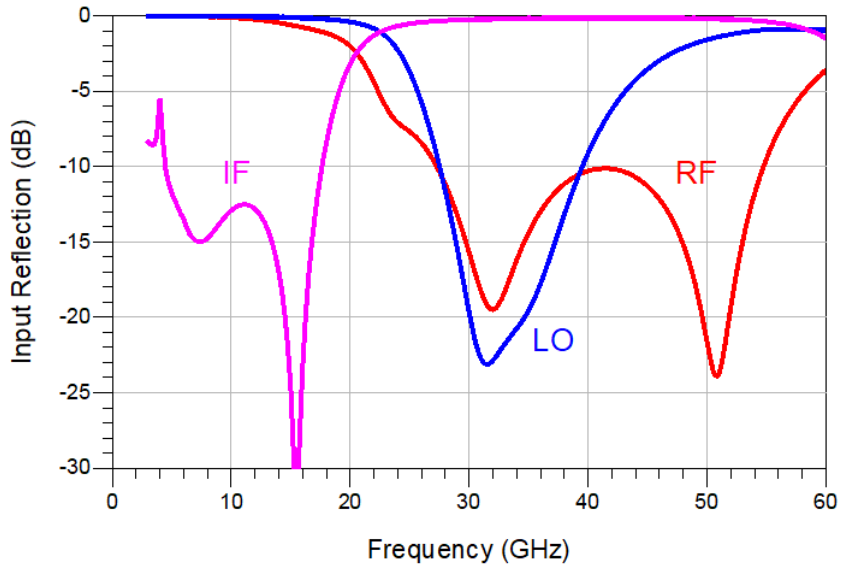

Figure 4.35. Simulated input reflection of the mixer.

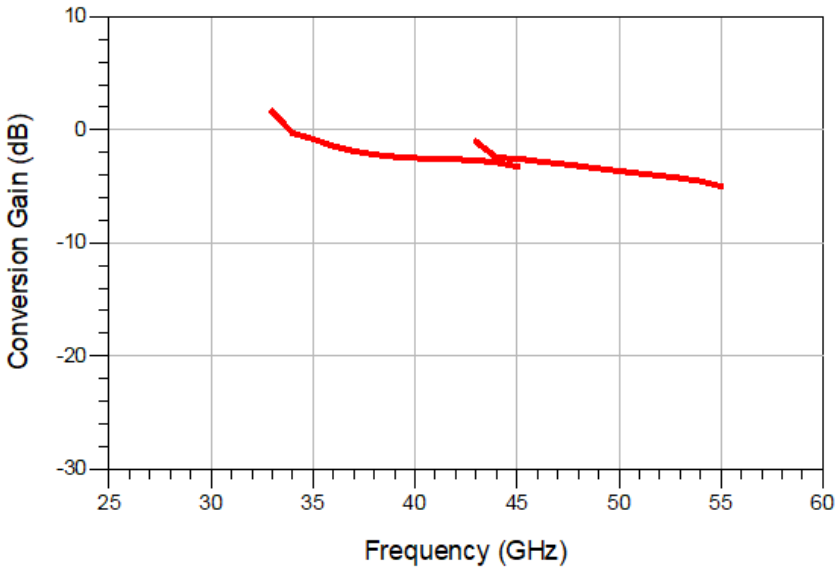

Figure 4.36. Simulated conversion gain for upper two RF sub-bands.

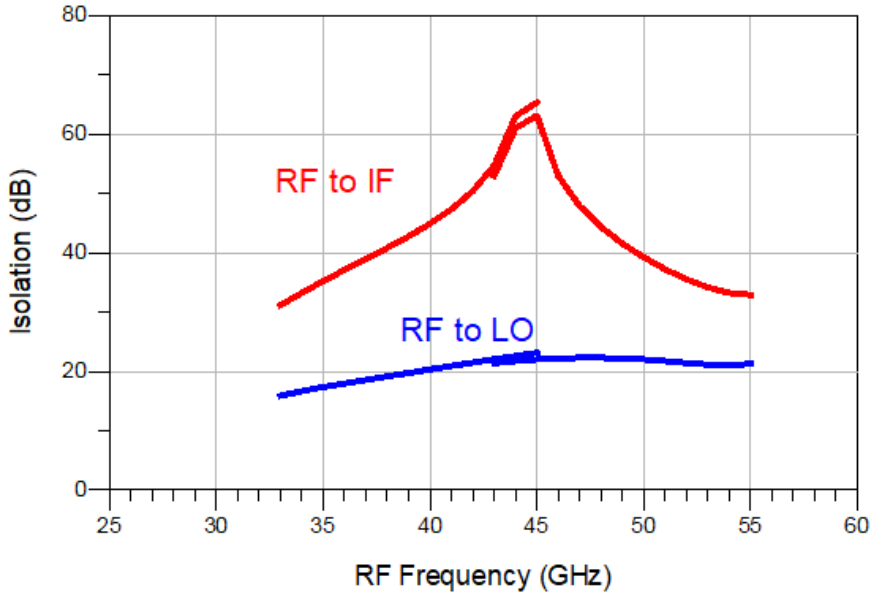

Figure 4.37. Simulated isolation of RF to IF and LO.

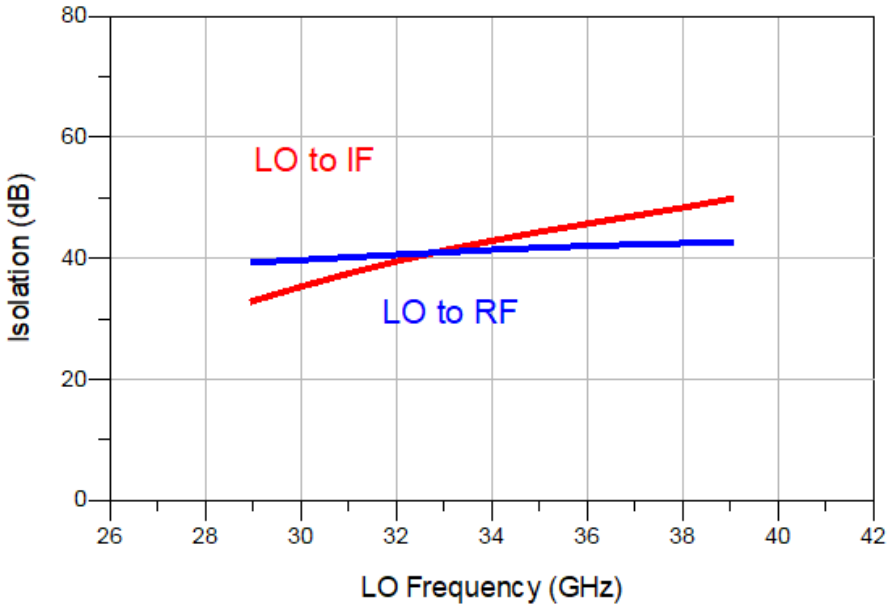

Figure 4.38. Simulated isolation of LO to IF and RF.

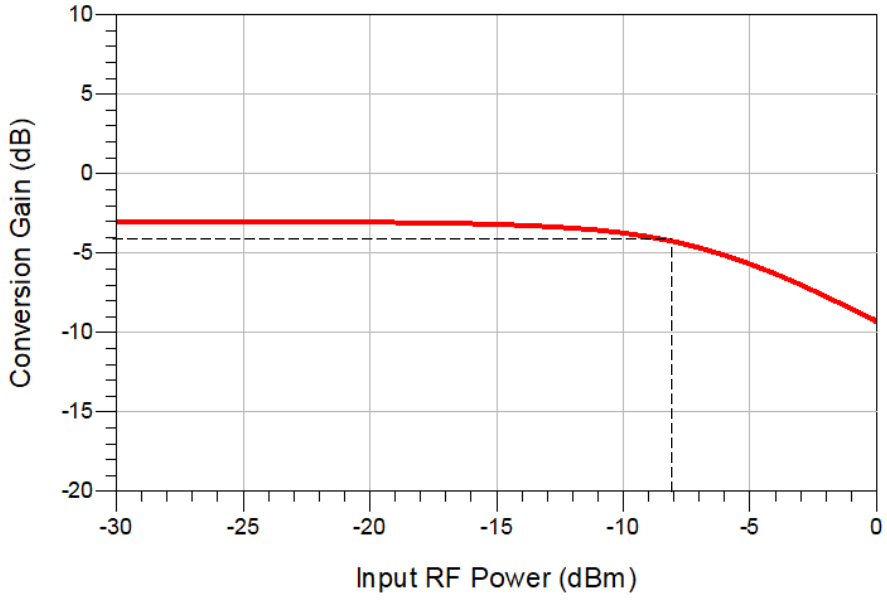

Figure 4.39. Conversion gain compression at f_{RF} = 45 GHz and f_{LO} = 33 GHz.

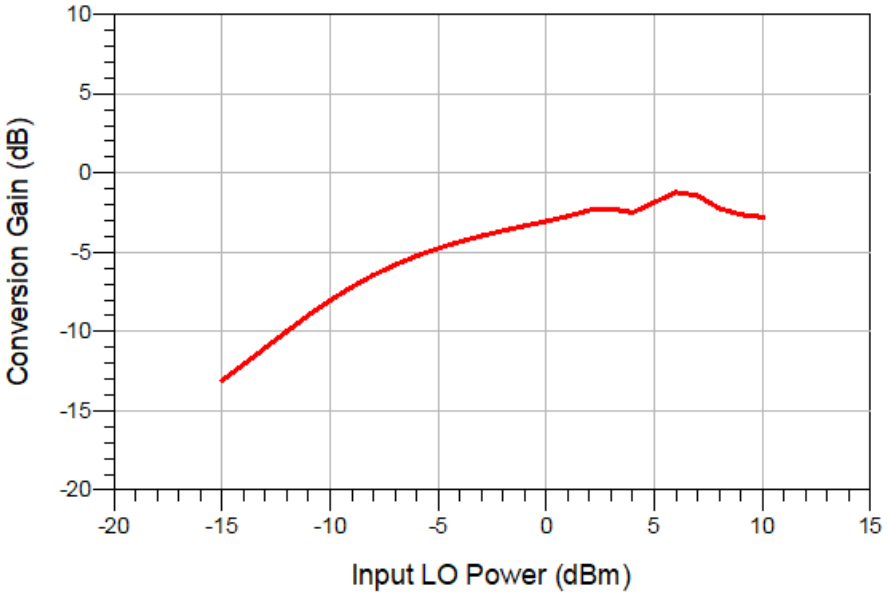

Figure 4.40. Conversion gain dependency on LO power at f_{RF} = 45 GHz and f_{LO} = 33 GHz.

4.3.2 Measured Results

Figure 4.41 shows a microphotograph of the fabricated chip. The chip was assembled in a custom designed coaxial chassis as shown Figure 4.42. The chassis provides RF, LO, IF and DC signals to the chip. The width and height of the chambers are kept minimized to prevent waveguide modes from excitation while small openings allow to wire bond the chip to off-chip components. A Keysight PNA 5227B with frequency off-set option and three ports was used to measure the *S*-parameters, conversion gain and isolations. Figure 4.43 shows the measured input reflection coefficient at three ports with a three-port SOLT calibration. All three ports have < -10 dB matching over the frequencies of interest. Figure 4.44 shows the measured conversion gain of the mixer for the sub-band with an IF of 4-16 GHz under an LO power of -3 dBm and nominal RF range of 33-55 GHz with power of -30 dBm. A 1-dB conversion gain was measured with 3 dB gain flatness in the 4-16 GHz IF range. The measured conversion gain is about 1-2 dB higher than the values predicted by simulations shown in Figure 4.36.

The chip however is able to provide wider IF bandwidth of 0.5-20 GHz if the gain flatness requirement is relaxed to 6 dB. This corresponds to 30-60 GHz RF bandwidth.

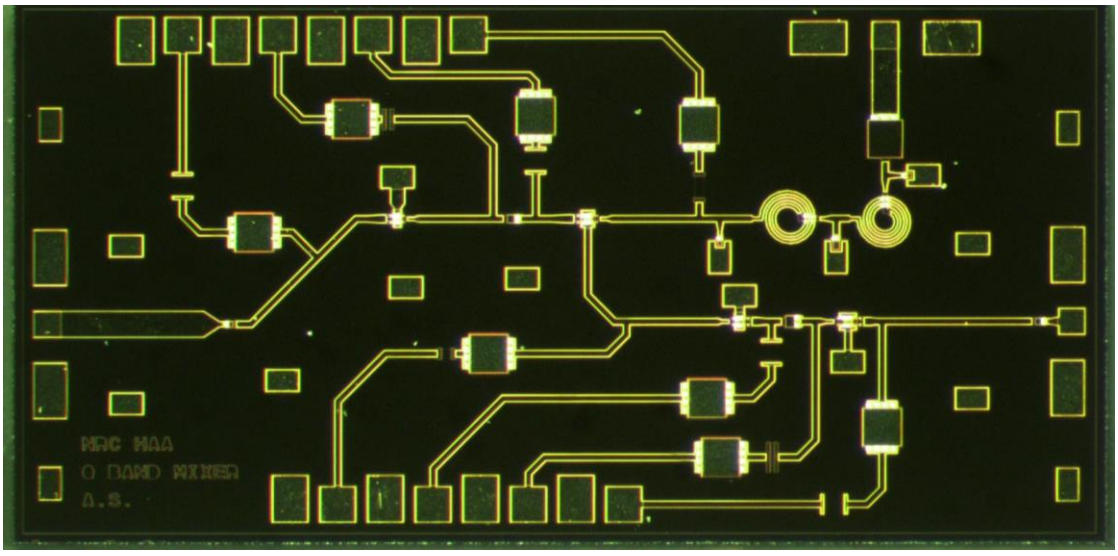

Figure 4.41. Microphotograph of the down-converter chip (size of 1.5 x 3 mm^2).

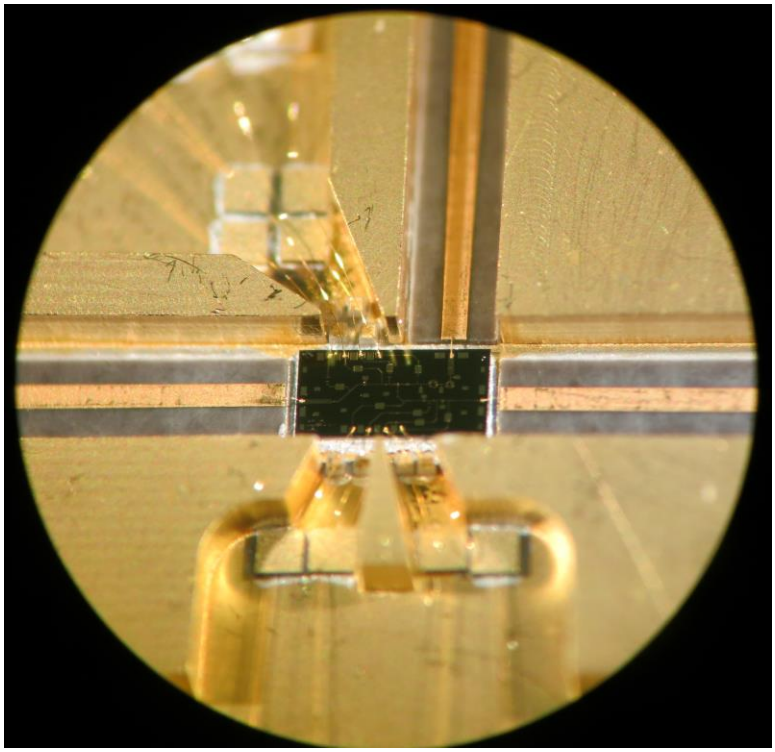

(a)

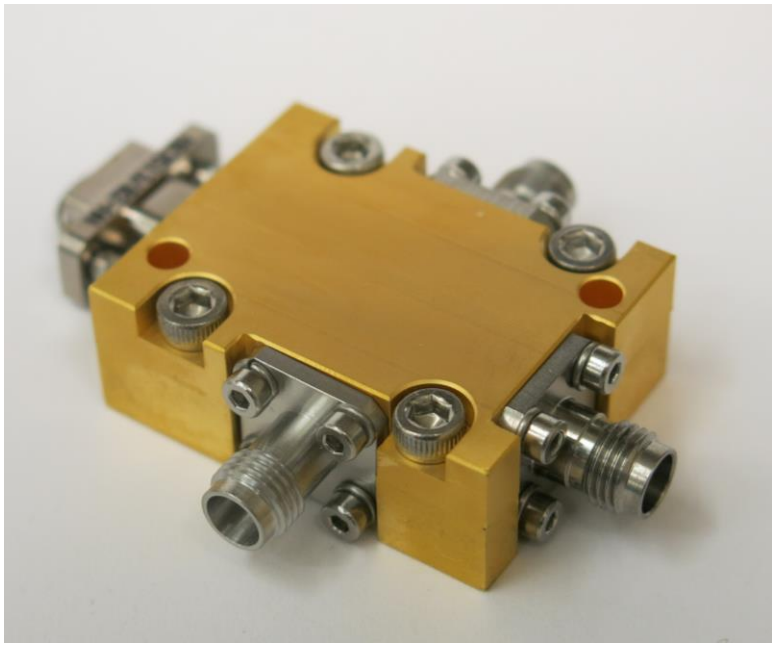

(b)

Figure 4.42. (a) Assembled chip in (b) the custom designed chassis.

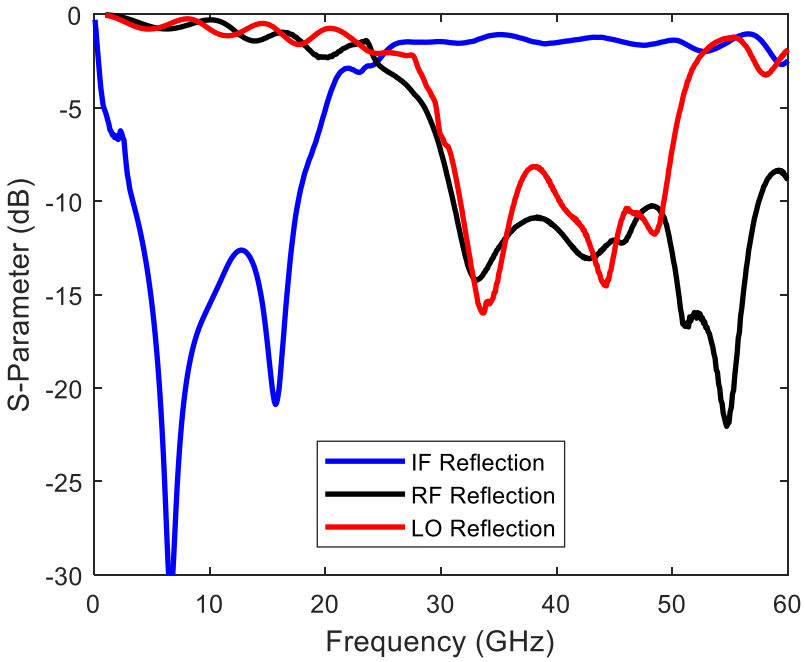

Figure 4.43. Measured input reflection of the mixer.

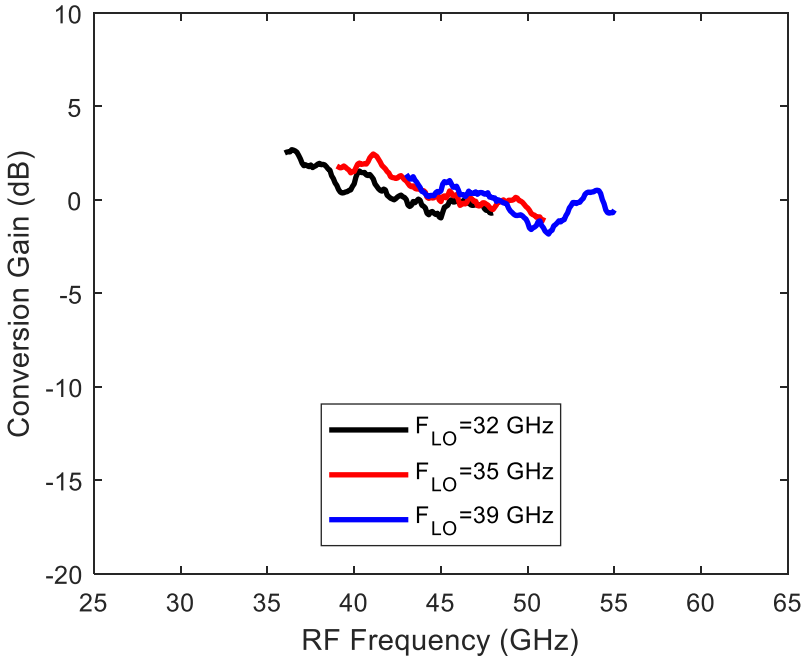

Figure 4.44. Measured conversion gain for upper two RF sub-bands.

Figure 4.45 shows the measured isolation between the LO and other two ports which is better than 35 dB for IF and better than 40 dB for the RF. Figure 4.46 shows the RF leakage to LO and IF port where leakage to IF is about 30 dB; however, the leakage to LO is as low as 20 dB. This is caused by the unbalanced configuration and was predicted in simulations. Note that the RF to LO leakage is not as critical as that of LO to RF in radio telescopes.

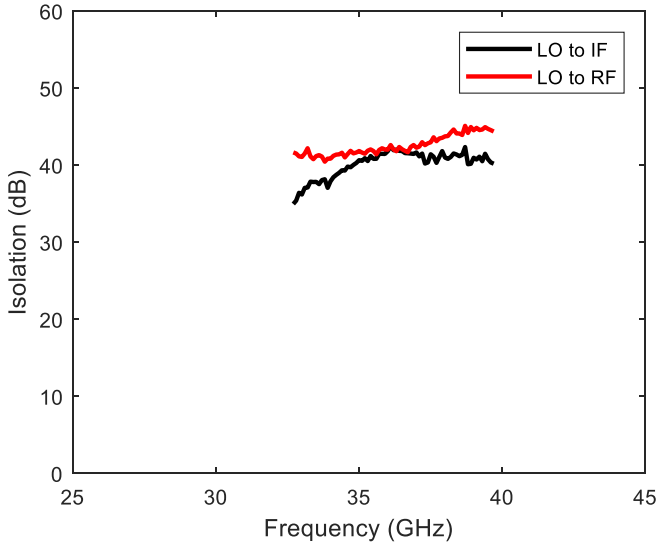

Figure 4.45. Measured isolation of LO to IF and RF.

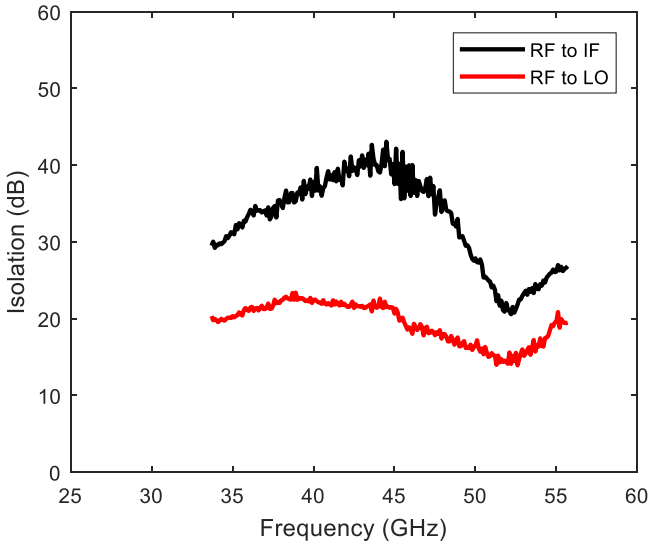

Figure 4.46. Measured isolation of RF to IF and LO.

Figure 4.47 shows the conversion gain change with respect to RF input power. It depicts the IF output power as a function of the input RF power. The 1dB compression point occurs at about -10 dBm input power and corresponds to a -11 dBm output swing. Taking into account the higher conversion gain seen in the measurements, this is in agreement with a simulated input 1-dB compression point around -10 dBm. Figure 4.48 shows the conversion gain dependency on the level of the pumping LO signal for LO and RF signals set at 30 GHz and 40 GHz, respectively.

Table 4.4 summarizes the down converter performance in comparison with published mixers for radio astronomy applications in similar frequency bands. This work demonstrates a good conversion gain, high LO-to-RF and LO-to-IF isolation.

The fabricated chip demonstrates a measured single-ended conversion gain of 1 dB with less than 3 dB variation and a low LO power of -3 dBm over the IF bandwidth of 4-16 GHz as the LO frequency range varies from 29 to 39 GHz, meeting design goals. A measured LO-to-RF isolation greater than 40 dB is achieved in addition to wideband RF port matching to 50 Ω, allowing to directly connect the down-converter to the post amplifier without the need of an isolator. The entire down-converter chip consumes 90 mW of power with the size of 4.5 mm^2.

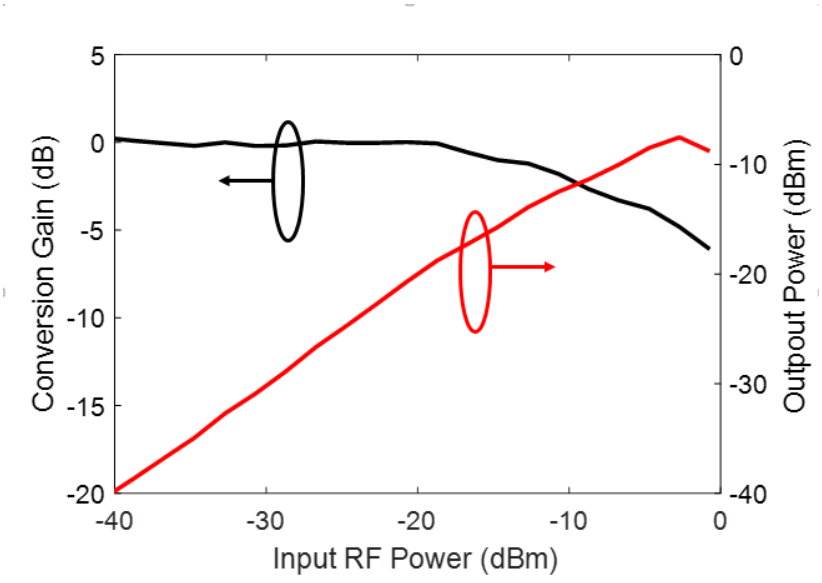

Figure 4.47. Conversion gain compression at f_{RF} = 40 GHz and f_{LO} = 30 GHz.

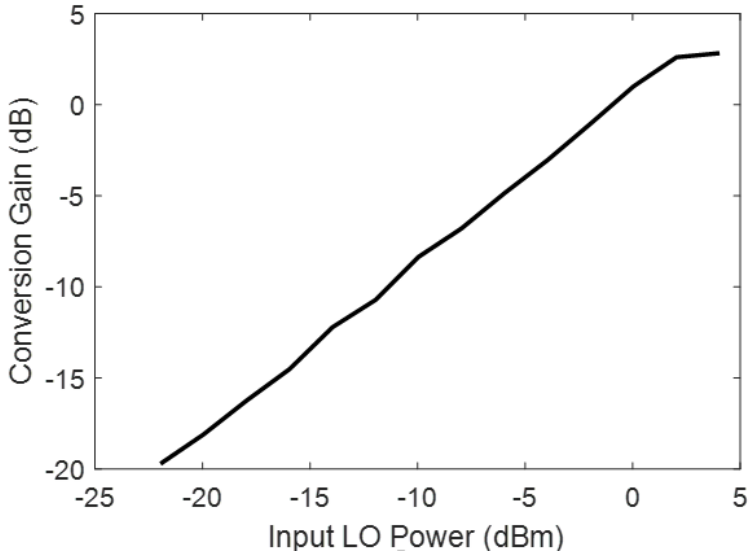

Figure 4.48. Conversion gain dependency on LO power at f_{RF} = 40 GHz and f_{LO} = 30 GHz.

Table 4.4. Summary of published Q-band mixer performances.

Ref.	Technology	RF Freq. (GHz)	IF Freq. (GHz)	CG (dB)	LO/RF ISO (dB)	LO/IF ISO (dB)	LO Power (dBm)	Size (mm2)	Power (mW)
[121]	GaAs pHEMT	32-52	2-12	4-7	38	35	4	2	N.A.
[124]	GaAs pHEMT	27-47	0-15	0	N.A	23	4	1.8	N.A
[114]	150 nm GaAs pHEMT	34-53	3-13	-2	> 37	> 21	0	2.25	36
[125]	150 nm GaAs pHEMT	32-52	2-12	4	> 37	> 35	4	2	N.A
This Work	150 nm GaAs pHEMT	33-55 30-60	4-16 0.5-20	1 -2-4	> 40	> 35	-3	4.5	90

4.4 SiGe BiCMOS Mixer for 70-120 GHz

As pointed out before, ngVLA will utilize a direct conversion architecture with a wide baseband of 0-7 GHz in which the RF signals at bands 2-6 are down converted to the desired baseband (BB) for sampling. The millimeter bands (5 and 6) need a wideband down converter that supports the entire RF bandwidth. In the particular case of Band 6, there are

very few commercial components available that cover the broad 50 GHz bandwidth of 70-120 GHz. And, in a case of an I/Q downconverter with acceptable conversion gain, good I/Q mismatch, high isolation and wide low return loss, the choices are even more limited if there are any at all. Therefore, a wideband mm-wave I/Q mixer is proposed to address all the requirements and challenges of the ngVLA radio telescope. This requires an elaborate design that inevitably expands beyond a single component development, and considering the small size of passives at such a high frequency, many components can be integrated with the mixer cores and BB buffers to achieve the system requirements. Figure 4.49 demonstrates the architecture of the proposed 70-120 GHz down-converter chip.

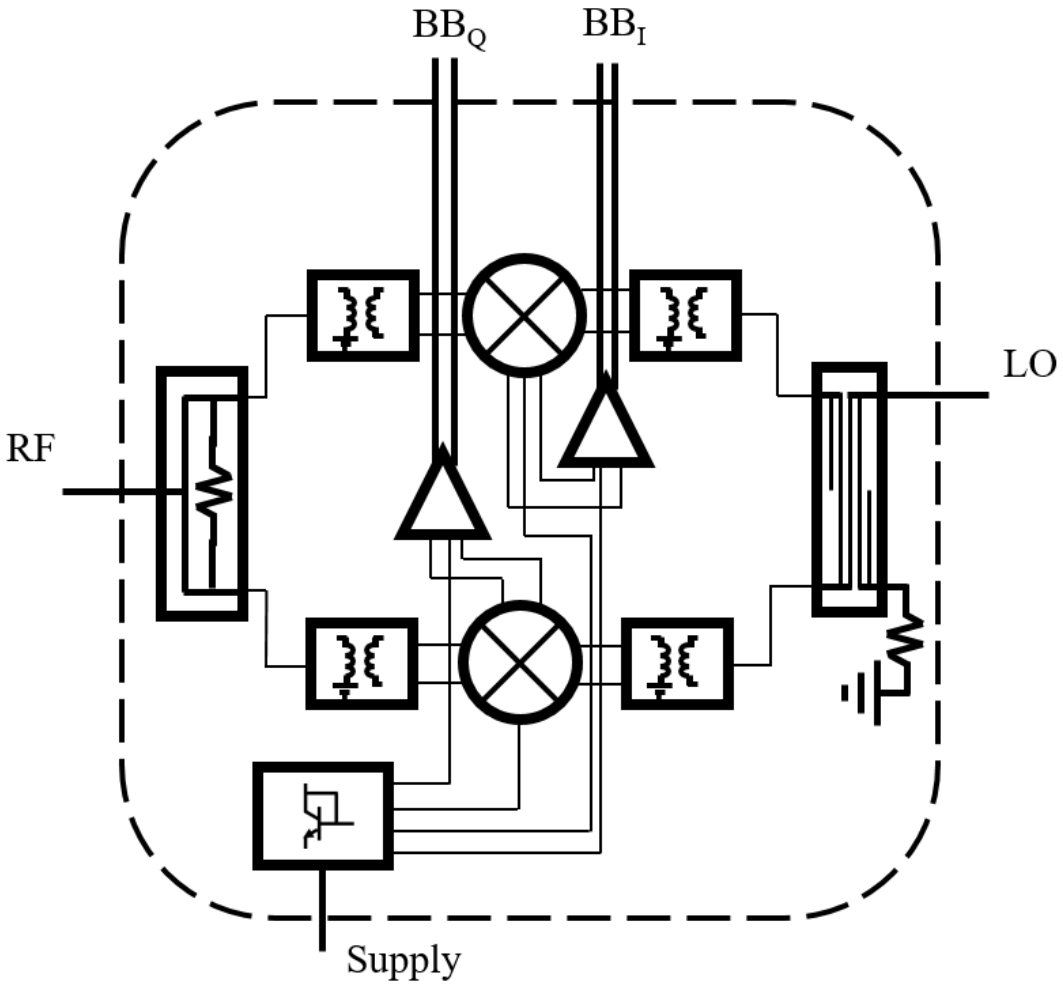

Figure 4.49. 70-120 GHz down-converter block diagram.

Table 4.5. 70-120 GHz down-converter design goals.

Conversion Gain (dB)	>3
Conversion Gain flatness (dB)	1.5
LO driving power (dBm)	-6
RF frequency (GHz)	70-120
LO frequency (GHz)	70-110
BB frequency (GHz)	0-8
RF port return loss (dB)	<-10
LO port return loss (dB)	<-10
BB port return loss (dB)	<-10
LO to BB Isolation	>30
LO to RF Isolation	>30
RF to BB Isolation	>30
IQ amplitude mismatch (dB)	± 0.5
IQ phase mismatch (degree)	± 5
Input 1-dB gain compression point (dBm)	>-8

It consists of two double balanced mixer cores, one Wilkinson power divider, a Lange coupler, four transformer baluns and two IF buffers. The input RF signal is split in half using a wideband Wilkinson power divider that generates two in-phase RF signals and a Lange coupler that divides the LO signal with a 90° phase difference. In an alternative architecture, the RF signal is fed to the Lange coupler and the LO to the Wilkinson divider. The reason to choose a Wilkinson divider over a Lange coupler for the RF signal is its broadband amplitude and phase match over the entire frequency of interest. On the other hand, the LO signal has a narrower bandwidth that results in a relatively constant gain and phase mismatch over frequency caused by the Lange coupler.

Before being fed to the mixer cores, single-ended RF and LO signals are converted to differential ones using wideband baluns. The double balanced Gilbert Cell configuration is chosen to improve the isolation of LO-to-RF and LO-to-BB. Finally, baseband buffers are placed between mixer outputs and chip pads to prevent loading as well as providing output matching with proper drive capability. The output signals are not DC decoupled on-chip due to chip size concerns. However, proper off-chip capacitors can be utilized based on baseband (backend) design and low frequency components. Table 4.5 summarizes the design goals for the proposed down converter.

4.4.1 Design

Using a standard 3.3-V power supply and 8 mA current for each mixing core, the switching quads and transconductor pairs are sized for maximum speed and low noise current density, respectively. As shown in Figure 4.50, a peaking inductor is added in series with the load resistor to preserve the conversion gain when the IF frequency increases. The differential outputs are DC coupled to buffer amplifiers to prevent the loading of the mixing core.

Each mixing core requires an in-phase RF signal that is achieved using a Wilkinson power divider considering the reasonable size at 90 GHz center frequency shown in Figure 4.51. The divider provides wideband power split with good phase and amplitude balance. Figure 4.52 shows the S-parameters and amplitude/phase mismatch. The overall loss of the divider is about 0.5 dB over the bandwidth of interest with better than ± 0.1 dB amplitude and ± 1° phase imbalance.

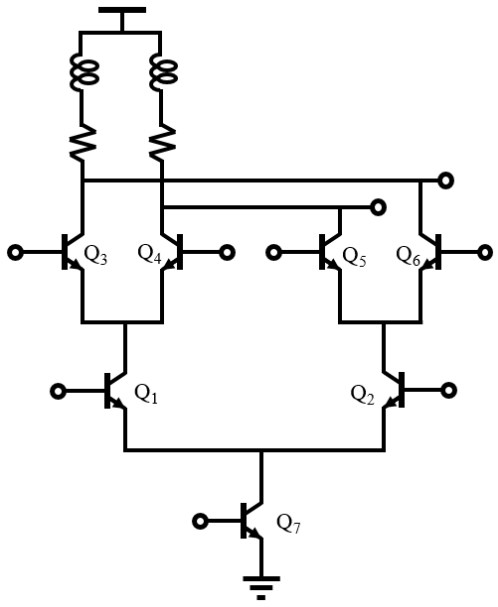

Figure 4.50. Simplified mixer core schematics.

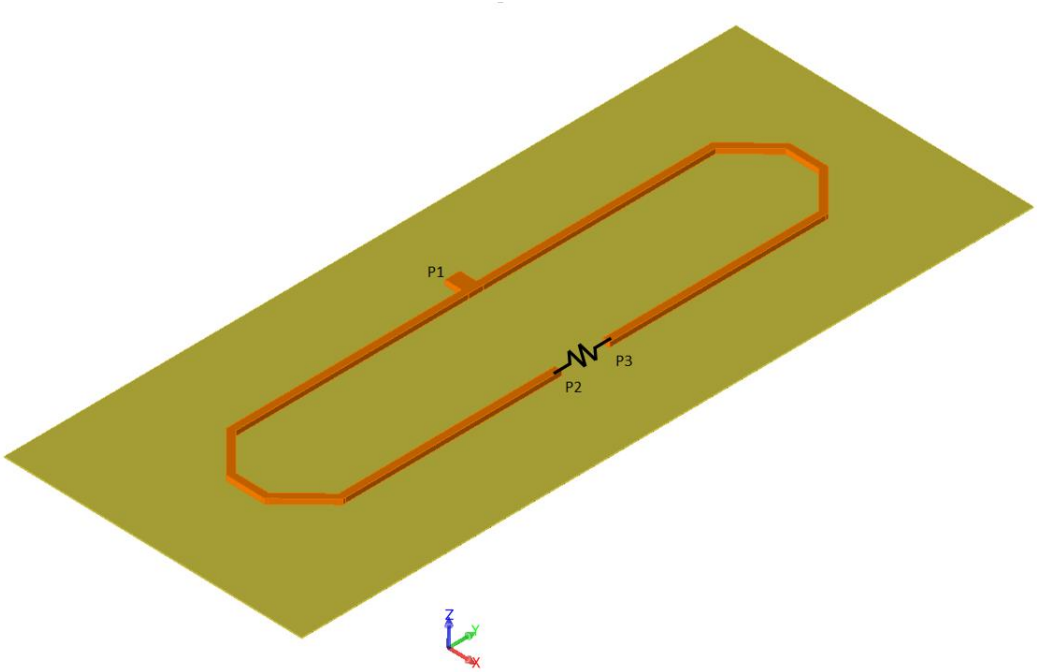

Figure 4.51. Wilkinson power divider EM model. The resistance is not EM simulated and is added to the circuit as a lumped element.

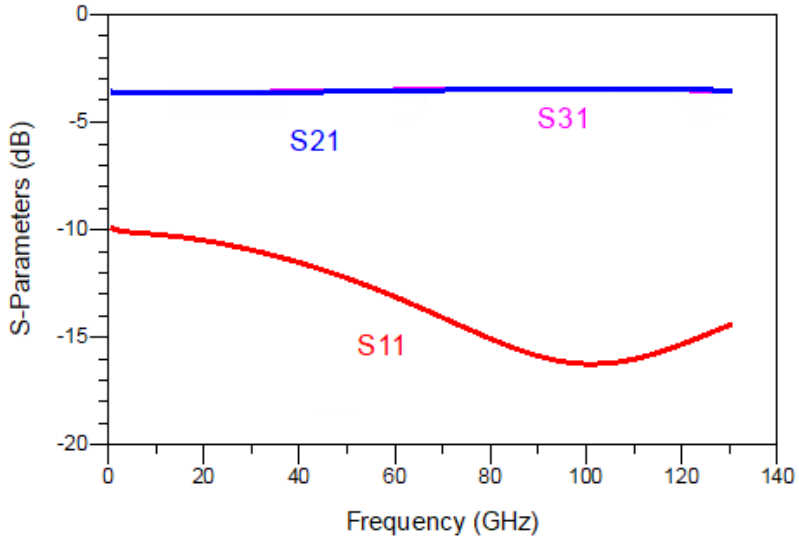

(a)

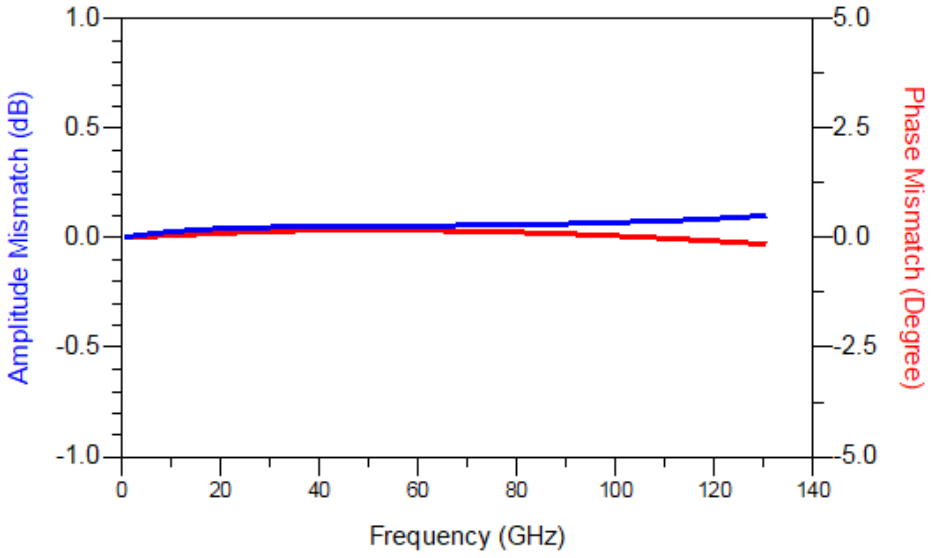

(b)

Figure 4.52. Wilkinson power divider (a) S-parameters (b) amplitude and phase imbalance.

The I and Q mixing cores need LO signals that are 90° out of phase. The Lange coupler that is designed using the most upper layer metal for this purpose is shown in Figure 4.53. Lange coupler offers a wide bandwidth; however, EM simulations show that the optimum results are realized with trace spacing less than the minimum value allowed by the technology. Figure 4.54 (a) shows the EM simulation results of the structure that is compatible with process fabrication rules with the minimum metal spacing of than 3 μm. The coupler provides ± 0.2 dB amplitude and ± 3.5° phase imbalance over the 70-120 GHz range as presented in Figure 4.54 (b). The overall loss of the coupler is around 0.7 dB across the band.

Finally, two transformer baluns were designed to translate the single ended RF and LO signals to differential for each mixing core.

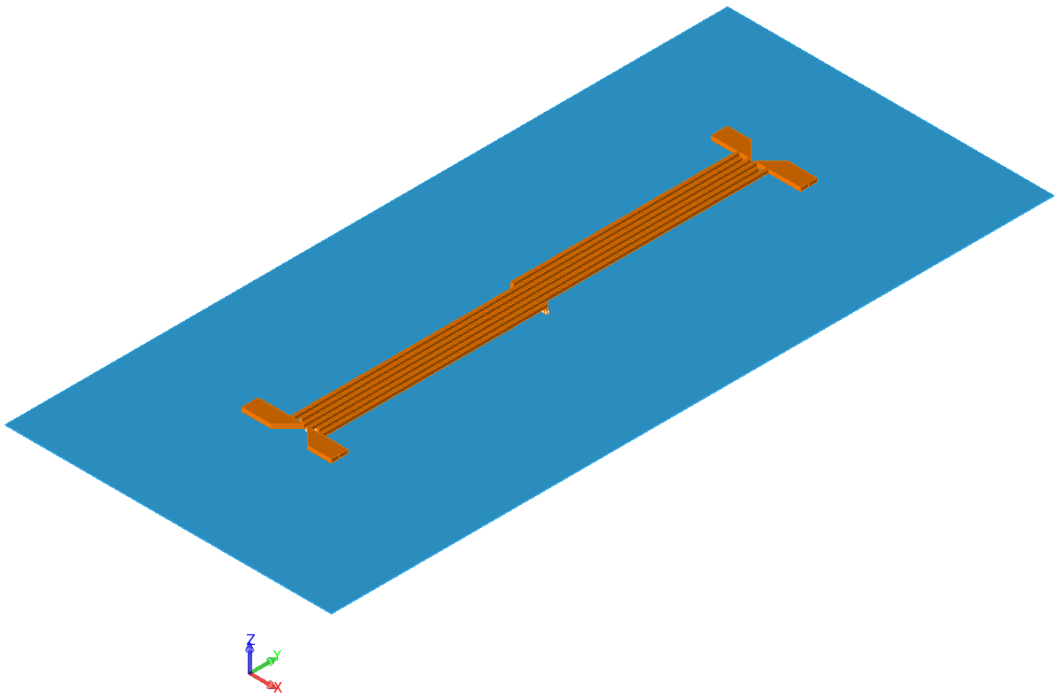

Figure 4.53. Lange coupler EM model.

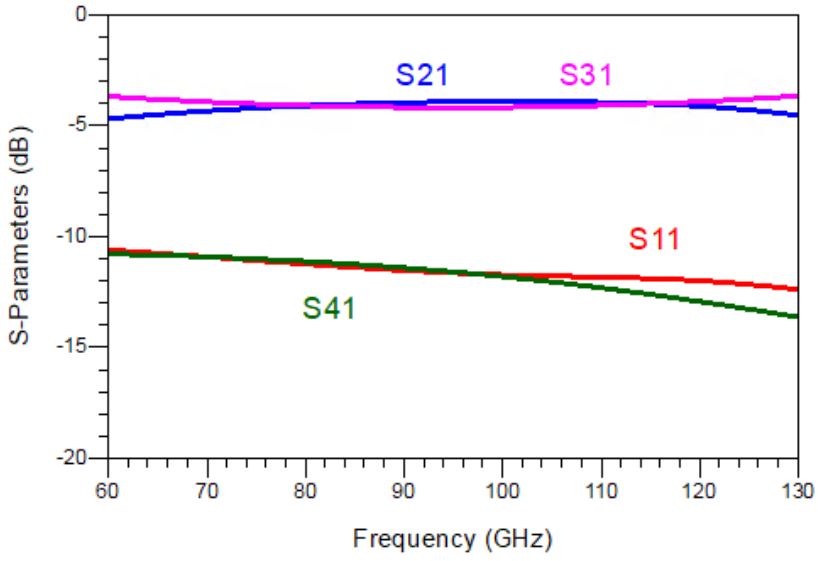

(a)

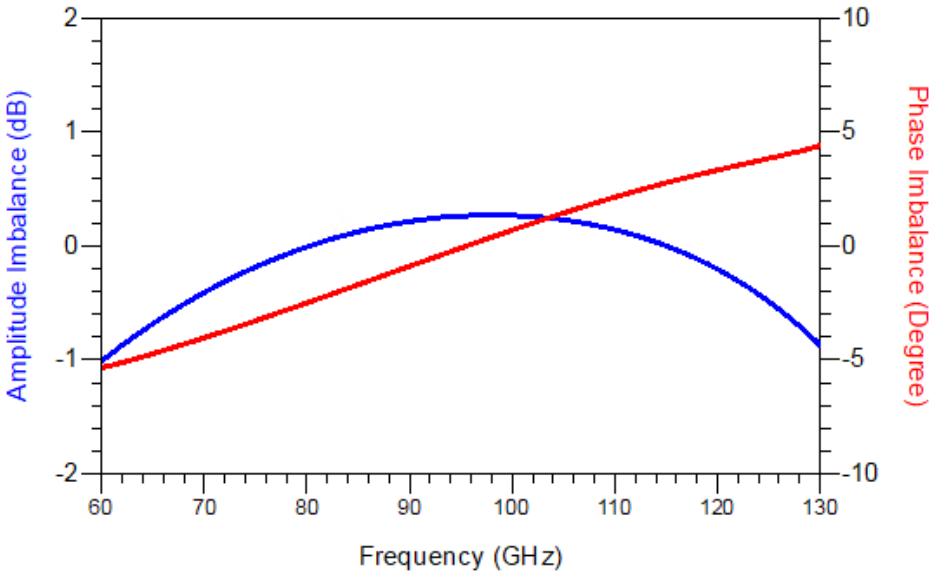

(b)

Figure 4.54. Lange coupler (a) S-parameters (b) amplitude and phase imbalance.

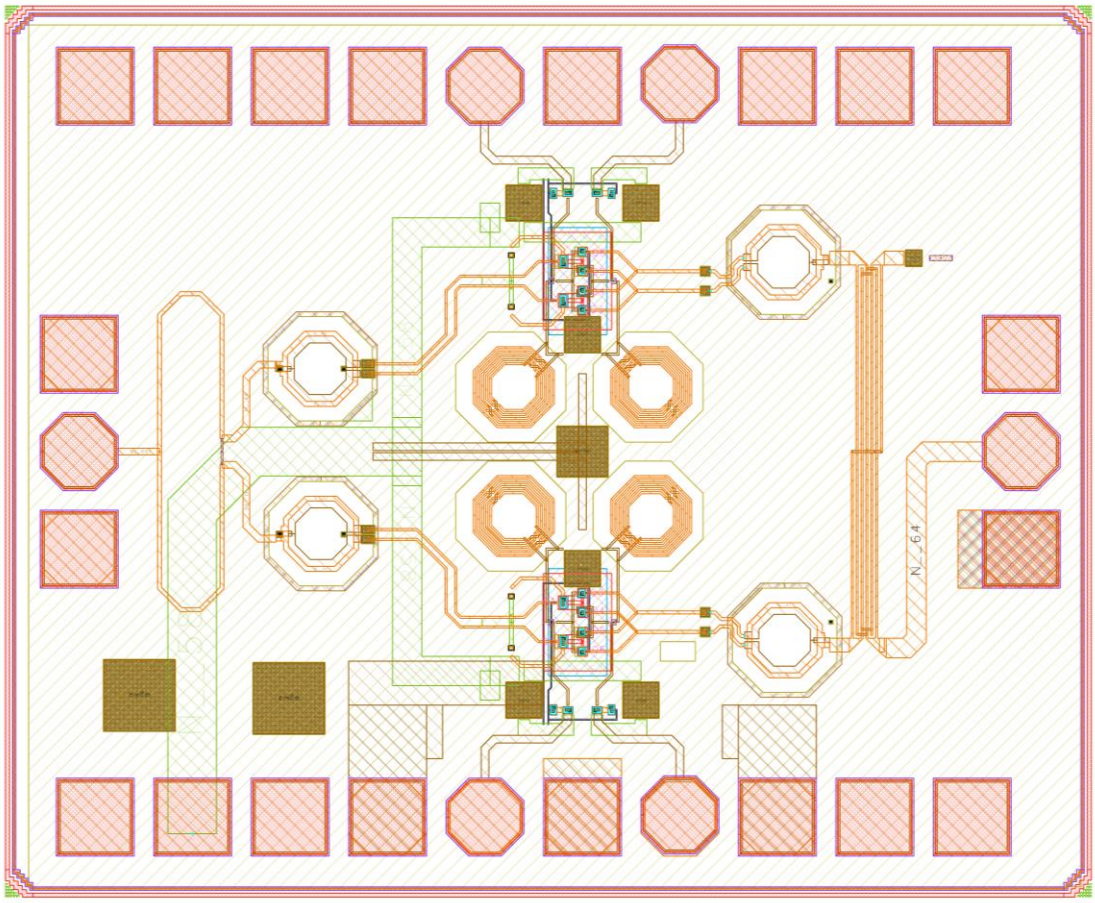

Figure 4.55. Current layout of the 70-120 GHz down-converter chip.

Figure 4.55 shows the current chip layout with a size of 0.8×1 mm^2. This chip is in the EM simulation phase at the time of submission of this theses and it is being prepared for tape out in the next few months. Figure 4.56 and Figure 4.57 show the simulated input (LO/RF) and output (BB) return loss for the down-converter chip, respectively.

The conversion gain for I and Q paths are shown in Figure 4.58. This shows about 3-8 dB conversion gain for the entire RF bandwidth with 1.5 dB gain flatness for individual RF sub-bands. Figure 4.59 shows the mismatch between I and Q outputs. The estimation of IQ mismatches over the entire band is $\pm$ 0.5 dB in amplitude and $\pm$ 5° for the phase. The

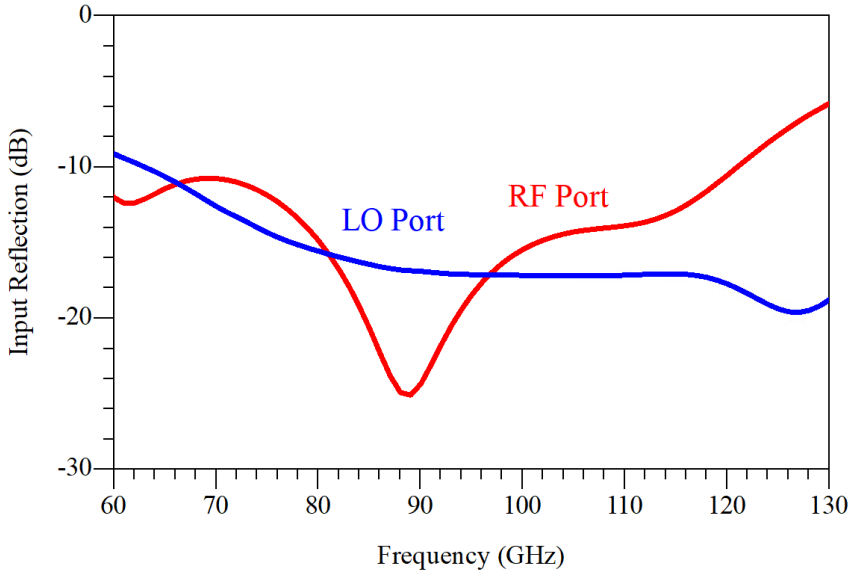

Figure 4.56. Simulated input reflection at RF and LO ports.

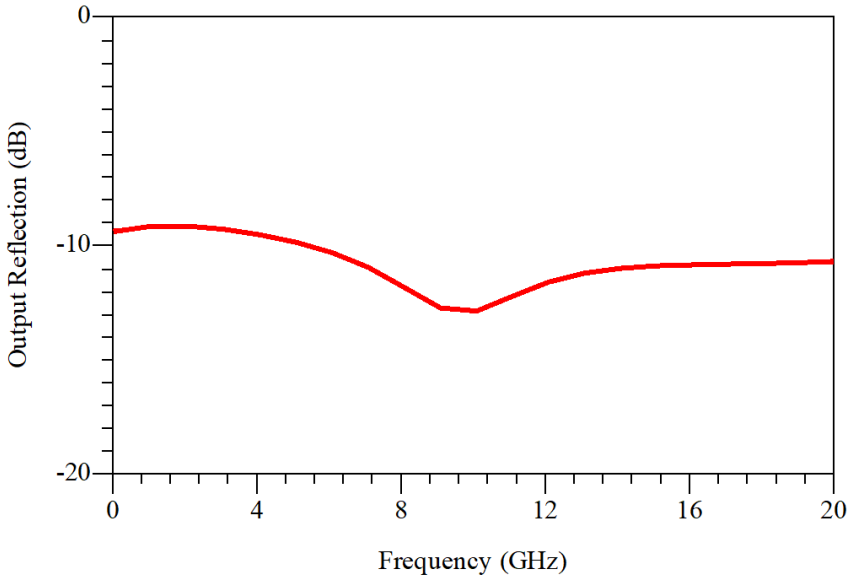

Figure 4.57. Simulated output reflection at the BB port.

mismatch is almost constant over frequency for each sub-band; therefore, it can be easily accounted for in the back end.

Figure 4.60 presents the isolation between LO and RF/BB for the mixer at different RF sub-bands. Better than 30 dB isolation is achieved without using any low pass filter.

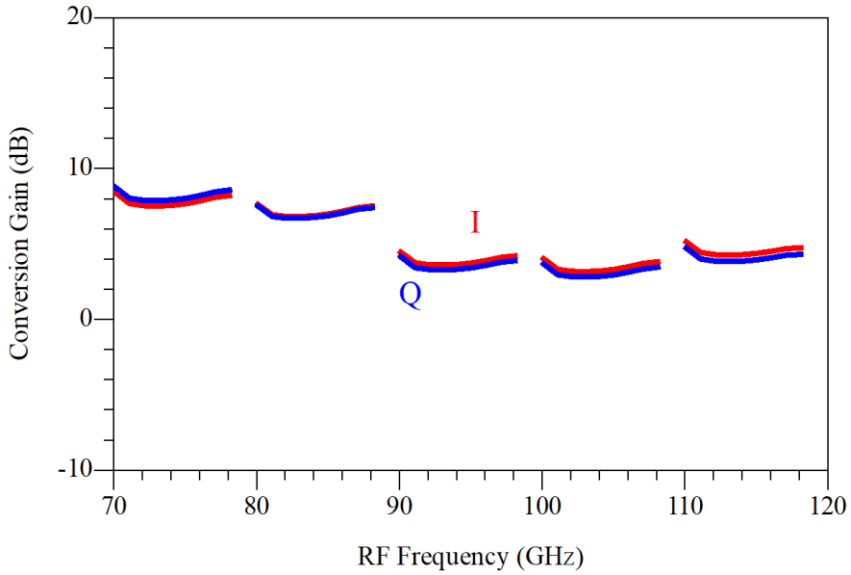

Figure 4.58. Simulated conversion gain for 8-GHz RF sub-bands (at 70, 80, 90, 100, 110 GHz).

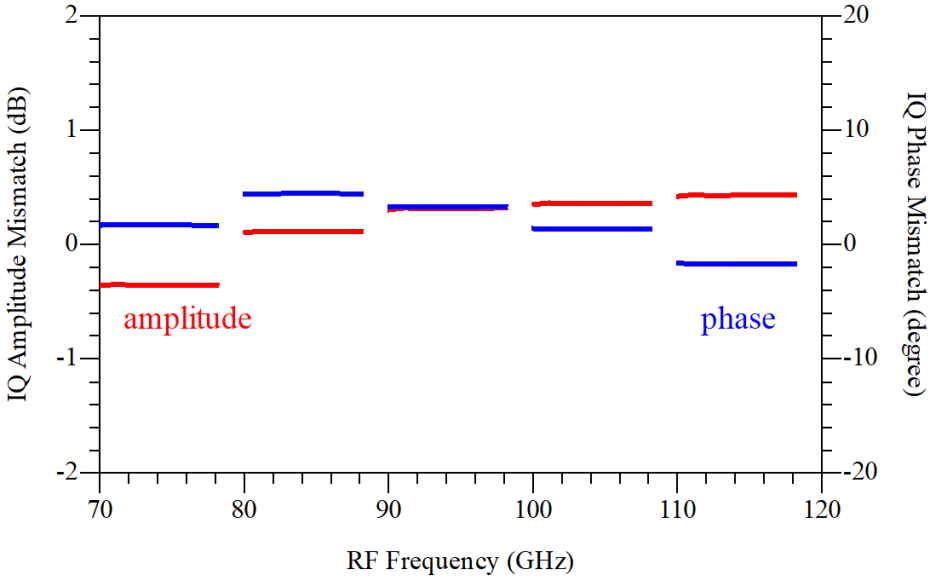

Figure 4.59. Simulated amplitude and phase mismatch between I and Q outputs for 8-GHz RF sub-bands (at 70, 80, 90, 100, 110 GHz).

As shown in Figure 4.61, the 1-dB point is at about -6 dBm at 95 GHz and -9 dBm at 70 GHz. However, the corresponding output 1-dB compression point for both is at -8 dBm.

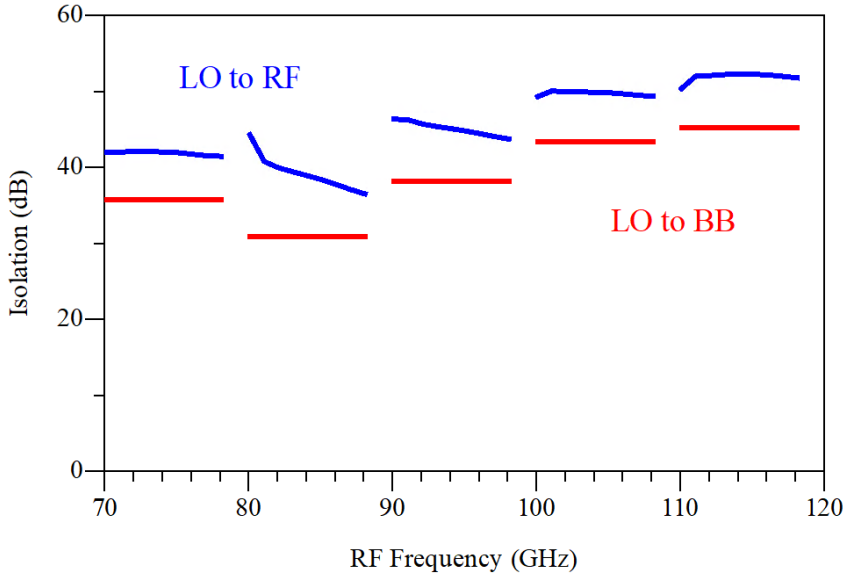

Figure 4.60. Isolation between LO and RF/BB for 8-GHz RF sub-bands (at 70, 80, 90, 100, 110 GHz).

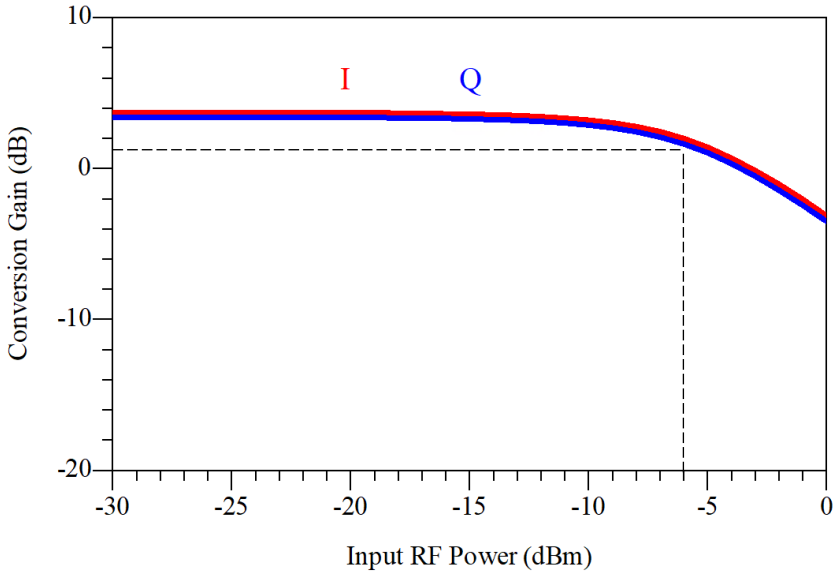

Figure 4.61. Conversion gain saturation at f_{RF} = 95 GHz, f_{LO} = 90 GHz.

Chapter 5

Discussion and Future Work

In this research we presented the semiconductor technologies and design methodologies of MMIC and RFIC development for radio telescopes. Four LNAs and three mm-wave down-converter mixers were introduced at various frequency bands in the 300 MHz to 120 GHz range targeting two upcoming radio telescopes: ngVLA and CHORD. The former covers a broad frequency range of 1-116 GHz focusing on cosmology and the latter is a broadband low frequency instrument to study fast radio bursts. Each proposed design is an effort to address the various challenges of radio astronomy.

From four low noise amplifiers, the UHF (300 MHz - 1.5 GHz) and Q-Band (30-52 GHz) LNAs were successfully measured. The Ku (12-24 GHz) and Ka (18-36 GHz) band LNAs based on InP are currently in the fabrication process. Similarly, from the three presented mixers, the SiGe (35-50 GHz) and GaAs pHEMT mixer (33-55 GHz) have been successfully fabricated and measured, and the W-Band (70-120 GHz) I/Q mixer is in the design phase.

5.1 Future Measurements and Designs

The measurement process of the mm-wave low noise amplifiers is a challenging process for low noise high gain amplifiers. A noise measurement using the Y-factor method requires a Y-factor of at least 3-6 dB for a reliable measurement. However, due to an usually high internal noise figure of the receiver in noise analyzers at frequencies above 30 GHz, a preamplifier is used to overcome the noise of the internal receiver and achieve a high Y-factor. On the other hand, cascading a high gain DUT with a preamplifier can cause saturation of the internal receiver, limiting the total gain. As the frequency increases, the internal noise figure increases and the input compression point reduces, narrowing the "dynamic range" for a valid noise measurement. This problem becomes more challenging when the DUT has a wide bandwidth. The wider bandwidth corresponds to higher power levels saturating the analyzer. Different noise measurement methods are currently under investigation to address the limitations mentioned above to measure the InP LNAs that both are very wideband.

For the W-Band I/Q mixer the challenge is to develop an on-chip structure at very high frequencies. Accurate modeling of passive structures and EM simulation at such high frequency requires high computation power. Thus, a great effort is dedicated to design, model and integrate multiple passive structures such as Lange coupler, Wilkinson power divider, transformer baluns and grounded coplanar transmission lines.

Further efforts can focus of developing warm amplifiers and mm-wave down-converters as well as transimpedance amplifiers that are able to drive high sample-rates analog to digital converters to reduce the size and component count of the receivers. SiGe technology is a good solution to develop such application specific mm-wave integrated circuits.

Multi-chip modules that benefit from different semiconductors that are integrated on a single package are beneficial for front ends that are not cryogenically cooled, keeping downconverters and RF LNAs adjacent to each other, greatly reducing the size and complexity of the receiver.

References

[1] Very Large Array, July 2017 https://public.nrao.edu/telescopes/vla/ (last visit 11 Jul. 2021).

[2] K.G. Jansky, "Directional studies of atmospherics at high frequencies," *Proc. IRE,* 20.12 (1932): 1920-1932.

[3] J.C. Webber and M. W. Pospieszalski. "Microwave instrumentation for radio astronomy." *IEEE Trans. Microw. Theory Techn*., 50.3 (2002): 986-995.

[4] J.W.M. Baars, L.R. D'Addario, and A.R. Thompson, "Radio astronomy in the early twenty-first century,*" Proc. IEEE,* 97.8 (2009): 1377-1381.

[5] G. Reber, "Cosmic static," *Proc. IRE*, 28.2 (1940): 68-70.

[6] J.D. Kraus, Radio Astronomy. Powell, OH: Cygnus-Quasar Books, 1986, ch. 7, p. 12.

[7] M.A. Morgan, "Custom GaAs and InP components for radio astronomy," *IEEE Compound Semiconductor Integrated Circuit Symp. Dig.*, 2005, pp. 216-219.

[8] C. Chiong, H. Chen, J. Kao, H. Wang, and M. Chen, "180–220 GHz MMIC amplifier using 70-nm GaAs MHEMT technology," *Proc. IEEE Int. Symp.Radio-Frequency Integration Technology*, 2016, pp. 1-4.

[9] W. Ciccognani, F. Giannini, E. Limiti, and P. E. Longhi, "Full W-bBand high-gain LNA in mHEMT MMIC technology," *Proc. Eur. Microw. Integrated Circuit Conf.*, 2008, pp. 314-317.

[10] J. Moll *et al*., "Panel design of a MIMO imaging radar at W-band for space applications," *Proc. Eur. Radar Conf.*, 2017, pp. 126-129.

[11] M. Varonen *et al*., "Cryogenic W-band SiGe BiCMOS low-noise amplifier," *IEEE MTT-S Int. Microw. Symp. Dig.*, 2020, pp. 185-188.

[12] J. L. Jimenez-Martin, V. Gonzalez-Posadas, A. Parra-Cerrada, L. E. Garcia-Muñoz, and D. Segovia-Vargas, "Broadband (1-16 GHz) balanced MMIC GaAs pHEMT LNA for

radio astronomy applications," *Proc. Eur. Microwa. Conf. Central Europe*, 2019, pp. 91-94.

[13] M. Hosseini, W. Wong, and J. C. Bardin, "A 0.4–1.2 GHz SiGe cryogenic LNA for readout of MKID arrays," *IEEE MTT-S Int. Microw. Symp. Dig.*, 2019, pp. 164-167.

[14] N. Jiang, D. Garcia, P. Niranjanan, M. Halman, and I. Wevers, "Extremely low noise UHF-band amplifiers for square kilometer array", *Proc. Millimeter Submillimeter Far-Infrared Detectors Instrumentation for Astronomy VIII*, vol. 9914, pp. 991420, 2016.

[15] J. Schleeh, N. Wadefalk, P. Nilsson, J. P. Starski, and J. Grahn, "Cryogenic broadband ultra-low-noise MMIC LNAs for radio astronomy applications," *IEEE Trans. Microw. Theory Techn.*, 61.2 (2013): 871-877.

[16] https://www.analog.com/en/products/hmc-mdb169.html#product-overview (last visit 11 Jul. 2021).

[17] https://www.analog.com/en/products/hmc1093.html (last visit 11 Jul. 2021).

[18] W. Chakraborty *et al*., "Characterization and modeling of 22 nm FDSOI cryogenic RF CMOS," *IEEE J. Exploratory Solid-State Computational Devices and Circuits*, 7.2 (2021): 184-192.

[19] H. Y. Yang, J. H. Tsai, C. H. Wang, C. S. Lin, W. H. Lin, K. Y. Lin, T. W. Huang, and H. Wang, "Design and analysis of a 0.8–77.5-GHz ultra-broadband distributed drain mixer using 0.13-μm CMOS technology," *IEEE Trans. Microw. Theory Techn.*, 57.3 (2009): 562–572.

[20] J. Tsai, "Design of 40–108-GHz low-power and high-speed CMOS up-/down-conversion ring mixers for multistandard MMW radio applications," *IEEE Trans. Microw. Theory Techn*., 60.3 (2012): 670-678.

[21] P.-C. Huang et al., A compact 35-65 GHz up-conversion mixer with integrated broadband transformers in 0.18-μm SiGe BiCMOS technology," *Proc. IEEE Radio Frequency Integrated Circuits Symp.*, 2006, pp. 1-4.

[22] C. Chen, Y. Lin, Y. Chen, C. Chiong, and H. Wang, “A high LO-to-RF isolation 34–53 GHz cascode mixer for ALMA observatory applications,” in IEEE/MTT-S Int. Microw. Symp. Dig., Philadelphia, PA, June 2018, pp. 686-689.

[23] D. Henke et al., "Component development for ALMA band 1 (31–45 GHz)," *Proc. SPIE 7741, Millim., Submillim., Far-Infrared Detectors Instrum. Astron. V.*, Vol. 7741, 2010, pp. 1-13.

[24] D. Henke and S. Claude, "Minimizing RF performance spikes in a cryogenic orthomode transducer (OMT)." *IEEE Trans. Microw. Theory Techn.*, 62.4 (2014): 840-850.

[25] J. Tsai and T. Huang, “35–65-GHz CMOS broadband modulator and demodulator with sub-harmonic pumping for MMW wireless gigabit applications,” *IEEE Trans. Microw. Theory Techn.*, 55.10 (2007): 2075-2085.

[26] Y. Hwang, C. Han, and Y. Huang, “A photonic-tunable cryogenically cooled W-band subharmonically-pumped GaAs HEMT diode mixer module,” *Proc. Eur. Microw. Integrated Circuits Conf.*, 2009, pp. 208-211.

[27] S. Weng et al., “A 35–50 GHz triple cascode mixer module with intermediate frequency of 4–12 GHz based on low noise GaAs PHEMT process,” *Proc. IEEE Int. Symp. Radio-Frequency Integration Technol.*, 2016, pp. 1-3.

[28] Y.-C. Wu, C.-C. Chiong, J.-H. Tsai, and H. Wang, “A novel 30–90-GHz singly balanced mixer with broadband LO/IF,” *IEEE Trans. Microw. Theory Techn.*, 64.12 (2016): 4611-4623.

[29] Y.-C. Wu, Y.-J. Hwang, C.-C. Chiong, B.-Z. Lu, and H. Wang, “An innovative joint-injection mixer with broadband IF and RF for advanced heterodyne receivers of millimeter-wave astronomy,” *IEEE Trans. Microw. Theory Techn.*, 68.12 (2020): 5408-5422.

[30] S. Marsh, Practical MMIC Design. Artech House (2006).

[31] I.D. Robertson and S. Lucyszyn, eds., RFIC and MMIC Design and Technology. No. 13, IET, 2001.

[32] J.S. Kilby, "Semiconductor structure fabrication." U.S. Patent No. 3,435,516. 1 Apr. 1969.

[33] J. Arnold, “FET technology for low-noise front ends,” *IEEE Communication Mag.*, 1983, pp. 37–42.

[34] R.S. Pengelly and J. A. Turner, "Monolithic broadband GaAs FET amplifiers," *IET Electron. Lett*., 12.10 (1976): 251-252.

[35] H. Takahashi et al., "10-Gbit/s quadrature phase-shift-keying modulator and demodulator for 120-GHz-band wireless links," *IEEE Transactions on Microwave Theory and Techniques*, 58.12 (2010): 4072-4078.

[36] C. Wang et al., "A 10-Gbit/s wireless communication link using 16-QAM modulation in 140-GHz band," *IEEE Trans. Microw. Theory Techn*., 61.7 (2013): 2737-2746.

[37] E. Laskin et al., "165-GHz transceiver in SiGe technology," *IEEE J. Solid-State Circuits*, 43.5 (2008): 1087-1100.

[38] L. Nyssens et al., "28-nm FD-SOI CMOS RF figures of merit down to 4.2 K," *IEEE J. Electron Devices Soc*., 8 (2020): 646-654.

[39] M. J. Gong et al., "Design considerations for spin readout amplifiers in monolithically integrated semiconductor quantum processors," *Proc. IEEE Radio Frequency Integrated Circuits Symp.*, 2019, pp. 111-114.

[40] E. Cha et al., "Two-finger InP HEMT design for stable cryogenic operation of ultra-low-noise Ka- and Q-band LNAs," *IEEE Trans. Microw. Theory Techn*., 65.12 (2017): 5171-5180.

[41] J. Ajayan and D. Nirmal, "20-nm enhancement-mode metamorphic GaAs HEMT with highly doped InGaAs source/drain regions for high-frequency applications." *Int. J. Electronics* 104.3 (2017): 504-512.

[42] B. Heinemann et al., "SiGe HBT with fx/fmax of 505 GHz/720 GHz," *Proc. IEEE Int. Electron Devices Meet.*, 2016, pp. 3.1.1-3.1.4.

[43] N. Estella, L. Bui, E. Camargo, and J. Schellenberg, "35nm InP HEMT LNAs at E/W-band frequencies," *IEEE Compound Semiconductor Integrated Circuit Symp. Dig.*, 2016, pp. 1-3.

[44] J. V. Terán Collantes, L. de la Fuente, B. Aja, and E. Artal, "Cryogenic broadband Q-band MMIC low-noise amplifier," *Proc. Eur. Microw. Integrated Circuits Conf.*, 2016, pp. 77-80.

[45] R. Cleriti *et al*., "D-band LNA using a 40-nm GaAs mHEMT technology," *Proc. Eur. Microw. Integrated Circuits Conf.*, 2017, pp. 105-108.

[46] Y. Chen, Y. Wang, C. Chiong, and H. Wang, "An ultra-broadband low noise amplifier in GaAs 0.1-μm pHEMT process for radio astronomy application," *Proc. IEEE Int. Symp. Radio-Frequency Integration Technol*., 2017, pp. 80-82.

[47] A. H. Aljuhani, T. Kanar, and G. M. Rebeiz, "A packaged single-ended K-band SiGe LNA with 2.14 dB mean noise figure," *Proc. IEEE BiCMOS Compound Semiconductor Integrated Circuits and Technology Symp*., 2018, pp. 198-201.

[48] E. Turkmen, A. Burak, A. Guner, I. Kalyoncu, M. Kaynak, and Y. Gurbuz, "A SiGe HBT D-band LNA with Butterworth response and noise reduction technique," *IEEE Microw. Wireless Compon. Lett.*, 29.6 (2018): 524-526.

[49] A. Nainani, "Hole mobility and its enhancement with strain for technologically relevant III-V semiconductors." *Proc. International Conference on Simulation of Semiconductor Processes and Devices*, 2009, pp. 1-4.

[50] P.P. Ruden, "Quantum-well p-channel AlGaAs/InGaAs/GaAs heterostructure insulated-gate field-effect transistors." *IEEE Trans Electron Devices* 36.11 (1989): 2371-2379.

[51] A. Nainani et al., "Engineering of strained III–V heterostructures for high hole mobility." *Proc. Int. Electron Devices Meet.*, 2009, pp. 1-4.

[52] S. Oktyabrsky and D. Ye Peide, eds., Fundamentals of III-V semiconductor MOSFETs. New York: Springer, 2010.

[53] H.J. Sell, “Growth of GaInAs bulk mixed crystals as a substrate with a tailored lattice parameter”. Journal of crystal growth, 107(1-4), 1991, pp. 396-402.

[54] M.I. Ziane, "First-principles prediction of the structural and electronic properties of zinc blende GaN x As 1− x alloys." *Materials Science in Semiconductor Processing* 16.4 (2013): 1138-1147.

[55] S. Kayali, "GaAs Material Properties." JPL Publication 96 25 (2006).

[56] T. Mimura et al., "A new field-effect transistor with selectively doped GaAs/n-AlxGa1-xAs heterojunctions." *Japan. J. Applied Physics* 19.5,1980, L252

[57] C.G. Yuan et al., "0.15 micron gate 6-inch pHEMT technology by using I-line stepper." *Proc. CS MANTECH Conf.,* 2009.

[58] M. Chertouk et al., "Manufacturable 0.15 um PHEMT process for high volume and low cost on 6” GaAs Substrates: The First 0.15 μm PHEMT 6” GaAs Foundry Fab," *Proc. GaAs MANTECH Conf.,* 2002.

[59] R. Ma , J. Lapointe, C. Storey, P. Poole, F. Jiang, A. Seyfollahi, A. W. Walker, J. Noël, A. Kam, and A. Densmore. "Impacts on access resistance of InP high electron mobility transistors from wafer processing." *J. Vacuum Science & Technology B, Nanotechnology and Microelectronics: Materials, Processing, Measurement, and Phenomena* 38. 2, 2020, 022212.

[60] J. Schleeh *et al*., "Ultralow-power cryogenic InP HEMT with minimum noise temperature of 1 K at 6 GHz," *IEEE Electron Device Lett.* 33. 5 (2012), 664-666.

[61] J. Ajayan, D. Nirmal, P. Mohankumar, D. Kuriyan, A. S. Augustine Fletcher, L. Arivazhagan, and B. Santhosh Kumar, "GaAs metamorphic high electron mobility transistors for future deep space-biomedical-military and communication system applications: A review," *Microelectron. J.*, 92 (2019):104604.

[62] J. Ajayan, D. Nirmal, P. Prajoon, and J.C. Pravin, “Analysis of nanometer-scaleInGaAs/InAs/InGaAs composite channel MOSFETs using high-K dielectrics for high speed applications,” *Int. J. Electron. Commun.* 79 (2017): 151–157.

[63] J. Ajayan, D. Nirmal, T. Ravichandran, P. Mohankumar, P. Prajoon, L. Arivazhagan, and C. Kumar Sarkar, “InP high electron mobility transistors for submillimetre wave and terahertz frequency applications: a review”, *Int. J. Electron. Commun.* 94 (2018): 199–214.

[64] R. Cleriti, W. Ciccognani, S. Colangeli, A. Serino, E. Limiti, P. Frijlink, M. Renvoise, R. Doerner, and M. Hossain, “D-band LNA using a 40-nm GaAs mHEMT technology,” *Proc. Eur. Microw. Integrated Circuits Conf.*, 2017, pp. 105–108.

[65] R. Weber, H. Massler, and A. Leuther, “D-band low-noise amplifier MMIC with 50% bandwidth and 3.0 dB noise figure in 100 nm and 50 nm mHEMT technology,” *IEEE MTT-S Int. Microw. Symp. Dig.*, 2017, pp. 756–759.

[66] L. John, T. Merkle, C. Friesicke, A. Tessmann, A. Leuther, R. Lozar, M. Schlechtweg, and T. Zwick, “Investigation of direct-coupled amplifier topologies for wireless communication systems using normally-on mHEMT technology,” *IEEE MTT-S Int. Microw. Symp. Dig.*, 2017, pp. 1129–1132.

[67] B. Amado-Rey, Y. Campos-Roca, C. Friesicke, A. Tessmann, H. Massler, S. Wagner, A. Leuther, M. Schlechtweg, and O. Ambacher, “A broadband 175–245 GHz balanced medium power amplifier using 50-nm mHEMT technology,” *Proc. Asia-Pacific Microw. Conf.*, 2016, pp. 1-4;

[68] X. Cheng, L. Zhang, and X. Deng, “Ka-band low noise amplifier using 70nm MHEMT process for wideband communication,” *Proc. Int. Conf. Semiconductor Technol.*, 2017, pp. 1-2.

[69] R. Cleriti, W. Ciccognani, S. Colangeli, E. Limiti, P. Frijlink, and M. Renvoise, “Characterization and modelling of 40 nm mHEMT process up to 110 GHz,” *Proc. Eur. Microw. Integrated Circuits Conf.*, 2016, pp. 353–356.

[70] W.-L. Chang, C. Meng, K.-C. Tsung, and G.-W. Huang, “30-GHz mHEMT divide-by-three injection-locked frequency divider with Marchand balun,” *Proc. Radio Wirel. Symp.*, 2015, pp. 68–70.

[71] M.L. Bhavsar, R. Sharma, and A. Bhattacharya, “Monolithic Ka- to Ku-band all balanced sub-harmonic resistive MHEMT mixer for satellite transponder,” *IEEE Microw. Wirel. Compon. Lett.* 25 (2015): 316–318;

[72] M.L. Bhavsar, A. Bhattacharya, and R.K. Arora, “Design and comparison of MHEMT and diode based K-band sub-harmonically pumped mixer MMICs,” *Proc. Int. Microw. RF Conf.*, 2014, pp. 26-269.

[73] K. Yaohui, W. Weibo, G. Jianfeng, and C. Chen, “100 MHEMT transistor technology for W-band amplifier,” *Proc. 3rd Asia-Pacific Antennas Propagat. Conf.*, 2014, pp. 1339-1341.

[74] S. Voinigescu, “High-frequency integrated circuits”, Cambridge University Press, 2013.

[75] D. B. Estreich, “Basics of compound semiconductor ICs”, IEEE CSICS, Primer Course, October 2010.

[76] G. W. Wang et al., "A 0.1 μm gate AlInAs/GaInAs MODFET fabricated on GaAs substrates." *IEEE Trans. Electron Devices* 35.7 (1988): 818-823.

[77] T. H. Tsai et al., "On a Pd/InAlAs metamorphic high electron mobility transistor (MHEMT)-based hydrogen sensor," *Sens. Actuators B Chem.*, 139.2 (2009): 310-316.

[78] D. Smith, G. Dambrine, and J. Orlhac, "Industrial MHEMT technologies for 80 - 220 GHz applications," *Proc. Eur. Microw. Integrated Circuits Conf.*, 2008, pp. 214-217.

[79] I. D. Robertson, and S. Lucyszyn, eds., RFIC and MMIC Design and Technology. No. 13, IET, 2001.

[80] W.R. Curtice, "A MESFET model for use in the design of GaAs integrated circuits," *IEEE Trans. Microw. Theory Techn.* 28.5 (1980): 448-456.

[81] W.R. Curtice and M. Ettenberg, "A nonlinear GaAs FET model for use in the design of output circuits for power amplifiers," *IEEE Trans. Microw. Theory Techn.* 33.12 (1985): 1383-1394.

[82] I. Angelov, H. Zirath, and N. Rosman, "A new empirical nonlinear model for HEMT and MESFET devices," *IEEE Trans. Microw. Theory Techn.* 40.12 (1992): 2258-2266.

[83] I. Angelov, L. Bengtsson, and M. Garcia, "Extensions of the Chalmers nonlinear HEMT and MESFET model," *IEEE Trans. Microw. Theory Techn.* 44.10 (1996): 1664-1674.

[84] I. Angelov, H. Zirath, and N. Rorsman, "Validation of a nonlinear HEMT model by power spectrum characteristics," *IEEE MTT-S Int. Microw. Symp. Dig.*, 1994, pp. 1571-1574.

[85] I. Angelov, Transistor Level Modeling for Analog/RF IC Design, The Netherlands, Dordrecht: Springer-Verlag, 2006.

[86] I. Angelov, M. Ferndahl, F. Ingvarson, H. Zirath and H. O. Vickes, "CMOS Large Signal and RF Noise Model for CAD," *Proc. Eur. Microw. Integr. Circuits Conf.*, 2006, pp. 217-220.

[87] I. Angelov et al., "Large-signal modelling and comparison of AlGaN/GaN HEMTs and SiC MESFETs," *Proc. Asia-Pacific Microw. Conf.*, 2006, pp. 279-282.

[88] I. Angelov, V. Desmaris, K. Dynefors, P. A. Nilsson, N. Rorsman and H. Zirath, "On the large-signal modelling of AlGaN/GaN HEMTs and SiC MESFETs," *Proc. Eur. Gallium Arsenide and Other Semiconductor Application Symposium*, 2005, pp. 309-312.

[89] L. Liu, J. Ma, and G. Ng, "Electrothermal large-signal model of III–V FETs accounting for frequency dispersion and charge conservation," *IEEE MTT-S Int. Microw. Symp. Dig.*, 2009, pp. 749-752.

[90] J. Böck et al., "SiGe HBT and BiCMOS process integration optimization within the DOTSEVEN project," *Proc. IEEE Bipolar/BiCMOS Circuits and Technology Meet.*, 2015, pp. 121-124.

[91] B. Heinemann et al., "SiGe HBT with fx/fmax of 505 GHz/720 GHz," *Proc. IEEE Int. Electron Devices Meet.*, 2016, pp. 3.1.1-3.1.4

[92] A. Fox et al., "Advanced Heterojunction Bipolar Transistor for Half-THz SiGe BiCMOS Technology," *IEEE Electron Device Lett.*, 36.7 (2015): 642-644.

[93] Y. Taur and T.H. Ning, “Fundamentals of modern VLSI devices”, Cambridge University Press, 2nd Ed., 2009.

[94] D. Henke et al., “Octave Band Receiver for ngVLA”, HAA-RIT-NGVLA-002-REP-A, 2021.

[95] A. Seyfollahi et al. “MM-Wave Mixer Develoment for ngVLA Band 5 and 6 Receivers”, HAA-RIT-NGVLA-004-REP-A, 2021.

[96] T. Kojima, H. Kiuchi, K. Uemizu, Y. Uzawa, M. Kroug, A. Gonzalez, T. Dippon, and T. Kageura. "Demonstration of a wideband submillimeter-wave low-noise receiver with 4–21 GHz IF output digitized by a high-speed 32 GSps ADC," Astronomy & Astrophysics 640, p L9, 2020.

[97] D. Cuadrado-Calle, D. George, G.A. Fuller, K. Cleary, L. Samoska, P. Kangaslahti, J.W. Kooi, M. Soria, M. Varonen, R. Lai, and X. Mei. "Broadband MMIC LNAs for ALMA Band 2+3 with noise temperature below 28 K," *IEEE Trans. Microw. Theory Techn.*, 65.5 (2017): 1589-1597.

[98] M. W. Pospieszalski, "On the limits of noise performance of field effect transistors," *IEEE MTT-S Int. Microw. Symp. Dig*., 2017, pp. 1953-1956.

[99] M. W. Pospieszalski, “Interpreting transistor noise,” *IEEE Microw. Mag.* 11.6 (2010): 61–69.

[100] G. Gonzalez, Microwave Transistor Amplifiers Analysis and Design. Prentice-Hall, Inc., 1996.

[101] A. Seyfollahi, Monolithic microwave integrated circuit (MMIC) low noise amplifier (LNA) design for radio astronomy applications. MASc Thesis, University of Victoria, 2018.

[102] K. Vanderlinde, A. Liu, B. Gaensler, D. Bond, G. Hinshaw, C. Ng., C. Chiang, I. Stairs, J.A. Brown, J. Sievers, and J. Mena, “The Canadian Hydrogen Observatory and

Radio-transient Detector (CHORD),” Canadian Long Range Plan for Astronomy and Astrophysics White Papers, 2020, p.28.

[103] E. Cha, N. Wadefalk, P. Nilsson, J. Schleeh, G. Moschetti, A. Pourkabirian, S. Tuzi, and J. Grahn, "0.3–14 and 16–28 GHz wide-bandwidth cryogenic MMIC low-noise amplifiers," *IEEE Trans. Microw. Theory Techn*. 66.11 (2018): 4860-4869.

[104] T. Kulatunga, L. Belostotski, and J. W. Haslett, "400-to-800-MHz GaAs pHEMT-based wideband LNA for radio-astronomy antenna-array feed," *IEEE Microw. Wireless Compon. Lett*. 28.10 (2018): 909-911.

[105] J. Xu, W. A. Serdijn, B. Woestenburg, and J. G. bij de Vaate, "GaAs 0.5 dB NF dual-loop negative-feedback broadband low-noise amplifier IC," *IEE Electron. Lett*. 41.14 (2005): 780-782.

[106] L. Belostotski and J. W. Haslett, "Wide band room temperature 0.35-dB noise figure LNA in 90-nm bulk CMOS," *Proc. IEEE Radio Wireless Symp*., 2007, pp. 221-224.

[107] J. V. Terán Collantes, L. de la Fuente, B. Aja, and E. Artal, "Cryogenic broadband Q-band MMIC low-noise amplifier," *Proc. Eur. Microw. Integr. Circuits Conf*., 2016, pp. 77-80.

[108] S. H. Weng, W. C. Wang, H. Y. Chang, C. C. Chiong, and M.-T. Chen “An ultra low-power Q-band LNA with 50% bandwitdth in WIN GaAs 0.1-μm pHEMT process,” *Proc. Asia-Pacific Microw. Conf*., 2013, pp. 713-715.

[109] S.H. Weng, C.H. Lin, H.Y. Chang, and C.C. Chiong, “Q-band low noise amplifiers using a 0.15-μm MHEMT process for broadband communication and radio astronomy applications,” *IEEE MTT-S Int. Microw. Symp. Dig*., June 2006, pp. 89-92.

[110] E. Cha et al., "Two-finger InP HEMT design for stable cryogenic operation of ultra-low-noise Ka- and Q-band LNAs," *IEEE Trans. Microw. Theory Techn*. 65.12 (2017): 5171-5180.

[111] D.M. Pozar, Microwave and RF Wireless Systems, John Wiley & Sons, 2001, Chapter 7.

[112] H. Y. Yang, J. H. Tsai, C. H. Wang, C. S. Lin, W. H. Lin, K. Y. Lin, T. W. Huang, and H. Wang, "Design and analysis of a 0.8–77.5-GHz ultra-broadband distributed drain mixer using 0.13-μm CMOS technology," *IEEE Trans. Microw. Theory Techn.* 57.3 (2009): 562–572.

[113] J. Tsai, "Design of 40–108-GHz low-power and high-speed CMOS up-/down-conversion ring mixers for multistandard MMW radio applications," *IEEE Trans. Microw. Theory Techn.* 60.3 (2012): 670-678.

[114] Ping-Chen Huang et al., "A compact 35-65 GHz up-conversion mixer with integrated broadband transformers in 0.18-μm SiGe BiCMOS technology," *Proc. IEEE Radio Frequency Integrated Circuits Symp.*, 2006, pp. 1-4.

[115] C. Chen, Y. Lin, Y. Chen, C. Chiong, and H. Wang, "A high LO-to-RF isolation 34–53 GHz cascode mixer for ALMA observatory applications," *IEEE/MTT-S Int. Microw. Symp. Dig.*, 2018, pp. 686-689.

[116] J. Tsai and T. Huang, "35–65-GHz CMOS broadband modulator and demodulator with sub-harmonic pumping for MMW wireless gigabit applications," *IEEE Trans. Microw. Theory Techn*. 55.10 (2007): 2075-2085.

[117] Y. Hwang, C. Han, and Y. Huang, "A photonic-tunable cryogenically cooled W-band subharmonically-pumped GaAs HEMT diode mixer module," *Proc. Eur. Microw. Integrated Circuits Conf*., 2009, pp. 208-211.

[118] S. Weng et al., "A 35–50 GHz triple cascode mixer module with intermediate frequency of 4–12 GHz based on low noise GaAs PHEMT process," *Proc. IEEE Int. Symp. Radio-Frequency Integration Technol.*, 2016, pp. 1-3.

[119] Y.-C. Wu, C.-C. Chiong, J.-H. Tsai, and H. Wang, "A novel 30–90-GHz singly balanced mixer with broadband LO/IF," *IEEE Trans. Microw. Theory Techn*. 64.12 (2016): 4611-4623.

[120] Y.-C. Wu, Y.-J. Hwang, C.-C. Chiong, B.-Z. Lu, and H. Wang, "An innovative joint-injection mixer with broadband IF and RF for advanced heterodyne receivers of millimeter-wave astronomy," *IEEE Trans. Microw. Theory Techn*. 68.12 (2020): 5408-5422.

[121] J. Kao, C. Chou, C. Chiong, C. Chuang, and H. Wang, “A high LO-to-RF isolation 32–52 GHz triple cascode down-conversion mixer with 2–12 GHz IF bandwidth for ALMA band-1,” *Proc. Asia-Pacific Microw. Conf.*, 2014, pp. 1190-1192.

[122] J. A. Qayyum, J. D. Albrecht, and A. C. Ulusoy, “A compact V-band upconversion mixer with −1.4-dBm OP1dB in SiGe HBT technology,” *IEEE Microw. Wireless Compon. Lett*. 29. 4 (2019): 276-278.

[123] Y. Wu, C. Chiong, J. Tsai, and H. Wang, “A novel 30–90-GHz singly balanced mixer with broadband LO/IF,” *IEEE Trans. Microw. Theory Techn*. 64.12 (2016): 4611-4623.

[124] Z.-M. Tsai, J.-C. Kao, K.-Y. Lin, and H. Wang, "A 24–48 GHz cascode HEMT mixer with DC to 15 GHz IF bandwidth for astronomy radio telescope", *Proc. IEEE Eur. Microw. Integr. Circuits Conf.*, 2009, pp. 5-8.

[125] J.-C. Kao, C.-F. Chou, C.-C. Chiong, C.-C. Chuang, and H. Wang, “A high LO-to-RF isolation 32–52 GHz triple cascode down-conversion mixer with 2–12 GHz IF bandwidth for ALMA band-1,” *Proc. IEEE Asia–Pacific Microw. Conf.*, 2014, pp. 1190–1192.